NSK Technical Journal

Motion & Control

No. 26 April 2016

NSK's Latest Technologies and Products for Industrial Machinery

ISSN1342-3630

NSK

MOTION & CONTROL No. 26
NSK Technical Journal
Printed and Published: April 2016
ISSN1342-3630
Publisher: NSK Ltd., Ohsaki, Shinagawa, Tokyo, JAPAN
Public Relations Department
TEL +81-3-3779-7050
FAX +81-3-3779-7431
Editor: Hirotoshi ARAMAKI
Managing Editor: Hitoshi EBISAWA
Design, Typesetting & Printing: Kuge Printing Co., Ltd.

NSK Technical Journal
Motion & Control
No. 26
April 2016

Contents

NSK's Latest Technologies and Products for Industrial Machinery

Preface

Technical Articles

New Products

Technical Articles

New Products

Preface

NSK's Latest Technologies and Products for Industrial Machinery

Seiji Ijuin
Vice President

Bearings support industries from the bottom, which lends them the nickname "the rice of industry."

Industries are rapidly expanding in newly developing areas such as China and other Asian countries. Just as Japan experienced in the past, this high growth means energy conservation, harmony with the environment, and assurance of human safety are demands that must be met for a modern society. As "the rice of industry," new technologies have been incorporated into bearings to meet these demands. We will introduce these in the following "NSK's Latest Technologies and Products for Industrial Machinery."

Bearings not only contribute to the reduction of consumption by reducing rotational torque but also support changing industrial machinery by saving energy with new technologies. In this special issue, we will introduce energy-saving compressors and bearings for refrigerating machines, bearings that support the increased production of LEDs and solar batteries, and bearings used in wind-power generators for renewable energy, as well as low-torque technologies and related bearing products. In addition, concern for human safety is larger than ever. A new grease made of food oil and food additives only, microelectromechanical systems (MEMS), and nanotechnology connecting ultra-miniature sensors will be introduced to show NSK's commitment to addressing this concern.

NSK supports industrial development and the global environment based on the four core tenets of material technology, tribology, analysis, and mechatronics, now and in the future.

Seiji Ijuin

Prismless Surface Plasmon Resonance (P-SPR) Sensor Using Periodic Nanostructures

Keisuke Yokoyama
NSK Ltd.
Marie Oshima
Institute of Industrial Science, The University of Tokyo

ABSTRACT

A Prismless surface plasmon resonance (P-SPR) sensor using periodic nanostructure of an equilateral triangle has been developed. Each nanostructure has a hole of 129 nm diameter and 243 nm depth aligned on each corner. The P-SPR sensor consists of a fixed optical fiber above the sensor substrate, unlike a conventional SPR sensor. In order to provide further portability, a collimator is mounted on the optical fiber so that the collimated light illuminates the sensor substrate. With a collimator-mounted optical fiber, the P-SPR sensor exhibits a stable real-time measurement signal, even with the optical fiber 30 mm away from the sensor substrate. Thus, it can be possible to hand-carry each component of equipment separately and assemble on-site for measurement. The present sensor substrate gives a spectrum with a sharp single resonance peak wavelength (λ_{peak}) which linearly shifts along with the surrounding refractive index. The P-SPR sensor also demonstrates avidin-biotin interaction on the sensor substrate, and shows good correlation in linearity in both logarithmic scales between avidin concentrations (1, 3.3, 10, 33, 100 nM) and reaction velocities.

Reprinted from FLUCOME2013: The 12th International Symposium on Fluid Control, Measurement and Visualization
November 18–23, 2013, Nara, Japan.

1. Introduction

Since Kretschmann and Otto developed surface plasmon resonance (SPR) sensor[1), 2)] in 1968, many studies of molecular interaction using SPR sensor have been reported[3), 4)]. Those types of SPR sensor require an incident light which travels through a prism located on the sensor substrate with a certain angle to produce an evanescent wave on the sensor substrate. A movable detector is mounted on the other side of the incident light source to collect the reflected light with another certain angle which depends on the surrounding refractive index of the sensor substrate. However, a conventional SPR sensor is bulky and expensive due to those complex structures, and it appears difficult to hand-carry and to measure a biomolecule or chemical on-site.

In order to miniaturize an SPR sensor for the portability, a variety of nanostructures from nanoparticles to nano-order patterned substrates are utilized. Nath et al[5)]. applied nanoparticles for the sensor to measure a change in refractive index using localized surface plasmon resonance (LSPR). A sensor substrate with the ordered nanoparticles shows the higher sensitivity than that of disordered nanoparticles in a solution[6)], whereas it is difficult to give a reproducibility of the sensor substrate fabrication with the ordered nanoparticles.

Since Ebbesen et al[7)]. discovered the extraordinary optical transmission through sub-wavelength hole arrays, a sensor substrate with periodic nanostructure has emerged. Nanostructures on the sensor substrate are fabricated by nano technology, such as a focused ion beam technique and an electron beam lithography technique. When an incident light illuminates the sensor substrate with periodic nanostructures in a triangular lattice, the transmitted or reflected light spectrum shows a resonance peak wavelength which is determined by:

$$\lambda_{\text{peak}} = \frac{\sqrt{3}\,d}{2\left(i^2 + j^2 - ij\right)^{1/2}} \left[\frac{\varepsilon_{\text{m}}\, n^2}{\varepsilon_{\text{m}} + n^2}\right]^{1/2} \qquad (1)$$

where λ_{peak} is the peak wavelength, d is the periodicity of a unit structure, i and j are the diffracted order, ε_m is the dielectric constant of the surface metal, and n is the surrounding refractive index.

Yeom et al[8)]. and Nakamoto et al[9)]. reported that the P-SPR sensor measured the relationship between the concentration of the biomolecules and the peak wavelength. The former uses the sensor substrate with random nanostructures, and the latter uses the conventional sensor substrate which aligns a hole in the triangular lattice. Both groups measure with the normal optical fiber, and the light beam diffuses at the edge of the optical fiber. Thus, there is a possibility that the signal is unstable during the measurement.

In this paper, we developed the high-sensitive compact prismless SPR sensor by designing the unique periodic nanostructures on the sensor substrate with a collimator-embedded optical fiber. The sensor substrate is fabricated through the thermal nanoimprinting and sputtering techniques to align nanostructures uniformly. We enhanced the measurement by using the zero-ordered reflected light with a collimator-embedded optical fiber. We observed the peak wavelength shift ($\Delta\lambda_{peak}$) with different refractive index liquids. We also monitored the behavior of the peak wavelength for the avidin-biotin reaction. As a result, it is concluded that our sensor system is a high-sensitive compact prismless SPR sensor.

2. Materials

Cyclo Olefin Polymer (COP) film was obtained from ZEON Corporation (Tokyo, Japan). A release agent was purchased from HARVES Co. Ltd. (Saitama, Japan). 11-Amino-1-undecanethiol hydrochloride (AUT), (+)-biotin N-hydroxysuccinimide ester (Biotin-NHS), avidin, ethanol, isopropyl alcohol, dimethyl sulforxide (DMSO), water and phosphate-buffered saline (PBS) were purchased from Sigma-Aldrich (St. Louis, MO, USA). All chemicals were of analytical grade and were used without further purification.

3. Fabrication Method

A sensor substrate with periodic nanostructures was prepared with thermal nanoimprinting technique. Thermal nanoimprinting technique provides a method of transferring uniformly nanostructure pattern of the mold to a thermoplastic film[10)]. The molds made of silicon and of silicon with silicon oxides were fabricated at SCIVAX Corporation (Tokyo, Japan) and at NTT Advanced Technology Corporation (Tokyo, Japan), respectively. In order to coat a release layer on molds, the molds were first immersed in the release agent for 1 minute and dried for 24 hours at room temperature, then immersed in the rinse agent to remove excess release agent.

A sensor substrate was fabricated as shown in Fig. 1. The mold was placed onto the silicon substrate. A piece of COP film followed by the silicon substrate were placed onto the mold. They were sandwiched with silicon wafers and cautiously loaded onto the thermal nanoimprinting machine. Then the sensor substrate with periodic nanostructure was loaded into the sputtering machine. The gold was deposited onto the sensor substrate under pure argon atmosphere.

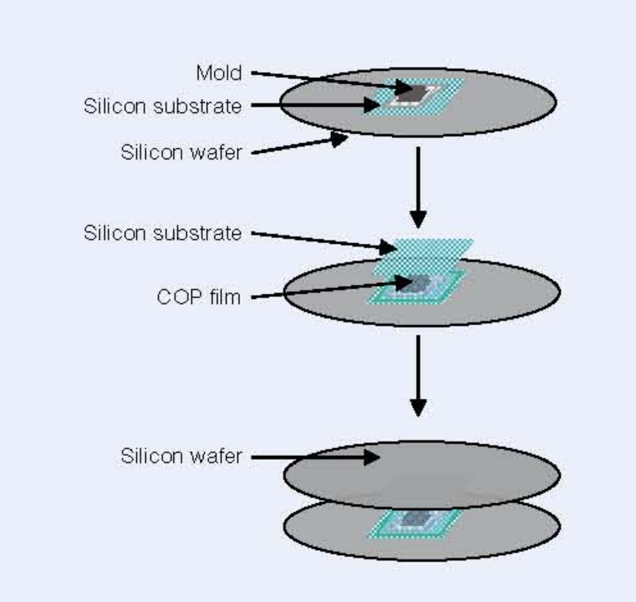

Fig. 1 Fabrication method of the sensor substrate.

4. Measurement System

The schematic illustration of our measurement system is shown in Fig. 2. Tungsten halogen lamp is used as an incident light source and the spectrometer is used as a detector capable of measuring wavelength within a range of 400 nm to 900 nm. A collimator is mounted on the optical fiber which consists of two optical fibers bundled to produce the collimated light beam.

As shown in Fig. 3, the sensor substrate is placed onto a polytetrafluoroethylene platform with two ports for an inlet and an outlet tubes. A polydimethylsiloxane (PDMS) channel followed by a slide glass are placed to provide the flow channel that is 4 mm wide, 40 mm long and 500 µm thick. The sensor substrate, the PDMS channel and the slide glass are tightly fixed with the jigs. The flow cell is loaded onto the measuring equipment. The optical fiber is mounted vertically to the sensor substrate so as to illuminate the collimated incident light and receive the maximum zero-order reflected light from the sensor substrate. A sample solution is transported from the sample tube to the flow cell by the pump. Reflectivity of the sensor substrate, R_S , is calculated by

$$R_{\text{S}} = \frac{I_{\text{S}} - I_{\text{B}}}{I_{\text{Al}} - I_{\text{B}}} \times R_{\text{Al}} \qquad (2)$$

where I_S, I_B and I_{Al} are reflected light intensities of the sensor substrate, background and an aluminium reference mirror, respectively. R_{Al} is the reflectivity of the aluminium reference mirror.

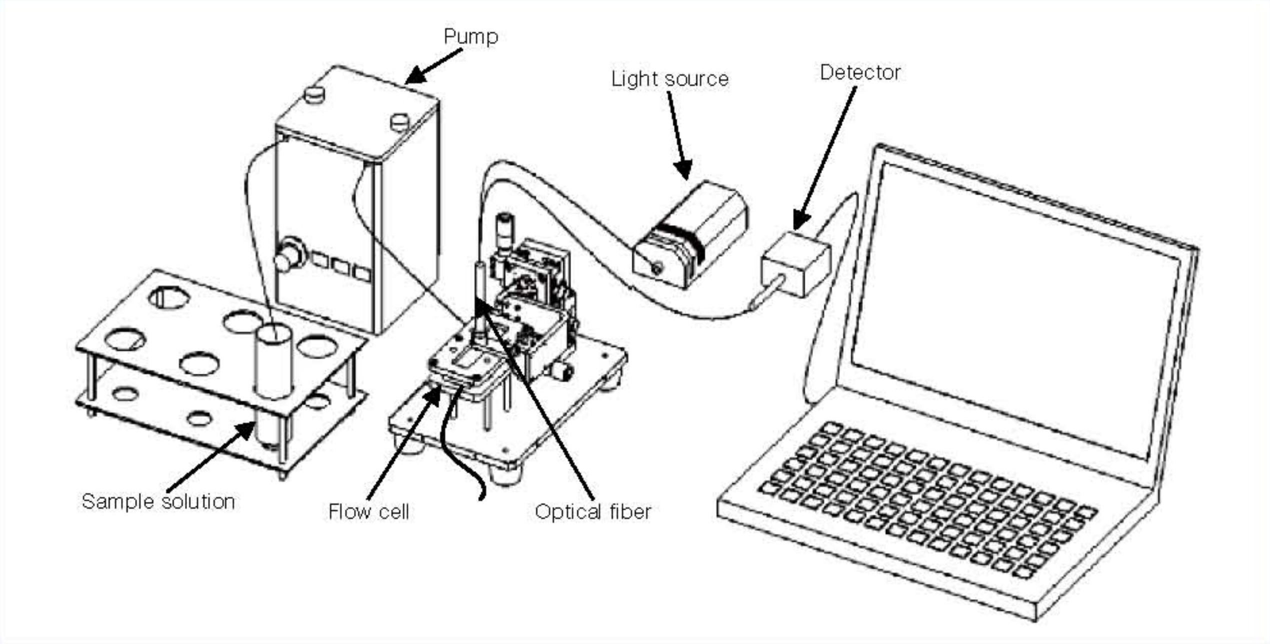

Fig. 2 Measurement system.

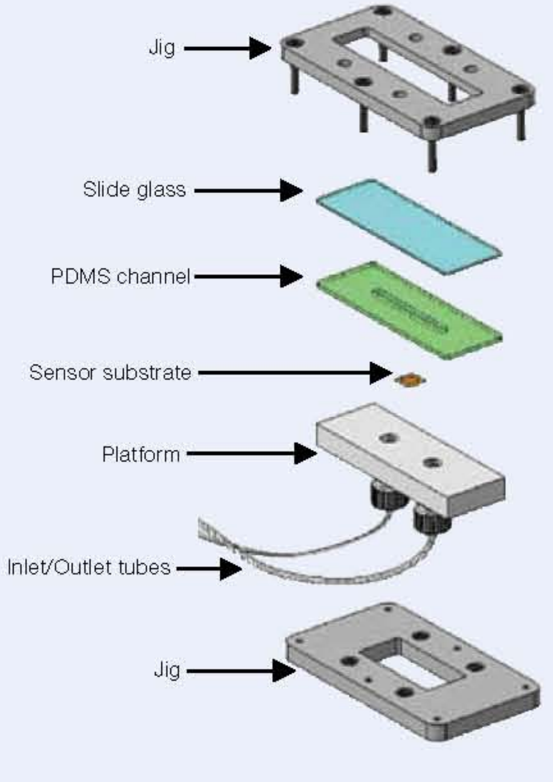

Fig. 3 Flow cell.

5. Results and Discussion

5.1 AFM characterization

The conventional and the developed sensor substrates were fabricated through the thermal nanoimprinting and sputtering techniques. Each sensor substrate was evaluated with an atomic force microscopy (AFM, Agilent 5500, Agilent Technologies Inc., CA, USA). Figure 4 shows the images of the sensor substrates. The dimensions of the sensor substrates are summarized in Table 1. Table 2 shows the results of the AFM measurements for 3 different sites of the conventional sensor substrate. It is indicated that the periodic nanostructures on the sensor substrates are successfully and uniformly fabricated.

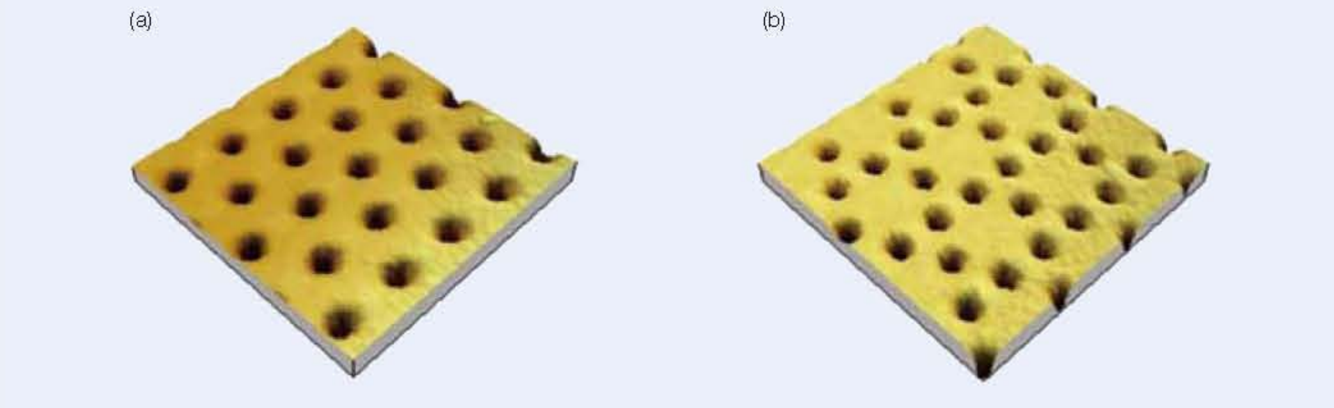

Fig. 4 AFM images of the sensor substrates.
(a) Conventional sensor substrate. (b) Developed sensor substrate.

Table 1 Periodicity, hole diameter and hole depth of the sensor substrates.

	Conventional	Developed
Periodicity (nm)	456	613
Diameter (nm)	207	129
Depth (nm)	200	243

Table 2 Dimensions at different sites in the same sensor substrate.

	1	2	3
Periodicity (nm)	458	460	459
Diameter (nm)	135	137	132
Depth (nm)	199	198	196

5.2 Effects of gold thickness

In order to determine the gold layer thickness of the sensor substrate, the gold bulk substrate and the conventional sensor substrates with different thickness layers of gold, 100, 200, 300 and 400 nm, were prepared. The sensor substrates were placed onto the platform with a single through-hole in the center through which a transmitted component of incident light passes and no longer return back to the optical fiber.

Figure 5 shows the spectra of each sensor substrate and the gold bulk substrate. The spectra from the sensor substrates exhibited the distinct dip around 525 nm, whereas no dip was observed for the spectrum of the gold bulk substrate. Those dips of spectra are attributed to the surface plasmon resonance deriving from the excitation of surface plasmon polaritons.

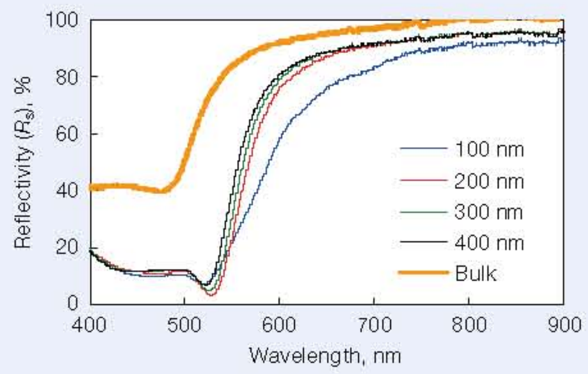

Fig. 5 Spectra of the gold bulk substrate and the sensor substrates with different gold thickness layer.

Although the spectra of 200, 300 and 400 nm gold thickness sensor substrates behave in the similar way, the spectrum of 100 nm gold thickness sensor substrate shows lower reflectivity especially in the range from 520 to 800 nm. This phenomenon indicates that some amount of incident light penetrate through the 100 nm-thick gold layer and underneath COP film substrate. Thus, 200 nm has been chosen for the gold thickness of the sensor substrate for all the experiments below.

5.3 Real-time signal monitoring with collimator-mounted optical fiber

In our measuring system, a collimator is mounted on an optical fiber to illuminate incident light vertically to the sensor substrate and to receive the maximum zero-order reflected light as much as possible. Also such a structure gives assembly robustness so as to carry each part of equipment separately and to easily assemble them on-site for measurement. Without a collimator, the light coming out of the optical fiber diffuses at the end of the optical fiber with the half-angle θ of the maximum cone of light. Thus, the diameter of the sensing spot on the sensor substrate strongly depends on the distance between the optical fiber and the sensor substrate, and is given by:

$$D = 2l \tan\theta \tag{3}$$

where D is the diameter of the sensing spot, and l represents the distance between the optical fiber and the sensor substrate. According to Eq. (3), the diameter of the sensing spot increases with an increase in the distance. This indicates that the intensity of the zero-order reflected light decreases with an increase in the distance.

Figure 6 shows the effects of different distances on the zero-order reflected light intensity using the optical fiber with and without the collimator. The zero-order reflected light intensity through the collimator-mounted optical fiber located 30 mm away from the sensor substrate is much stronger than that from the normal optical fiber even 15 mm away from the sensor substrate. Figure 7 shows the real-time peak wavelength behavior of each experimental condition for 350 sec. The peak wavelength from the optical fiber with collimator is stable, whereas the other two peak wavelengths moved up and down while data were collected. This could be mainly because the collimator-mounted optical fiber vertically illuminates incident light in parallel so that the most of the zero-order reflected light returns back to the optical fiber resulting in producing a stable real-time signal.

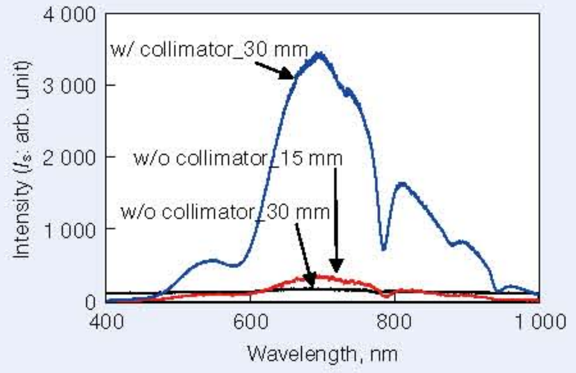

Fig. 6 Intensity of the zero-order reflected light.

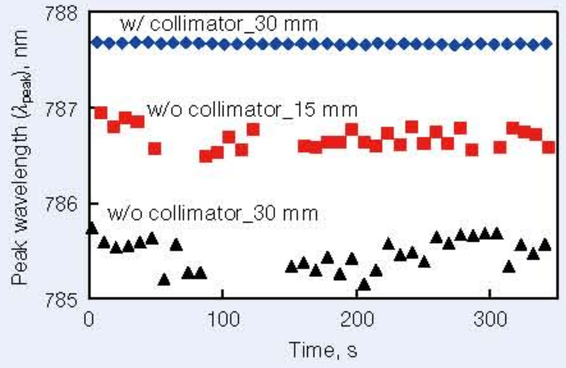

Fig. 7 Effects of the collimator on measurement behavior.

5.4 Sensitivity for refractive index of bulk liquids

Equation (1) describes how the peak wavelength is determined by the surrounding different refractive index. We used 6 liquids with different refractive indexes to see whether the sensor substrate functions as a sensor for different surrounding refractive indexes. Table 3 shows the liquids and their refractive indexes.

First, water was transported to the flow cell and the spectrum shown in Fig. 8 was obtained. Six liquids were continuously transported to the flow cell in descending order of the refractive index from water to isopropyl alcohol. The peak wavelength shift against different refractive indexes is shown in Fig. 9. The increase in refractive index leads to the red shift of the peak wavelength. The relationship between the peak wavelength and the refractive index are plotted in Fig. 10, which gives a linear correlation between the peak wavelength and the refractive index. It has proved that the sensor substrate with periodic nanostructures functions as a sensor measuring a change in refractive index.

Table 3 Refractive indexes of bulk liquid.

Bulk liquid	Refractive index
Water	1.3330
3 mM PBS	1.3333
6 mM PBS	1.3338
10 mM PBS	1.3346
Ethanol	1.3613
Isopropyl alcohol (IPA)	1.3770

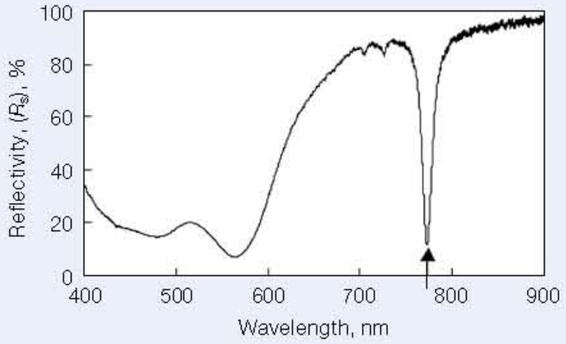

Fig. 8 Spectrum of the developed sensor substrate in water. The arrow indicates the peak wavelength.

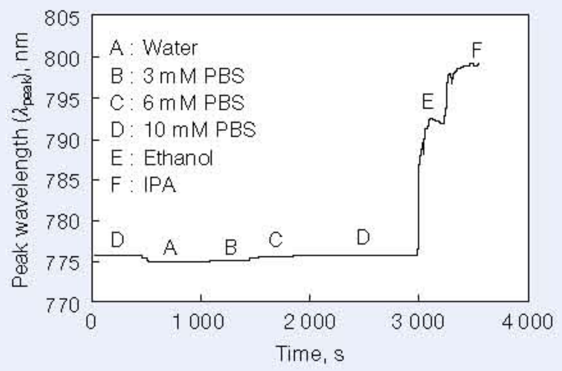

Fig. 9 Measurement behavior of the peak wavelength at the different refractive indexes.

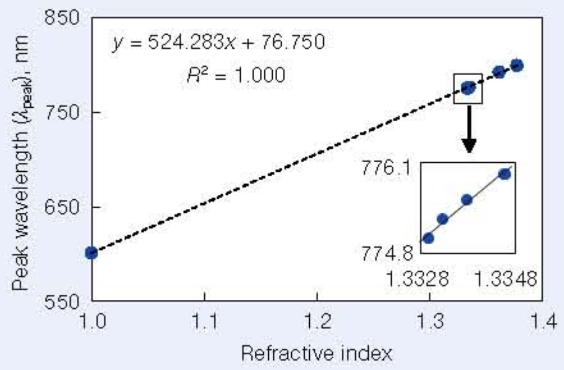

Fig. 10 Peak wavelength dependence on the refractive index.

5.5 Avidin-Biotin interaction

We demonstrated the avidin-biotin interaction on the sensor substrate as a proof of concept of the potential biomolecule detection system. Avidin and biotin are widely known as a pair which shows a considerably high affinity with the dissociation constant, $K_d = 10^{-15}$[11]. In order to immobilize biotin on the sensor substrate to interact with avidin, first the monolayer of AUT was formed on the sensor substrate. AUT has a linear hydrocarbon chain which has a thiol group at one end and an amino group at the other end. A thiol group forms a strong bond with gold[12]. The AUT molecules are well aligned to form a monolayer because of such a structure. The sensor substrate was immersed in 1 mM (mol/m^3) AUT ethanol solution for 20 hours followed by rinsed with ethanol and water. Biotin-NHS was used to immobilize biotin onto the monolayer surface. Biotin-NHS is a biotin derivative in which a carboxyl group of biotin is functionalized with N-Hydroxysuccinimide to form an ester which readily reacts with a primary amine to create an amide bond. The monolayer-formed sensor substrate was immersed in 1 mM Biotin-NHS 0.3 % DMSO aqueous solution for 1 hour followed by rinsed with water. The sensor substrate functionalized with biotin is set on the measuring system.

A series of avidin concentration solutions, 1, 3.3, 10, 33 and 100 nM, are added onto the sensor substrate to observe a real-time behavior of the avidin-biotin interaction. A typical shift of the peak wavelength is shown in Fig. 11. First, 10 mM PBS as a background buffer was transported to the sensor substrate. The peak wavelength shift appears stable until the point (~ 1 000 sec) at which 100 nM avidin PBS aqueous solution was applied. The addition of avidin solution led to a considerable red shift of the peak wavelength. It indicates that avidin has interacted with the biotin immobilized on the sensor substrate. This is in agreement with Eq. (1) which describes that the peak wavelength is proportional to refractive index surrounding the sensor substrate. After the peak wavelength shift became modest, 10 mM PBS was transported again to remove non-specific binding. The blue shift of the peak wavelength was observed with the second 10 mM PBS injection. This attributes to the removal of excess amount of avidin from the sensor substrate. The experiment ended at the stable wavelength shift of the second PBS injection. The final wavelength shift means the amount of avidin binding to biotin on the sensor substrate.

In case of an analysis with the final wavelength shift, considerable experimental time is required until the end of the second PBS behavior. Thus, we used the initial reaction velocity to evaluate the concentration dependence of avidin. The avidin-biotin interaction proceeds as follows:

$$[\mathrm{Avi}] + \alpha[\mathrm{Bio}] \longleftrightarrow [\mathrm{Avi{\cdot}Bio}_{\alpha}] \quad (4)$$

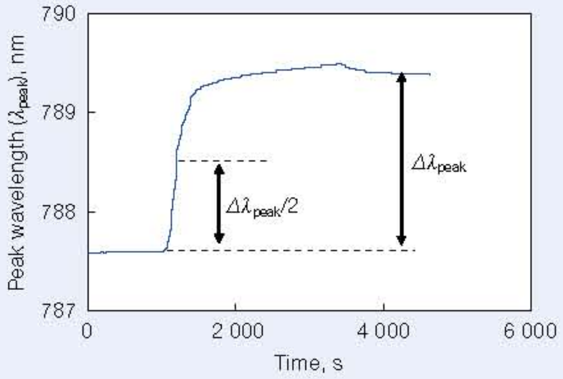

Fig. 11 Measurement behavior of the peak wavelength for 100 nM avidin.

where [Avi] and [Bio] represents the concentrations of the avidin and the biotin, respectively. [Avi·Bio$_\alpha$] is the concentration of the avidin-biotin complex, and α indicates the average number of biotin binding to one avidin because avidin is a tetramer. As already described, the dissociation constant of avidin-biotin interaction is very small and given by:

$$K_\mathrm{d} = \frac{k_\mathrm{off}}{k_\mathrm{on}} = 10^{-15} \tag{5}$$

where k_on and k_off are the rate constants. The reaction velocity of the avidin-biotin interaction is expressed as follows:

$$\frac{d[\mathrm{Avi} \cdot \mathrm{Bio}_\alpha]}{dt} = k_\mathrm{on}[\mathrm{Avi}][\mathrm{Bio}]^\alpha - k_\mathrm{off}[\mathrm{Avi} \cdot \mathrm{Bio}_\alpha] \tag{6}$$

here, the second term in the right side can be cancelled according to Eq. (5), and k_on and $[\mathrm{Bio}]^\alpha$ are considered constant. Hence, the reaction velocity of avidin-biotin interaction is proportional to avidin concentration. For calculating the reaction velocity, we used the reaction time at which the peak wavelength reaches at half the full peak wavelength shift. Figure 12 shows the relationship between the avidin concentration and the reaction velocity. The reaction velocity of the avidin-biotin interaction shows good correlation in linearity in both logarithmic scales.

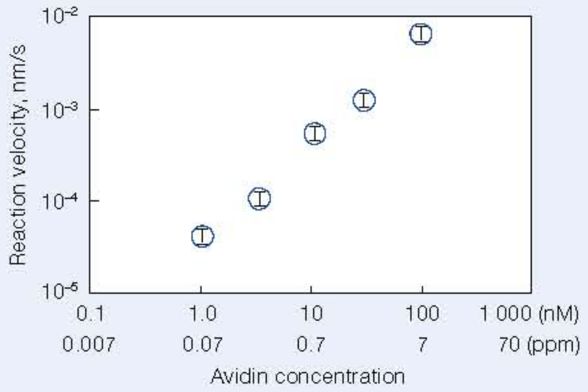

Fig. 12 Reaction velocity dependence on avidin concentration.

6. Conclusions

We developed a compact prismless surface plasmon resonance sensor by locating periodic nanostructures on the sensor substrate and also by embedding the collimator into the optical fiber. The developed sensor system is portable due to the simple structure. With the collimator-mounted optical fiber, the sensor system exhibits a stable real-time measurement signal even with the optical fiber 30 mm away from the sensor substrate. We showed that the peak wavelength derived from surface plasmon resonance shifts linearly along with the surrounding refractive index and a small difference 0.0003 of the refractive index was measured. We also demonstrated that the immobilized biotin on the sensor substrate interacted with avidin. The reaction velocity shows good correlation with avidin concentrations (1, 3.3, 10, 33 and 100 nM). It is concluded that the developed sensor system is a high-sensitive compact prismless SPR sensor.

Acknowledgement

We thank Prof. Fujii and Dr Kinoshita and Mr Oishi from The University of Tokyo, as well as Mr Furukawa, Ms Okutani, Mr Sasao, Dr Oguchi, and Dr Takajo from NSK Ltd. for advice and comments on the research.

References

1) H. Raether and E. Kretschmann, Radiative Decay of Nonradiative Surface Plasmons Excited by Light, Zeitschrift für Naturforsch, 23, pp. 2135–2136, 1968.
2) A. Otto, Excitation of Nonradiative Surface Plasma Waves in Silver by the Method of Frustrated Total Reflection, Zeitschrift für Physik, 216, pp. 398–410, 1968.
3) Jiri Homola, Present and Future of Surface Plasmon Resonance Biosensors, Analytical and Bioanalytical Chemistry, 377, pp. 528–539, 2003.
4) R. L. Rich and D. G. Myszka, Advances in Surface Plasmon Resonance Biosensor Analysis, Current Opinion in Biotechnology, 11 (1) pp. 54–61, 2000.
5) N. Nath, and A. Chilkoti, Label-Free Biosensing by Surface Plasmon Resonance of Nanoparticles on Glass: Optimization of Nanoparticle Size, Analytical Chemistry, 75, pp. 5370–5378, 2004.
6) M. E. Stewart, C. R. Anderton, L. B. Thompson, J. Maria, S. K. Gray, J. A. Rogers and R. G. Nuzzo, Nanostructured Plasmonic Sensors, Chemical Reviews, 108, pp. 494–521, 2008.
7) W. T. Ebbesen, J. H. Lezec, F. H. Ghaemi, T. Thio, A. P. Wolff, Extraordinary Optical Transmission through Subwavelength Hole Array, Nature, 392, pp. 667–669, 1998.
8) S. Yeom, O. Kim, B. Kang, K. Kim, H. Yuan, D. Kwon, H. Kim and S. Kang, Highly Sensitive Nano-porous Lattice Biosensor Based on Localized Surface Plasmon Resonance and Interference, Optics Express, 19 (23) pp. 22882–22891, 2011.
9) K. Nakamoto, R. Kurita, O. Niwa, T. Fujii and M. Nishida, Development of a Mass-Producible On-Chip Plasmonic Nanohole Array Biosensor, Nanoscale, 3, pp. 5067–5075, 2011.
10) S. Y. Chou, P. R. Krauss and P. J. Renstrom, Nanoimprint Lithography, Journal of Vacuum Science & Technology B, 14 (6) pp. 4129–4133, 1996.
11) J. Guesdon, T. Ternynck and S. Avrameas, The Use of Avidin-Biotin Interaction in Immunoenzymatic Techniques, Journal of Histochemistry and Cytochemistry, 27 (8) pp. 1131–1139, 1979.
12) L. H. Dubois and R. G. Nuzzo, Synthesis, Structure, and Properties of Model Organic Surfaces, Annual Review of Physical Chemistry, 43, pp. 437–463, 1992.

Keisuke Yokoyama

Marie Oshima

Bearing Torque Characteristics of Lithium Soap Greases with Some Synthetic Base Oils

Eri Watabe, Noriyuki Inami, Michita Hokao, and Atsushi Yokouchi
NSK Ltd.
Joichi Sugimura
Kyushu University, Department of Mechanical Engineering

ABSTRACT

This paper describes the influence of rheological properties on the bearing torque characteristics of the lithium soap greases with five types of base oils. The greases used had different yield stress depending on the base oils even with the same thickener concentration. Measurement of bearing torque was conducted for a deep-groove radial ball bearing by using a bearing test apparatus. The bearings filled with greases initially exhibited high torque but showed gradual decrease in the torque with prolonged rotation, where the greases with higher yield stress showed larger normalized torque decrease. Observation of bearing after the rotation revealed a tendency that the greases with larger normalized torque decrease had been pushed aside in the raceway by channeling. This implied that the greases with higher yield stress tended to show channeling. On the other hand, the greases with lower yield stress circulated within the bearing by churning and showed smaller normalized torque decrease. These behaviors are explained in terms of the yield stress of the greases and the shear stress to entrain the greases into the contacts. Observation of grease structure was made with atomic force microscopy showed that the greases whose thickener network structure was distributed more densely had higher yield stress.

Reprinted with permission from SAGE Publication Ltd., Proc IMechE Part J: Journal of Engineering Tribology 226 (6) 575-583.

1. Introduction

Lithium soap thickened greases account for approximately 60 percent of the grease used in the world because of their well-balanced properties1). The thickener fibers distributed in the grease form a three dimensional fiber structure, and oil is held by a combination of interactive force and capillary force within the pockets formed by the network2). In this paper, the network formed by thickeners is described as the grease structure. Greases show complicated behavior in contrast with oil because the grease structure is dramatically changed by shear stress. Recent studies have shown that thickeners play an important role in lubrication3).

Cann et al. focused on the role of thickener type and showed that EHL film formation in the starved regime depended on grease rheology and that lubricant replenishment to the contact was determined by yield stress and shear stability3). Yokouchi et al. focused on the influence of fiber length of lithium-soap thickener of grease on friction coefficient under boundary lubrication conditions. The ball-on-disk friction tests revealed that the greases had a lower friction coefficient than the base oil. The grease with a long soap fiber structure had a lower friction coefficient than that for short soap fiber structure. The grease with longer soap fibers was easily entrained into the contact because of its lower viscosity and lower yield stress. This entrainment capability of the grease led to favorable lubrication to maintain low friction coefficient4).

However, the rheological behaviors of greases in rolling-contact bearings are more complex as it does not only affects traction at EHL conjunctions but also affects their flow in the bearings, which may cause resistance to the motions of rolling elements. Hutton described the initial stage of bearing operation known as clearing stage, in which grease was redistributed and deposited in the bearing recesses, was very important for the proper functioning of the bearing, and reported the clearing characteristics was influenced by grease rheological properties5).

Considering that the grease structure is one of the key factors affecting physical properties and lubrication of greases, it must also have a great influence on bearing torque. Therefore, it is necessary to understand the influence of the grease structure on lubrication of bearings in order to improve bearing performances. However, few studies have focused on the relationship between bearing torque and rheological properties and their relations with the grease structure6).

In this study, the influence of rheological properties on bearing torque characteristics is investigated. Lithium soap greases with five different types of base oils are used to examine the effect of the grease structure, and hence the rheological properties, on the generation of torque.

2. Experimental

2.1 Test greases

Test greases were composed of lithium 12-hydroxystearete thickener and five types of base oils of poly alpha olefin (PAO), carbonate ester (COE), polyol ester (POE) and two types of poly alkylene glycol (PAG) with the same range of viscosity and different relative dielectric constant. Their properties are shown in Table 1.

The greases were prepared by dissolving the thickener in the base oil at up to 503 K, water-cooled by pouring it on a stainless tray, and then passing it through a three roll mill. Thickener concentration was 11 mass% and no additives were contained in the greases. Grease penetration was greatly changed with the base oils having different relative dielectric constant at the same thickener concentration. This phenomenon should be investigated and addressed in the future work. In addition to the five greases, greases with different thickener concentration were also prepared for three types of base oils of PAO, POE and PAG-3. These grease properties are shown in Table 2.

2.2 Rheological measurement

Rheological characteristics were evaluated by a rheometer with a parallel plate. Apparent viscosity and yield stress of the greases were measured at 303 K.

Apparent viscosity measurements were made as follows. Shear rate was increased stepwise from 0.01 s^{-1} to 4 800 s^{-1} every two minutes. The viscosity after two minutes at each shear rate was defined as apparent viscosity to exclude time-dependence of apparent viscosity of greases.

Yield stress was measured in oscillating tests. Shear stress was increased continuously from 10 Pa to 5 000 Pa at 10 Hz. Yield stress was defined as the shear stress value when loss tangent G'' / G became 1 7). A viscous behavior of greases represented by loss modulus G'' becomes dominant compared with an elastic behavior represented by storage modulus G' when loss tangent are more than unity.

2.3 Bearing torque measurement

Bearing torque was measured by detecting the force generated at the outer ring when the inner ring was rotated. Figure 1 shows a schematic diagram of the test apparatus. Deep-groove radial ball bearings 6305 with bore diameter 25 mm were used for the tests. The tests were conducted at a rotating speed of 1 800 rpm, a radial load of 29.4 N, and an axial load of 294.2 N and at ambient temperature. The grease of a volume of 35 % of the vacant space in a bearing was uniformly filled between balls and rings, and tests were started. Tests were conducted without a running-in period in order to make sure that the grease distribution at the start of the tests was the same in all the tests. Test duration time was ten minutes. Non-contact rubber seals were set on the bearing during the rotating tests. The maximum torque during initial period and the mean torque averaged over last 20 seconds were obtained as the initial torque and the steady-state torque, respectively. Measurement was made three times for each grease sample, and their average value was plotted.

Separate tests were conducted in order to observe flow of grease in the bearing by using the grease added with red dyes as a tracer. The tracer grease was put on a prescribed position after the fresh grease was filled in a bearing uniformly. Visual observation of the distribution of the tracer dyes on the tested bearing was conducted after rotating the bearings with the same conditions as in the above torque measurement tests.

Table 1 Properties of greases

Grease	PAO	COE	POE	PAG1	PAG3
Base oil type	PAO	COE	POE	PAG	
Base oil viscosity at 313 K, mm²/s	31	31.6	30.5	32.8	29.8
Base oil relative dielectric constant at 1 MHz	2.1	2.2	2.3	5.4	8.1
Worked penetration at 298 K	282	262	212	240	310

Table 2 Properties of greases with different thickener concentration

Grease	PAO			POE		PAG3	
Thickener concentration, %	14	15	16	3	6	16	18
Worked penetration at 298 K	240	222	193	328	269	250	212

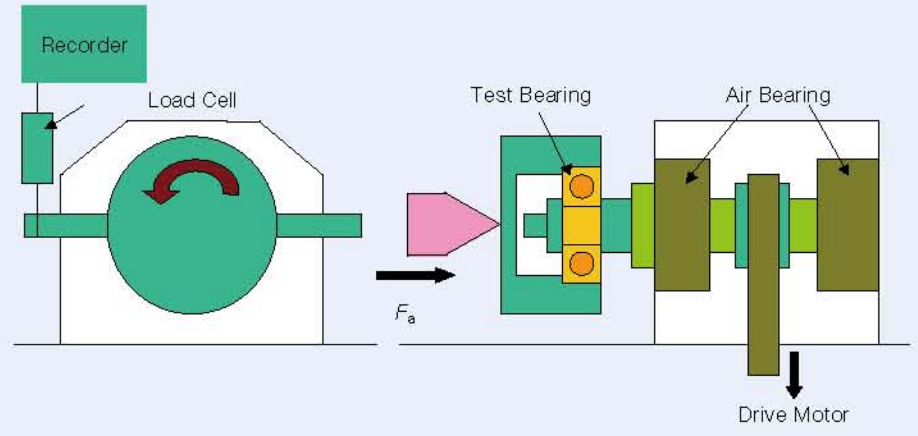

Fig. 1 Schematic diagram of the bearing torque test apparatus

3. Results and discussion

3.1 Rheological characteristics

Greases show non-Newton characteristics and have a yield stress. Grease fluidity is also characterized by shear thinning and thixotropic properties attributed to shear-rate-dependence and time-dependence of the apparent viscosity[8]. These rheological characteristics must be influenced by the grease structure.

Figure 2 shows the shear-rate-dependence of the apparent viscosity of PAO. The apparent viscosity at infinitely large shear rate indicated by a dotted line was calculated by the following equation (1) proposed by Casson:

$$\sqrt{\tau} = a\sqrt{\dot{\gamma}} + b \tag{1}$$

Where τ is shear stress, $\dot{\gamma}$ is shear rate, a^2 is apparent viscosity at infinity of shear rate and b^2 is yield stress. The coefficient "*a*" in equation (1) was experimentally determined by measuring viscosity at shear rates of 460s^{-1}, 1 000 s^{-1}, and 4 800 s^{-1}. Casson plot was made with good correlation with the shear rate above 460 for all the greases. The correlation coefficient of the plot was above 0.98. The apparent viscosity greatly decreased with increasing of shear rate. This was common to all the greases used in this study.

Figure 3 compares the apparent viscosities at the shear rate of 0.01 s^{-1} and infinity. Shear rate of 0.01 s^{-1} was the lowest shear rate that can be set with the rheometer used. At the shear rate of 0.01 s^{-1} where grease begins to flow, the apparent viscosity of POE with large worked penetration shows high value and that of PAG-3 with small penetration indicated low value. On the other hand, apparent viscosities of all greases were comparable at the shear rate of infinity. Young reported greases behaved like solids at low shear stress levels and like liquids at high shear stress levels[9]. In this work, the base oil viscosities are almost the same. This suggests that the apparent viscosity of the greases at high shear rate approaches to that of the base oils.

Figure 4 shows the yield stress of the greases. The yield stress was measured with oscillating tests based on the assumption that the grease in the bearing was sheared periodically. It can be seen that the yield stress varies depending on the base oil types despite the thickener concentration was the same. The POE grease with large penetration indicated high yield stress and the PAG-3 grease with small penetration indicated low yield stress. This result agrees with the apparent viscosity at the shear stress of 0.01 s^{-1} shown in Figure 3 (a).

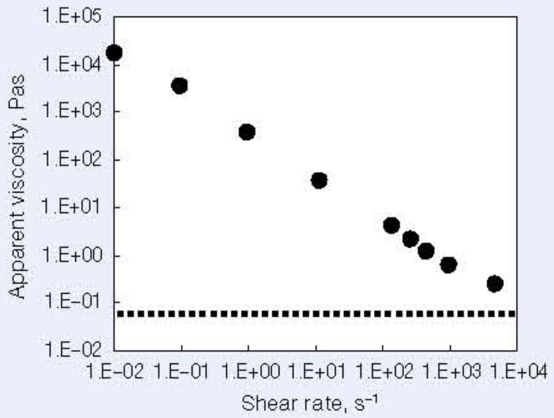

Fig. 2 Shear-rate-dependence of the apparent viscosities of PAO grease

3.2 Bearing torque characteristics

3.2.1 Flow of grease in bearing

Figure 5 shows the experimental results of changes in the bearing torque with time for the POE and PAG-3 greases. The torque with PAG-3 grease stayed almost flat. On the other hand, the torque with POE grease significantly decreased at the initial stage of duration before it became constant.

In order to investigate the rheological behavior of the greases in the bearings, flow of the grease in the bearing after rotating test was observed by using the grease added with dyes as a tracer. Figure 6 shows the distribution of the dyes on the grease filled in bearings after rotating tests. The dyes of PAG-3 grease were distributed uniformly in the bearing and this indicated PAG-3 grease was circulated through the bearing. In contrast, the dyes in POE grease was seen partially in the bearing; particularly, the dyed grease was not distributed in the outer ringside.

Two remarkable rheological characteristics for greases in a bearing are well known. One is churning, and the other is channeling. The grease with churning tends to be stirred continuously in a bearing during operation.

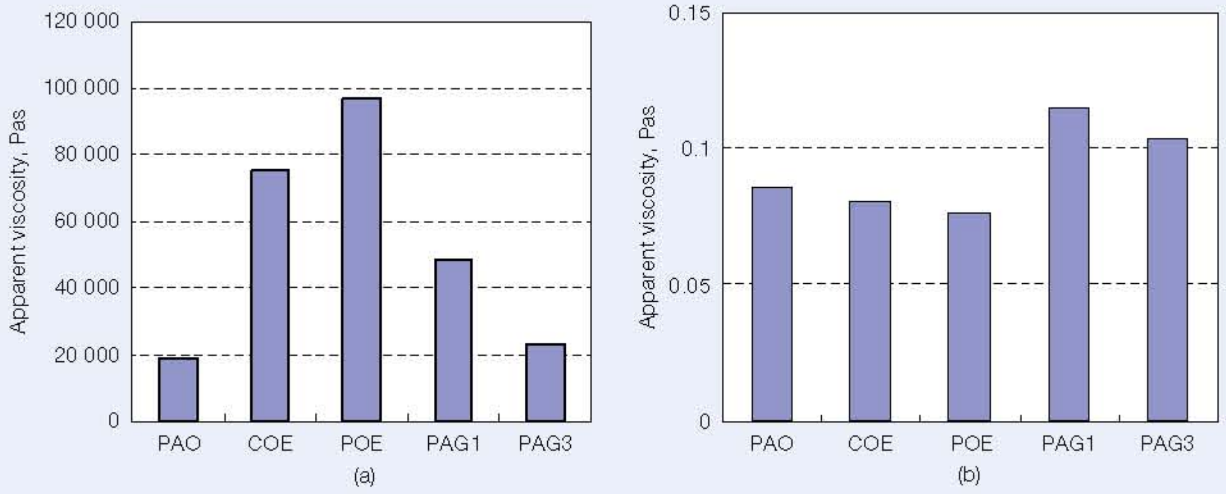

Fig. 3 Apparent viscosity of tested greases at shear rate of (a) 0.01s^{-1}, (b) ∞

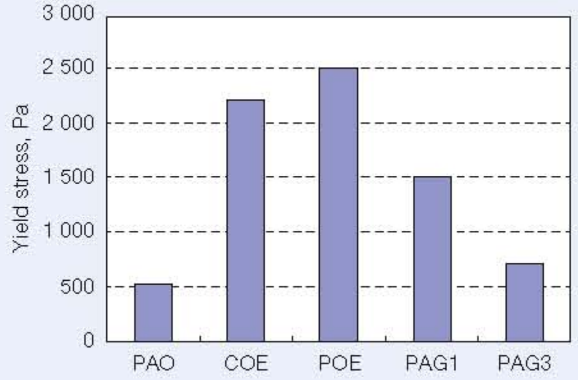

Fig. 4 Yield stress of tested greases

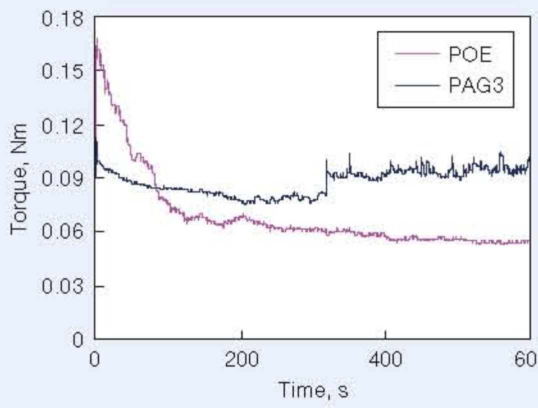

Fig. 5 Comparison of bearing torque of POE and PAG-3 greases

On the other hand, the grease that channels tends to be excluded from initial position, and redistributed to the side of a contact area during the initial stage of a bearing operation. While a grease channels, a small quantity of grease remains at the contact area to maintain lubrication. The observation of the grease using the tracer indicates that PAG-3 grease tends to be churning, and POE grease tends to be channeling. The observation results similarly indicate that PAO grease tends to be churning and COE and PAG-1 greases tends to be channeling.

3.2.2 Factors of bearing torque generation

Distribution of grease in a bearing, which could cause a difference in shear resistance of the bearing, may influence bearing torque. Grease is sheared within lubricating film at the contact point, surrounding area of the contact between balls and races, areas between balls and a cage, and areas between a cages and seals10). Yokouchi et al. reported the grease affects the friction at the contact point4). The above results suggest that the redistribution of grease in the bearing also affects the bearing torque. In order to investigate their contributions, the resistance with lubrication film at the contact point and the torque generated in other areas of the bearing are now estimated.

The oil film parameter Λ was approximately 5.6 in this test condition. The total frictional torque T of a rolling bearing at mild operating condition consists of two main torques11) as described in equation (2),

$$T = T_0 + T_1 \qquad (2)$$

T_0 represents the torque generated by stir of the lubricant and it does not depend on load. T_1 represents the torque at the contact point and it depends on load.

By calculations based on specifications for the shape and dimensions of the bearing and the properties of greases, T_1 is estimated to be approximately 15 % of the whole torque T under this condition. Therefore, it is likely that the bearing torque is greatly influenced by the stirring resistance of the grease.

The shear rates that the greases experience in the bearing depends on a rolling velocity and distributed position. Because the grease was uniformly filled between balls and races before the test, the grease distributed between balls and races could most influence the torque in the initial stage of the rotation.

Shear rate at the gap between a ball and a ring decrease with distance from the contact point due to diverging gap between the surfaces. The shear rate was roughly estimated to 10^6 s^{-1} at the contact point and 400 s^{-1} at the edge of the ball of the tested 6305 bearing at a rotational speed of 1 800 min^{-1}. This difference in the shear rate could correspond to the increase of apparent viscosity by seventeen times at the edge of ball from that at the contact point for PAO grease shown in Figure 2. Therefore, the high shear stress is generated at the front and the sides of the contact area where shear rate is low. This increases the bearing torque significantly.

3.2.3 Initial torque and steady-state torque

Figure 7 shows the initial torque and the steady-state torque of the tested greases. The grease in the bearing is sheared at the initial position after the bearing was started to rotate, and consequently the torque is generated with the same grease distribution for all the greases. Because of this, the initial torque is high because there is a large amount of grease at the positions in the bearing where the shear stress is high.

Fig. 6 Distribution of the dyes on the grease filled in bearings after rotation tests
(a) POE grease (b) PAG-3 grease

As indicated above, the steady-state torque of the greases with different rheological characteristics is assumed to be greatly affected by the redistributed position of the grease in the bearing. It is likely that a large volume of grease stay between balls and races for the churning grease of PAO and PAG-3, continuously circulating within the bearing. Therefore, the steady-state torque of these greases maintains high because there is a large amount of grease at the positions in the bearing where the shear stress is high. On the other hand, in the case of the grease with channeling such as COE, POE and PAG-1, the steady-state torque is low because substantial amount of the grease is excluded from the contact track where the grease would exhibit higher shear force under low shear rate. This must lead to the large torque decrease from initial torque for the channeling greases.

Figure 8 shows the torque decrease from initial torque. PAO and PAG-3 greases show the decrease less than 0.02, whereas COE, POE, and PAG-1 greases show the decrease above 0.04. Especially, POE grease shows a large decrease of approximately 0.1. The channeling grease thus shows the large torque decrease from initial torque.

3.2.4 Influence of grease properties on torque characteristics

Plastic flow of grease may hardly occur by a shear stress below the yield stress where an elastic behavior is dominant, and thus the grease is excluded from the contact area. In order to examine the condition for a grease to flow, the shear stress between balls and races is plotted against the distance from the contact center for POE and PAG-3 greases in Figure 9. The yield stresses of the greases are also shown with dotted lines. A grease flows when it is sheared at a stress larger than its yield stress. Figure 9 demonstrates that the POE grease yields near the contact area and the PAG-3 grease yields near the edge of a ball. This suggests that the PAG-3 grease is more entrained into the contact area than the POE grease. As a result, the POE grease shows low steady-state torque because small amount of grease remained between balls and races by the exclusion of the excess grease at the contact area. In contrast, the PAG-3 grease maintains high steady-state torque because a large amount of grease remains around the contact area. Thus the grease entrainment capacity to the contact area is expected to depend on yield stress.

In order to see if there is a quantitative relationship between the torque decrease from initial torque and the yield stress, the torque decrease from initial torque is plotted against the yield stress in Figure 10. The figure clearly shows that the grease with higher yield stress shows larger torques. In other words, the grease with higher yield stress tends to show channeling.

The decrease in the torque and the yield stress is measured also for the greases with different thickener concentration as listed in Table 2. Figure 11 shows the variation of the yield stress with thickener concentration,

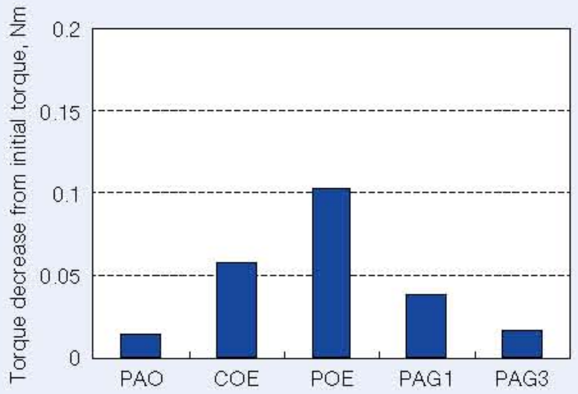

Fig. 8 Torque decrease from initial torque of tested greases

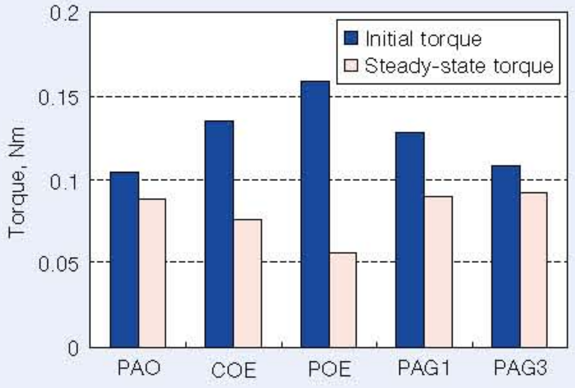

Fig. 7 Initial torque and steady-state torque of tested greases

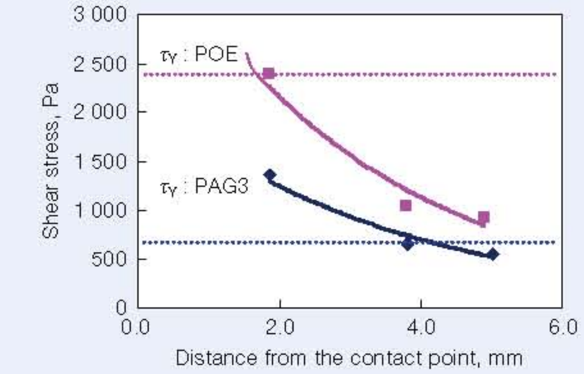

Fig. 9 Shear stress between a ball and a ring with distance from the contact point

which clearly indicates that the yield stress increases with the thickener concentration.

Variation of the torque decrease for all the tested grease and base oils with their yield stress is shown in Figure 12. Plotted in the figure is the normalized torque decrease T_d defined by

$$T_d = (T_i - T_s) / T_i \quad (3)$$

Where T_i is the initial torque and T_s is the steady-state torque. The figure demonstrates that the normalized torque decrease increases with the yield stress. The symbol τ_Y represents yield stress. The relationship shown in Figure 12 is expressed as follows:

$$T_d = 9.6\,\tau_Y + 27.1 \quad (4)$$

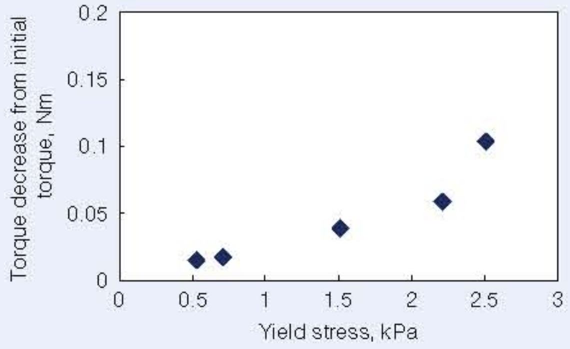

Fig. 10 Torque decrease from initial torque against to the yield stress

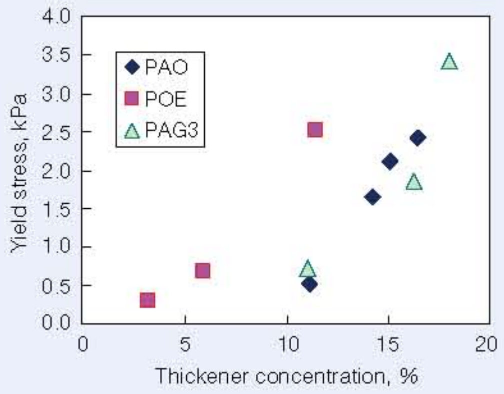

Fig. 11 Yield stress of the greases with different thickener concentration

The correlation coefficient of the equation is 0.818.

The above discussion on the relationship between torque and channeling are summarized as follows.

i) Shear resistance force of greases is large where the shear rate is low, i.e. at the contacts between balls and races but at some distance from the contact center. This increases the bearing torque.
ii) The initial torque is high because there is a large amount of grease at the positions in the bearing where the shear stress is high.
iii) The steady-state torque of the channeling grease is low because substantial amount of the grease is excluded from the contact track where the grease would exhibit higher shear force under low shear rate.

These points imply that T_s depends on the ratio of the excluded volume of grease from the position where shear rate is low. The ratio may depend on physical property of the grease, the parameter of the bearing and an operating condition. The yield stress τ_Y represents the physical property of the grease, and the coefficient 9.6 of equation (4) corresponds to the parameter of the bearing and an operating condition. A physical meaning of equation (4) may be as follows; the yield stress τ_Y represents the ability to channel in the allowed space and the coefficient 9.6 represents the possible space for grease to channel between balls and races. A torque decrease of near 100 % may occur when the grease is almost excluded from allowed space. The yield stress at T_d= 100 % is estimated to be 7.6 kPa from equation (4). In practice, the range of the torque decrease is from 20 % to 60 %, which implies that the yield stress for largest torque decrease is 4 kPa.

3.2.5 Grease structure

The mechanical properties and the behavior of the greases shown in the previous sections should be related with the network structure of thickeners. In order to explore the grease structure, direct observation of a three dimensional fiber structure was made with the atomic force microscopy, AFM. Distribution of thickeners on the virgin grease surface was observed by AFM. Surface observation in this way corresponds to observation of cross-section of inside of grease. Grease was applied to a flat glass plate in a form of thin layer. AFM measurements were made in dynamic force mode, and in more detail in phase mode. Figure 13 shows AFM images of PAG-1 with different thickener concentrations. The images show that the network structure is partially formed in the grease with larger thickener concentration. Measurement was made for two or three views, and it was confirmed that they showed the same tendency.

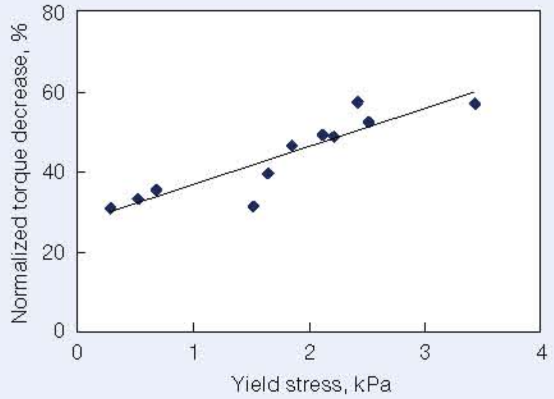

Fig. 12 Relationship between yield stress and torque decrease

Figure 14 shows the AFM images of greases with different type of base oils and the same thickener concentration. The network of thickeners distributes sparsely in PAO and PAG-3 greases, while the network distributes densely in POE grease. The images for PAO and PAG-3 greases appear similar to that of 12 % of PAG-1, and the image of POE is similar to that of 14 % of PAG-1 shown in Figure 13. This implies that the grease structure with different type of base oils corresponds to the grease structure with different thickener concentrations. More quantitative analysis of the grease structure will be addressed in the future work.

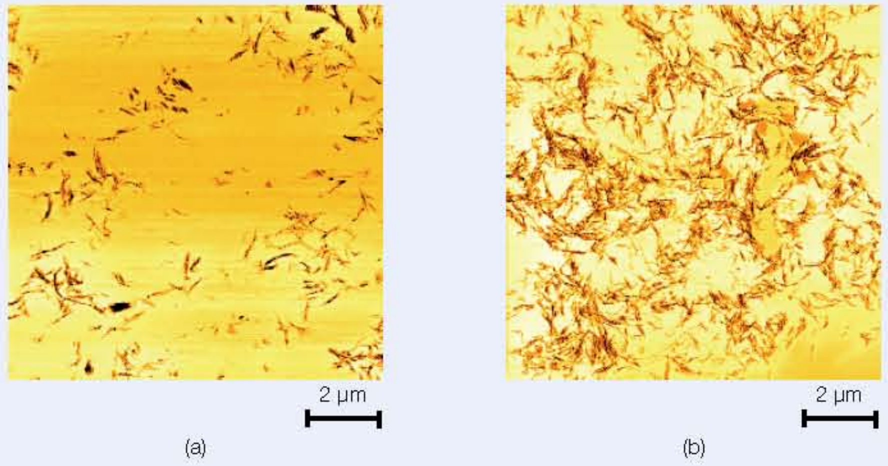

Fig. 13 AFM images of PAG-1 grease with different thickener concentrations, (a) 12 %, (b) 14 %

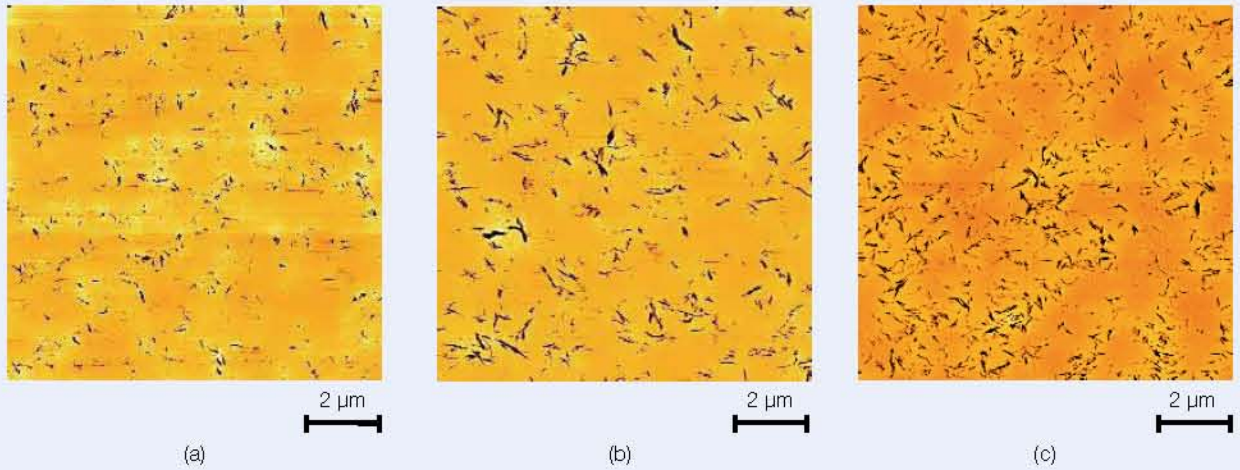

Fig. 14 AFM images of the greases with different type of base oil at same thickener concentration of 11%, (a) PAO, (b) PAG-3, (c) POE

4. Conclusions

Rheological properties and bearing torque characteristics of lithium soap greases with five types of base oils were studied in this paper. The results are summarized as follows.

(1) The bearing torque with the greases depends on the high shear stress where shear rate is low.
(2) The greases with higher yield stress tend to show channeling, and provide lower steady-state torque. These greases are not easily entrained into the contact area, but redistributed to the front and the sides of a contact area during the initial stage.
(3) The greases with lower yield stress tend to show churning, and maintain high steady-state torque. This is because a large volume of grease is remained between balls and races.
(4) The POE, COE, and PAG-1 greases show channeling among tested grease of five types of base oils.
(5) The grease network structure depends on base oil, and the greases whose thickener network structure is distributed more densely have higher yield stress.

References

1) Kimura. H., and Imai, Y., Study on Fiber Length Control for Ester-Based Lithium Soap Grease, Tribology Transactions, 44, 3 (2001) 405.
2) Cann, P. M. and Spikes, H.A., Fourier-Transform Infrared Study of the behavior of grease in Lubricated Contacts, Lubrication Engineering, 48, 4 (1992) 335–343.
3) Hurley, S. and Cann, P.M., Starved Lubrication of EHL Contacts-Relationship to Bulk Grease Properties, NLGI Spokesman, 64, 2 (2000) 15–23.
4) Yokouchi, A., Hokao, M. and Sugimura, J., Effects of Soap Fiber Structure on Boundary Lubrication of Lithium Soap Greases, Tribology Online, 6, 4 (2011) 219–225.
5) Hutton, J.F., The Influence of Flow Elasticity on the Bearing Performance of Lubricating Grease, Proc. JSLE-ASLE International Lubrication Conference (1975) 707–714.
6) Thelen, E., Devine, M.J. and Stallings, L.J., The Starting Torque and Rheology of Lubricating Grease at Low Temperature, Lubrication Engineering, 27, 9 (1971) 301–310.
7) Couronne, I., Blettner, G. and Vergne, P., Rheological Behavior of Grease: Part I - Effects of Composition and Structure, Tribology Transactions, 43, 4 (2000) 619–626.
8) Meng, Y. and Zheng, J., A rheological model for lithium lubricating grease, Tribology International, 31, 10 (1998) 619–625.
9) Young, I. C. and Eunsoo, C., The Rheology and Hydrodynamic Analysis of Grease Flows in a Circular Pipe, Tribology Transactions, 36, 4 (1993) 545–554.
10) Wikström, V. and Höglund, E, Starting and Steady-State Friction Torque of Grease-Lubricated Rolling Element Bearings at Low Temperatures, Tribology Transactions, 39, 3 (1996) 684–690.
11) Brändlein, J., et al., Ball and Roller Bearings: Theory, Design and Application, Japanese version edited by Yoshitake. T., Kogyochousakai, 1996, 198–202.


Eri Watabe


Noriyuki Inami


Michita Hokao


Atsushi Yokouchi


Joichi Sugimura

Evaluation of Lubrication Properties of the 100 % Food-Derived Grease for Rolling Bearings

Eri Watabe, Yujiro Toda, Kanako Tsumura and Koichi Hachiya
NSK Ltd.

Translated and reprinted from Preprinted Paper for Tribology Conference 2013 autumn Fukuoka A20 with permission from JAST.

1. Introduction

Many raw materials that are used for lubricating grease are petroleum-derived. With recent increases in safety and health consciousness by consumers and companies, however, demands are increasing for lubricants that consist of safer ingredients.

For instance, lubricating grease that meets category code H1 (standard of lubricant with incidental food contact) of the National Sanitation Foundation (NSF) is being used for rolling bearings in food and drug manufacturing machinery. However, the following problems exist even with this registered NFS H1 grease:

1) Although the grease can be used at places where there is a risk of contact with foods incidentally, it does not consist of edible ingredients.
2) Because the usable ingredients are restricted by the standard, performance is lower compared with lubricating grease for general industry.

Therefore, NSK developed a lubricating grease that consists of a base oil, thickener, and additive with 100 % food-derived ingredients and evaluated bearing performance with the new grease in this study. The study found that bearing lubrication performance was equivalent to general-purpose grease, and the results are introduced here.

2. Test Method

2.1 Test grease

The ingredients of the developed grease are as follows:

(1) Base oil: Medium-chain triglyceride (MCT)
(2) Thickener: Food additive
(3) Additive: Antioxidant agent for food

For comparison, two other greases were used: a general-purpose grease made of mineral oil-based lithium soap and a commercial food grade grease made of PAO-based aluminum-complex soap.

2.2 Test method

2.2.1 Standard test

In accordance with ASTM standards, general properties of the developed grease and the compared grease were evaluated by various methods such as copper-strip and standard corrosion tests, a wear test using four balls, and a water washout test.

2.2.2 Bearing rotation test

Grease leakage tests, torque tests, high-speed rotation tests, and acoustic life tests of a bearing packed with the developed grease and bearings packed with the compared grease were carried out. Test conditions are shown in Tables 1, 2, 3 and 4.

3. Results and Discussion

3.1 General properties

Table 5 shows the standard test results. The developed grease has a low dropping point at 112 ℃, but oil separation is small. It passed the copper-strip corrosion test.

Additionally, the developed grease does not contain a rust-preventive agent or wear-resistant agent, but it showed good results in rust-preventive properties and wear properties using four balls. This is thought to be because the triglyceride used for the base oil has high adsorption performance to surfaces$^{1)-3)}$.

It was confirmed that the developed grease had the most resistance to water in the water washout test. This is thought to be because the grease tends to remain inside the bearing because of its small worked penetration.

From the above results, the general properties of the developed grease were confirmed to be equivalent to those of general-purpose grease and commercial food grade grease.

Table 1 Grease leakage test conditions

Bearing	Axial load N	Speed rpm	Prepacked grease amount g	Environmental temperature °C
6203VV	196	1 800	1	80 to 120

Table 2 Torque test conditions

Bearing	Axial load N	Speed rpm	Prepacked grease amount g	Environmental temperature °C
6203VV	196	1 800 to 7 500	1	Ambient temperature

Table 3 Bearing high-speed test conditions

Bearing	Axial load N	Speed rpm	Prepacked grease amount g	Environmental temperature °C
6210VV	1470	1 800 to 7 500	4.3	Ambient temperature

Table 4 Acoustic life test conditions

Bearing	Axial load N	Speed rpm	Prepacked grease amount g	Environmental temperature °C
6203VV	196	5 000	1	90

Table 5 General properties of test greases and standard test results

Items	Developed grease	General-purpose grease	Commercial food grade grease
Thickener	Food additive	Lithium soap	Aluminum-complex soap
Base oil	MCT	Mineral oil	PAO
Additive	Antioxidant agent	Petroleum based	Petroleum based
Base oil viscosity at 40 °C, mm^2/s	14.8	130	150
Base oil pour point, °C (JIS-K2266)	−17.5	−17.5	−52
Worked penetration (ASTM-D217) at 25 °C, 0.1 mm	255	275	280
Dropping point, °C (ASTM-D566-76)	112	181	258
Oil separation (ASTM-D566-76) at 100 °C, 24 hours	0.1	0.7	3
Copper strip corrosion test (ASTM-D130) at 100 °C, 24 hours	Passed	Passed	Passed
Corrosion preventive property (ASTM-D1743) at 52 °C, 48 hours	No rust	No rust	Rusted
Wear scar diameter by four ball test, mm (ASTM-D2266) at 200 N, 75 °C, 1 hour	0.46	0.56	0.97
Water washout, % (ASTM-D1264) at 38 °C, 1 hour	1	2	7.6

3.2 Bearing rotation test

3.2.1 Grease leakage test

Figure 1 shows the developed grease's leakage test results after 20 hours. Due to the thermal analysis results obtained by DSC, the test was carried out at a temperature of less than 90 °C because the thickener started to dissolve at temperatures near 100 °C. While the leak rate of the general-purpose grease uses a temperature of 120 °C as standard, the leak rate of the developed grease is low, up to 90 °C, and the service temperature limit should be set at 90 °C.

3.2.2 Torque test

Figure 2 shows the torque test results. The running torque of a bearing packed with the developed grease was less than 50 % of that with a bearing packed with general-purpose grease. This is because the base oil kinematic viscosity is approximately 1/10.

3.2.3 High-speed test

Figure 3 shows the high-speed test results. As can be inferred from the bearing torque, the developed grease showed a low temperature rise, even at high d_mN. Additionally, the developed grease showed the least rise in temperature with increasing speed, and showed low heat generation, even at high speed.

3.2.4 Acoustic life test

Figure 4 shows the acoustic life test results. Anderon values of the developed grease remained at a low level from the initial period, and it was found that it was superior in durability.

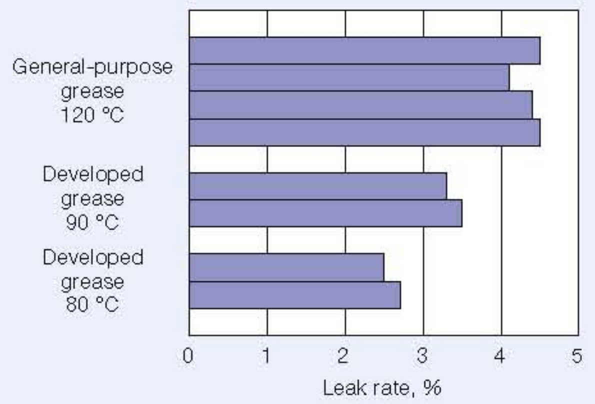

Fig. 1 Grease leakage test results (20 hours)

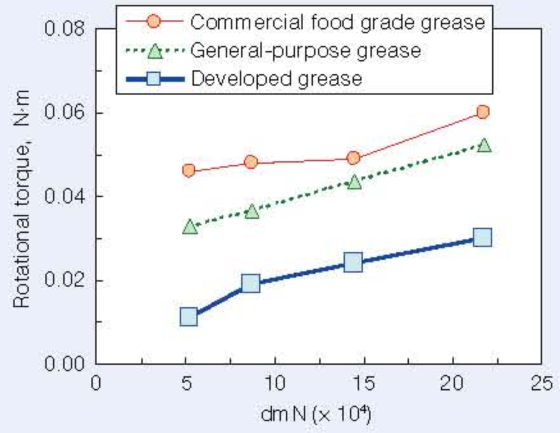

Fig. 2 Torque test results

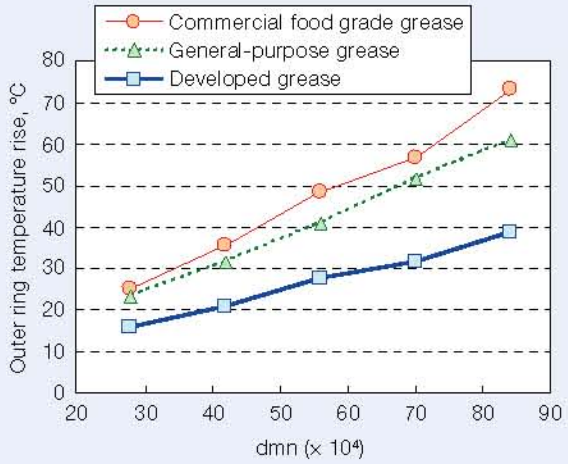

Fig. 3 High-speed test results

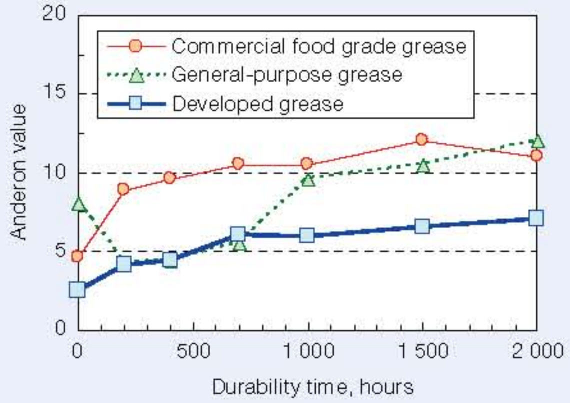

Fig. 4 Acoustic life test results

4. Conclusion

NSK developed a 100 % food-derived grease consisting of a base oil, thickener, and additive, and carried out various evaluation tests. The following results were obtained:

- The food-derived grease's dropping point was low (112 °C), but it was superior in corrosion resistance, wear resistance, and water resistance, and the grease had other general properties equivalent to those of general-purpose grease.
- Using the developed grease resulted in low torque and low heat generation at low to high speeds.
- The developed grease showed good durability in the acoustic life test.

In addition, the developed grease has been registered in the safer category code H3 (standard of lubricant with direct food contact) as well as NFS category code H1.

References

1) Mori et al., Proceedings for tribology meeting (Fukui 2010–10) 307–308.
2) Atanu Adhvaryu, et al., Ind. Eng. Chem. Res., 45, 10 (2006) 3735–3740.
3) N. H. Jayadas, K. Prabhakaran Nair, J. Tribol. 129, 2 (2007) 419–424.


Eri Watabe


Yujiro Toda


Kanako Tsumura


Koichi Hachiya

Increasing Sizes of Wind Turbines and Bearing Trends

Tasuku Suzuki
NSK Deutschland GMBH
Masafumi Fukunaga
Industrial Machinery Bearing Technology Center

Partly corrected, translated and reprinted with permission from Japan Wind Energy Association, Journal of Wind Energy, JWEA Vol. 37 No. 4 (Serial No. 108) February 2014.

1. Introduction

If a wind turbine breaks down, it reduces the operating production of the facility and creates an enormous expense for the repair and replacement of components. Therefore, high reliability is necessary for wind turbines. Since the latter half of the 1980s, NSK has supplied various components of wind turbines that require reliability and economic efficiency.

Recent enlargement of wind turbine size, the demands of bearings used for those, and the NSK-developed bearings based on these demands and changes are discussed in the following sections.

2. Increasing the Size of Wind Turbines

Recently, the size of wind turbines has been increasing.

Better installation efficiency of generators on the ground with approximately 3 MW of wind-power generation has led to increasing numbers of new placements of 2 to 3 MW wind turbines. In addition, the repowering (Figure 1) of aged, small- and middle-sized wind turbines that have already been placed with this class of efficient wind turbines is proceeding. Presently, this class covers 80 % of total wind turbines1).

On the other hand, constructing wind turbines with capacities greater than 2 to 3 MW is efficient on the sea, and development of generators with capacities over 5 MW continues to proceed. Investigation and research into 10 MW generators started this fiscal year as a project of the New Energy and Industrial Technology Development Organization (NEDO) in Japan.

As just discussed, production of 3 MW generators on the ground and further enlargement of generators on the sea are proceeding.

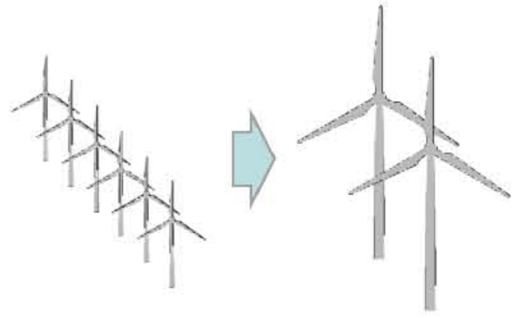
Aged, small-capacity facilities are replaced with large, high-efficiency facilities. This process is eligible for subsidies in Germany.

Fig. 1 Re-powering

3. Bearings for Large-Sized Wind Turbines

Figure 2 shows the components and bearings used inside each in general wind turbines. The drivetrain of a wind turbine consists of the main rotor shaft, a gearboxes, and the generator itself, and bearings are used in each of these parts. one to 2 ultra-large bearings with bore diameters of approximately 1 to 2 m are used for the main rotor shaft, ultra-large and large bearings are used to support the numerous gear shafts of gearboxes, and large bearings are used for both sides of the rotor for the generator.

The bearings used in each part are described below.

3.1 Bearings for main rotor shafts

Bearings with a bore diameter of over 1 m have been adopted in the main rotor shaft for large wind turbines. Recently, there are ultra-large bearings with bore diameters of over 2 m, and enlargement of bearing size is proceeding.

In addition, the bearing type is changing.

Conventionally, it was typical to use spherical roller bearings, but tapered roller bearings or cylindrical roller bearings have been increasingly adopted. As a countermeasure to prevent the weight from increasing with expanding size, various types of bearings and bearing combinations have been examined. For instance, the steeply-sloped double-row tapered roller bearing (Figure 3 (c)) can support high moment loads by one bearing and allows for shortening of the length of the main rotor shaft. Another example is the bearing combination of a double-row tapered roller bearing and a cylindrical roller bearing (Figure 3 (d)), which maintain proper distance and allow for compacting the size of the main rotor shaft.

3.2 Bearings for gearboxes

Gearboxes are components of wind turbines more than 10 bearings are generally used there. This is because having a high speed-up ratio requires many gears, resulting in many bearings being necessary to support the many gear shafts.

Generally, a 2 MW class main rotor shaft rotates at around 15 rpm, and the rotational speed of a four-pole generator is between 1 500 and 1 800 rpm; therefore, the gear ratio is over 100:1. The rotational speed of the main rotor shaft decreases with increasing generator size (increasing blade length) due to speed limitations of the blade tips, resulting in a low speed of less than 10 rpm for wind turbines with capacities over 5 MW. In this case, the gear ratio is more than 150:1. To avoid such high speed-increasing ratio for high reliability of gearboxes, a medium-speed gear type, which adopts a lower speed-up (approximately 50:1), has been developed for use in multipole generators (up to 12 poles), instead of a four-pole generator.

As shown in Figure 3, gearboxes with 1 planetary gear and 2 helical gears are used for 2 MW generators or smaller. 2 planetary gears and 1 helical gear are also adopted in cases of a high gear ratio. The use of 2 planetary gears to allow for medium speed operation is also sometimes adopted.

Input torque and the load on bearings increases with expanding size of wind turbine. Carrier bearings and planetary gear bearings are used in the planetary gears. Since the size of drive shaft increases with increasing torque, carrier bearings become large and the bearing load capacity also increases. But the load capacity of bearings that are used for the planetary gears that need to remain compact is very limited. Therefore, increasing load capacity can be achieved by removing the bearing outer ring, making the bore surface of a planetary gear serve as the outer ring raceway surface and enlarging the roller diameter.

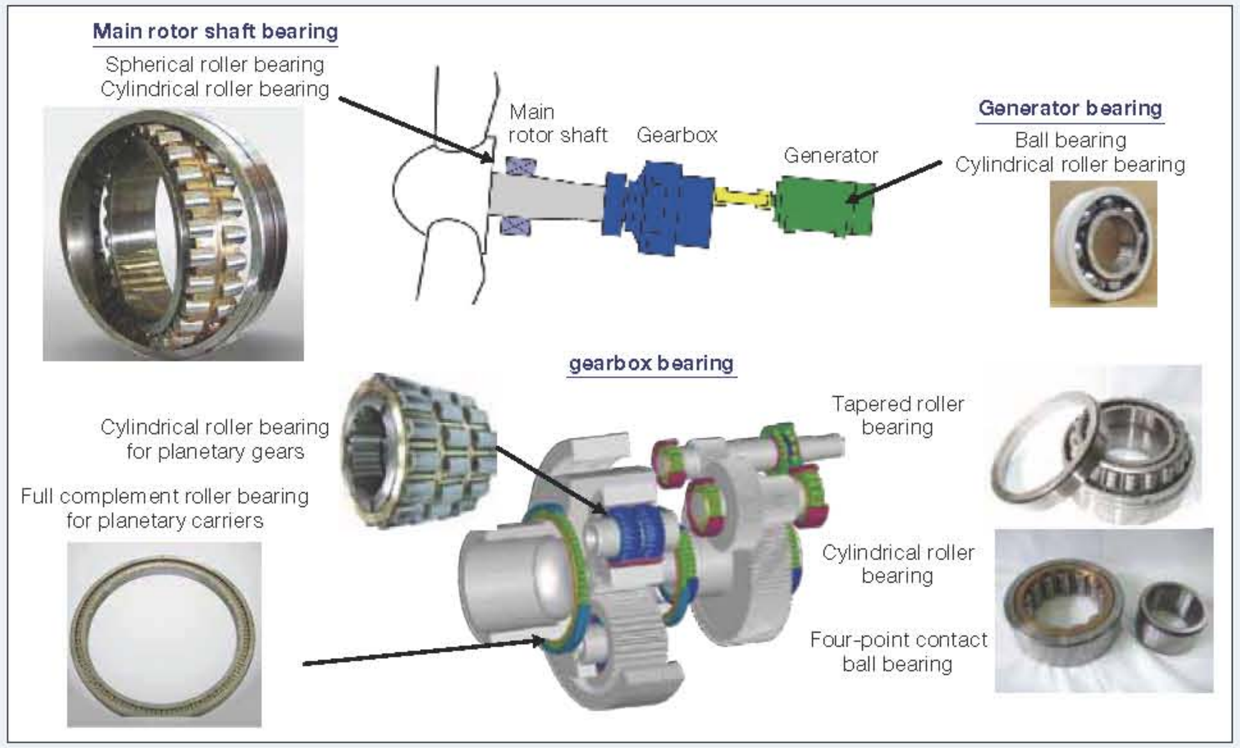

Fig. 2 Bearings used for various components of wind turbines

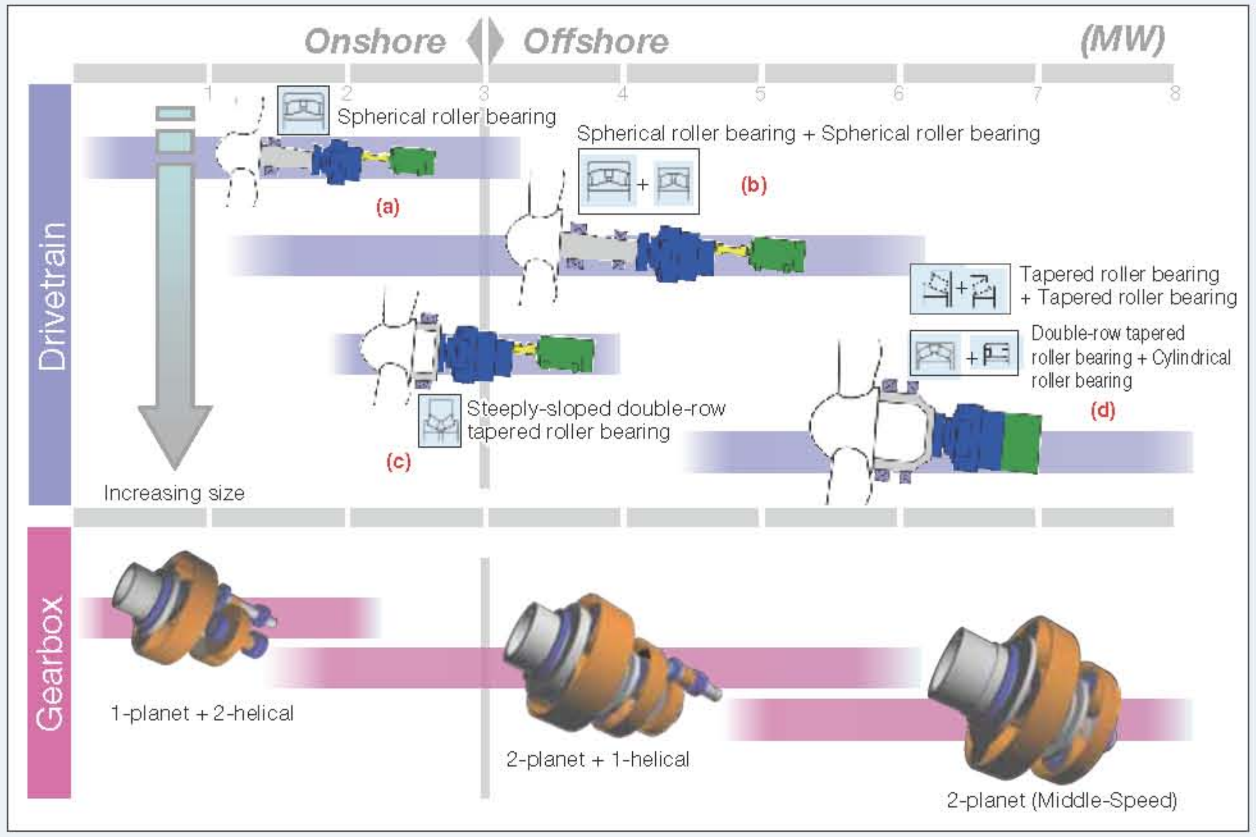

Fig. 3 Transition of drivetrain and gearbox with increasing wind turbine size

1) Introduction of NSK product – Cylindrical roller bearings with high load capacity

NSK developed a cylindrical roller bearing with high load capacity for responding to these market needs. As shown in Figure 4, increasing the number of rollers in a bearing can reduce the pressure at the surface-contact area of the roller and ring, increase the load capacity, and lengthen the bearing life. On the other hand, increasing the number of rollers reduces the thickness of the cage bar and reduces cage strength. Therefore, stress concentration on the cage bar was controlled by optimizing the cage shape, and a cage with sufficient strength was developed.

2) Introduction of NSK product – Large-sized bearings using long-life bearing material

Additionally, bearings for gearboxes use lubrication oil together with the gears and are exposed to severe conditions. Common problems include contamination powder from gear wear and the generation of insufficient lubrication oil due to increased viscosity at a low-temperature start. Therefore, it is possible to select STF (Super-TF) material or HTF (High-TF) material that has a longer life than that of general bearing steel under contaminated conditions, developed by NSK for such severe applications. Although the lubrication oil in gearboxes has recently been controlled by filtering, the life of STF and HTF material is 1.5 to 2 times longer than that of general bearing steel, even in such a case[2]. NSK's focus in developing these materials has been to increase the bearing life in this way.

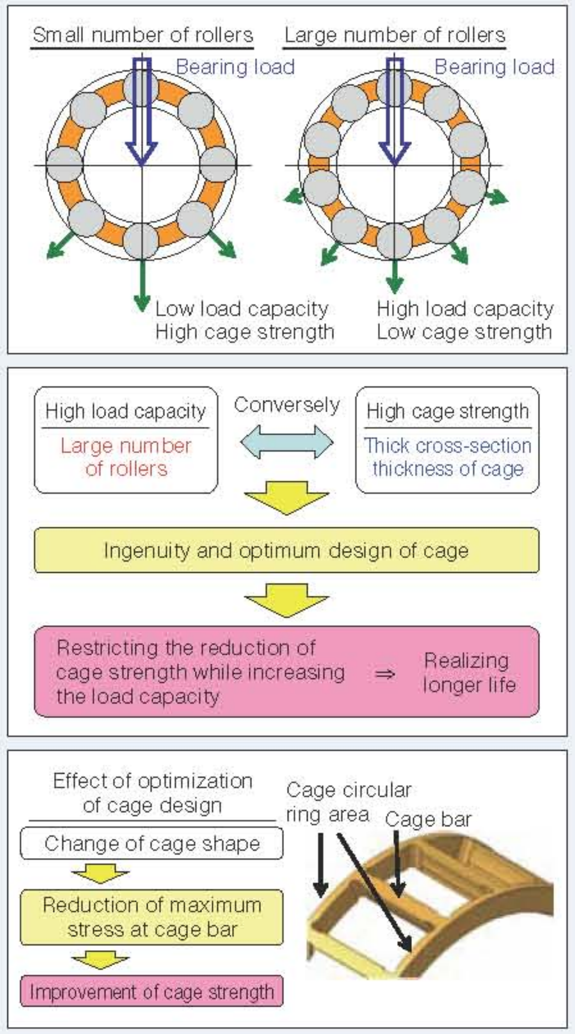

Fig. 4 Cylindrical roller bearing with high load capacity

3.3 Bearings for generators

To restrict the increase of the main rotor shaft speed-up ratio with increasing size, like the aforementioned medium-speed type or multi-pole configurations, generation control in the variable speed area of a generator has been conducted. Electric erosion (microscopic melting due to the passage of current) on the raceway surface of generator bearings has sometimes occurred in recent years, although it is not known if this is related to these new measures. As a countermeasure, bearings with increased insulating performance from ceramic spraying on the bearing outside surface have been used.

4. Condition Monitoring System of Wind Turbine Bearings

As it is not easy to access wind turbines on the ocean, the installation of condition monitoring systems has been recently mandated, and condition monitoring systems for wind turbines have been introduced from various diagnostic device manufacturers. Bearing manufacturers have diagnostic knowledge of abnormal bearing conditions and have the technology to detect such abnormalities at an early stage[3]. By using such diagnostics in components such as the drivetrain and structures of wind turbines in the future, it will be possible to make a diagnostic device for facilitating early detection of abnormalities within the entire wind turbine. NSK is participating in the NEDO project this year to approach this goal.

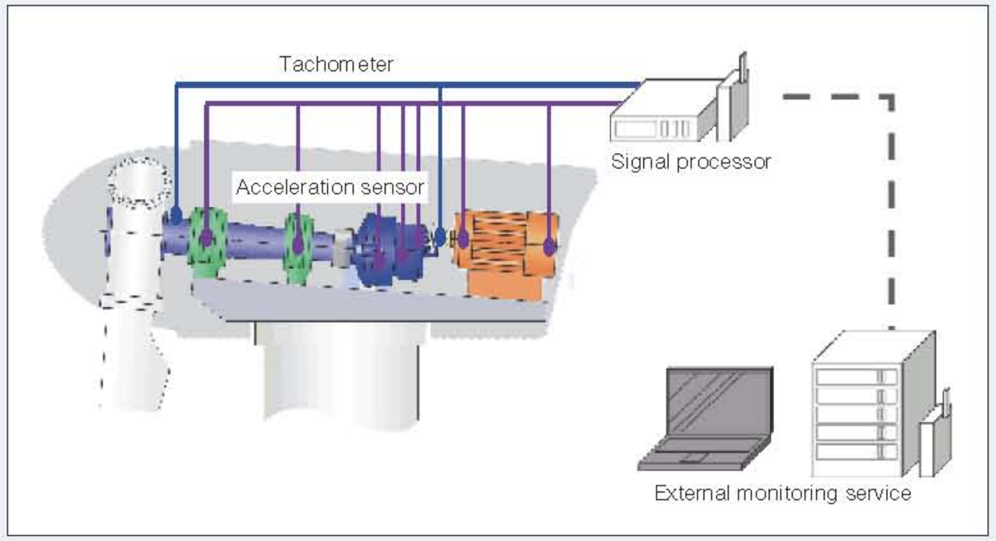

Fig. 5 Condition monitoring system of wind turbine bearings

5. Conclusion

By using the current experience and comprehensive capabilities as a bearing manufacturer, NSK contributes to advancing the wind turbine industry. NSK provides highly reliable products in response to various demands regarding increasing size in wind turbine bearings.

References

1) BTM Wind Report: World Market Update 2012, "Wind turbine size class by market share 2010–2012."
2) NSK Technical Journal No. 652 "Long Life Super TF & Hi-TF Bearings under Severe Lubrication Conditions."
3) NSK Technical Journal No. 674 "Bearing Noise Digital Analysis System ACOUS NAVI.

Tasuku Suzuki

Masafumi Fukunaga

Technological Trends of Bearings for Industrial Compressors

Keisuke Kimura
Industrial Machinery Bearing Technology Center

ABSTRACT

A compressor, as its name implies, presses a gaseous body and creates high pressure. Compressors are used in a wide variety of applications, such as factory and construction site equipment, drive sources, heating, ventilation, and air conditioning. In this article, we will discuss bearing technology and compressor bearings, as well as examine compressor trends and demands.

1. Introduction

Compressors are used for a wide variety of applications where increasing pressure is achieved by compressing gas.

Here, the authors will discuss the technology and products used for supporting the rotation of bearings (compressor bearings) in the compression sections of a compressor with consideration for current demand and trends.

2. Application and Demand for Compressors

Compressors are broadly separated into two types: compressors for compressing general air (gas) and refrigeration and air conditioning compressors for compressing refrigerant gas.

Compressors for compressing air (gas) are used in a wide variety of applications (Figure 1) and some examples are introduced below:

(1) Device controllers, cooling and processing in manufacturing or in the production of electricity, electronic products, and automobiles
(2) Treatment, brewage, cultivation, and aeration in the production of food, chemical products, and medicinal drugs
(3) Pressurized air, cooling, and burning in civil engineering, cement production, and glass production (ceramics)

In recent years, compressors have additionally been used in areas such as petro chemistry for the pneumatic transporting of processed gas, including high-visibility natural gas (LNG, shale gas).

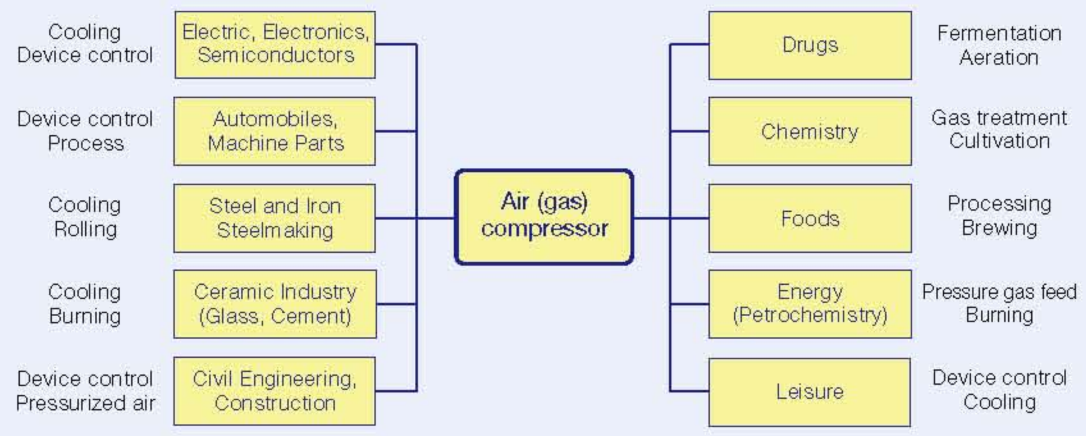

Fig. 1 Air and gas compressor applications

On the other hand, compressors for refrigeration and air conditioning are used for compressing refrigerant gas utilized for heat exchange in refrigeration cycles. These include air conditioning compressors for home comfort and industry applications as well as refrigeration and cold storage compressors used to preserve the quality of food, drugs, and other medical supplies (Figure 2).

All industries and societies are anticipated to have increased demand for both kinds of compressors in the future, especially in emerging countries where population growth and infrastructure investment are expected.

Based on statistical data regarding recent orders of compressors in Japan from the Japan Society of Industrial Machinery Manufacturers[1)], Japanese demand increased by 20 % a year and foreign demand increased by 30 % a year until 2006. However, demand decreased sharply in 2009 due to the influence of the Global Financial Crisis and the bankruptcy of Lehman Brothers in 2007 and 2008 (Figure 3).

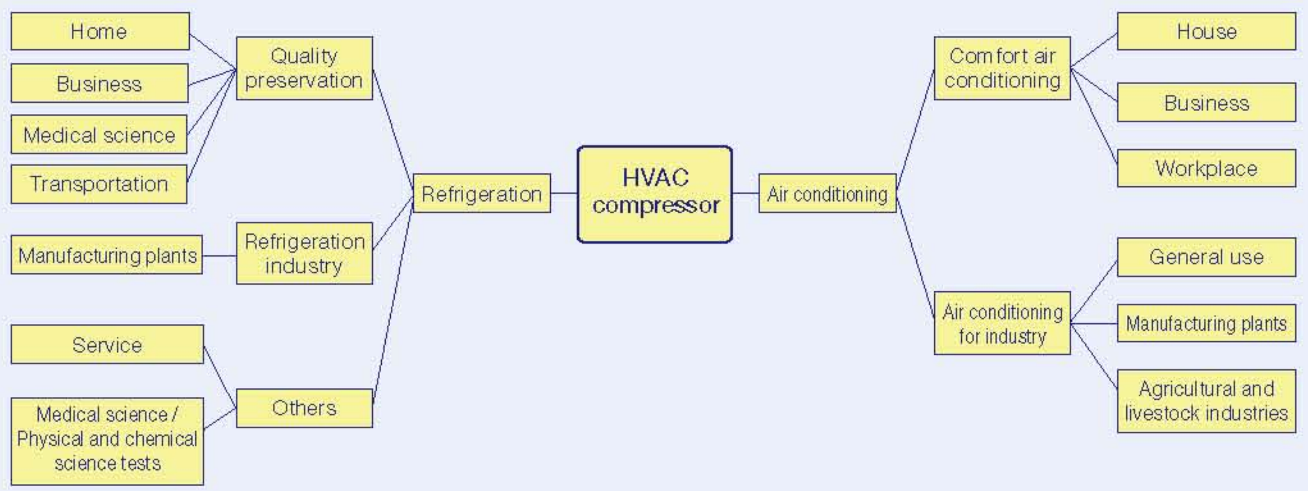

Fig. 2 HVAC compressor applications

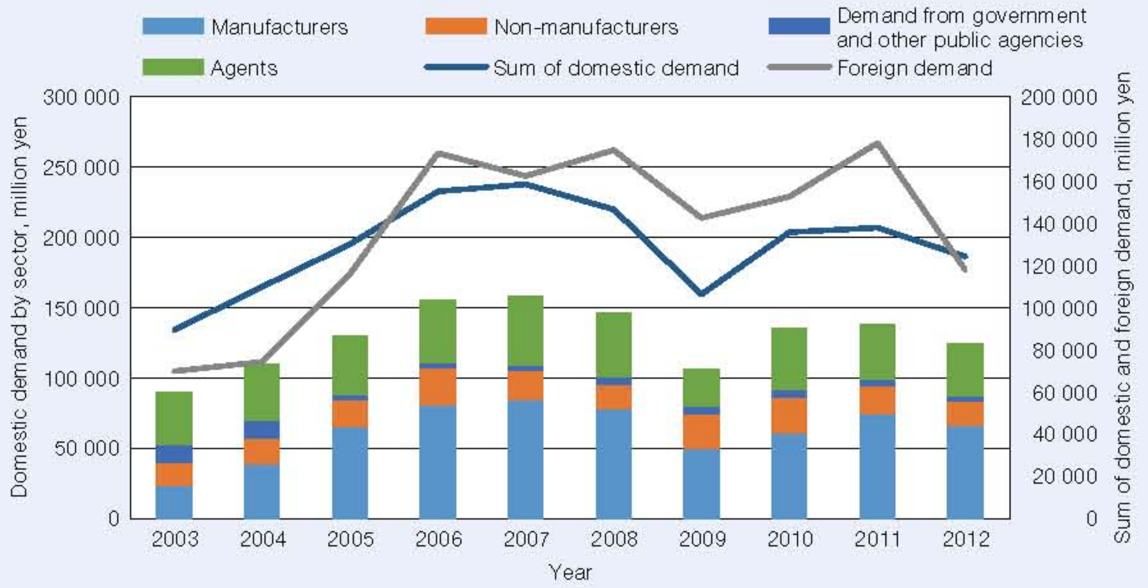

Fig. 3 Domestic demand for compressors

Although demand showed a slow recovery trend after 2010, demand fell again in 2012, especially in foreign countries, due to Europe's debt crisis, the stagnation of China's economic growth, and global downturn following financial problems in the USA. However, demand tended to increase in the long-term for these ten years and further increases in demand from emerging countries are expected in the future.

3. Bearings Used in Compressors

Compressors are classified broadly into volume types and turbo types by their compression principle[2].

In a volume-type compressor, plain bearings and rolling bearings are used in the main shaft. Due to space constraints and cost, usually plain bearings are adopted for compact and low-cost compressors. On the other hand, rolling bearings are utilized in medium and large compressors, such as refrigerating machines or air compressors used in facilities and plants, where high speed, high accuracy, high rigidity, and reliability are required. These medium and large size volume-type compressors are being adopted and used widely in reciprocating and screw compressors, and rolling bearings are increasingly adopted in scroll compressors as well.

In turbo-type compressors, high-cost hydrostatic bearings have generally been used because it is necessary to rotate the vanes at a very high speed for compression. However, because the performance of rolling bearings has increased in recent years, adoption of rolling bearings in turbo compressors has increased in order to improve reliability and reduce cost.

4. Rolling Bearings for Compressors

Bearing technologies for reciprocating compressors, scroll compressors, and screw compressors that use rolling bearings are introduced here using NSK's products as examples. Bearings for turbo-type compressors are omitted from this paper on account of space.

4.1 Bearings for reciprocating compressors

Sizes of reciprocating compressors vary from small to large, and the compressors are used in a wide range of applications. Rotating the crankshaft results in compression by pushing up a piston connected by a rod through a reciprocating crank.

The following bearings are used for these rotation and oscillating mechanisms (Figure 4):

(1) A bearing that supports crankshaft receives a load generated when air is compressed through the rod and crank. A number of cylinders are used depending on the compressor type. A cylindrical roller bearing with high load capacity or an easy-to-handle deep groove ball bearing is used to support the load.

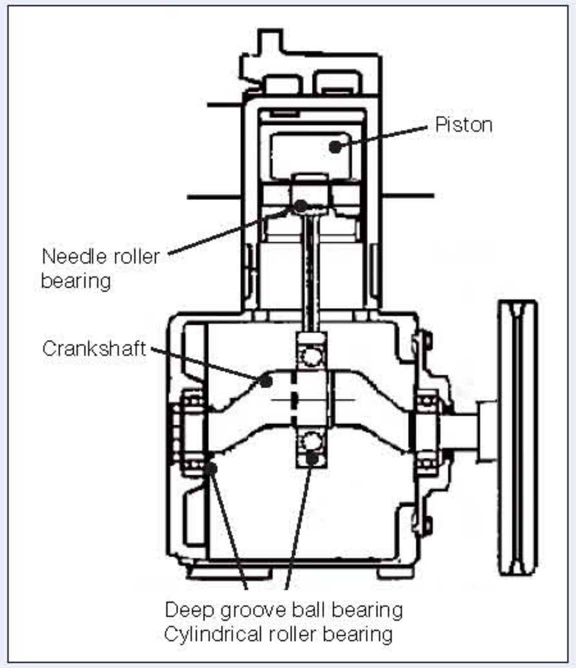

Fig. 4 Reciprocating compressor

(2) A bearing placed between the crank and the rod that pushes up a piston has a necessarily large bore because the crank passes through the crankshaft during assembly of the compressor. Because the crankshaft rotates with centrifugal whirling however, the bearing is expected to have a small outside diameter for suppressing imbalance. As a result, thin-walled cylindrical roller bearings with a small outside diameter and a large bore diameter are utilized.

(3) A bearing used for the joint of the rod tip and piston is required to be small because it is placed at the tip of the rod without any rotation but with oscillation. However, the bearing receives a high load from the piston. Therefore, a needle roller bearing is generally used.

Bearings used for air compression in reciprocating compressors are mostly dry and oil-free; therefore, grease is generally used for lubrication of the bearings.

Bearings with grease lubrication sometimes experience failures, such as seizure caused by grease leakage under severe conditions, because they are exposed to high temperature by the heat from compression. In addition, premature flaking bearing damage has occurred in some compressors in recent years, and white structure flaking was observed in a detailed investigation (Photo 1).

It is well known that white structure flaking sometimes occurs in bearings for automotive electric accessories, which are driven by a belt and pulley, as well as reciprocating compressors used under high temperature conditions with grease lubrication. As a countermeasure, it is effective to adopt the HAB grease developed by NSK[3] (Figure 5).

HAB grease enables formation of a rigid grease film, prevents static electric charges by blending conductive nano-carbon particles in the grease, and has excellent resistance to white structure flaking. Additionally, adopting a thickener that has good stability properties at high temperatures allows for excellent durability under high temperature conditions. These features can prevent the premature damage of reciprocating compressor bearings and contribute to lengthening the compressor's service life.

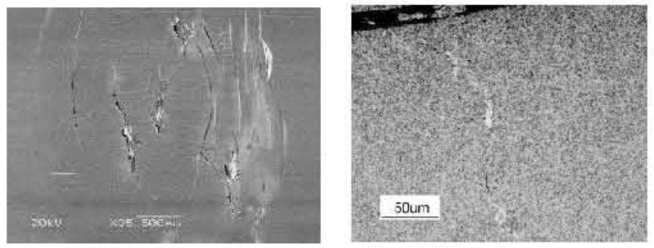

(a) Damaged area (b) Sectional structure

Photo 1 White structure flaking

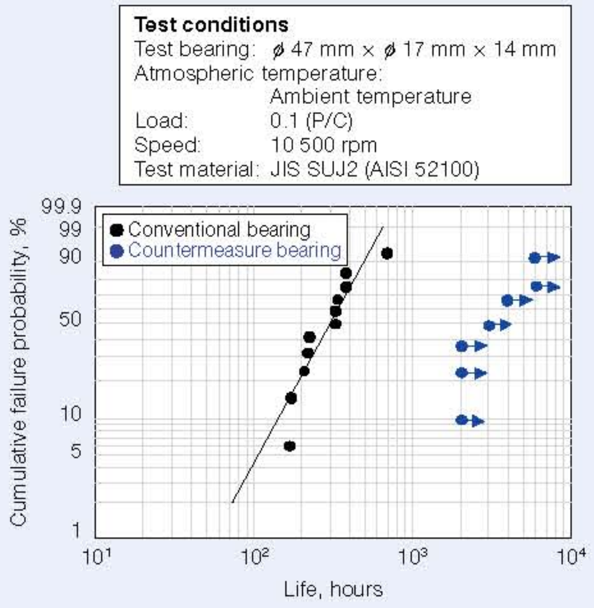
Test conditions
Test bearing: ϕ 47 mm × ϕ 17 mm × 14 mm
Atmospheric temperature: Ambient temperature
Load: 0.1 (P/C)
Speed: 10 500 rpm
Test material: JIS SUJ2 (AISI 52100)

Fig. 5 White structure flaking, durability test of HAB grease

4.2 Bearings for scroll compressors

A scroll compressor consists of a fixed scroll that is orbited by a scroll blade. Air is compressed by reducing the space (compression chamber) volume between the scroll blade and the fixed scroll[2] (Figure 6 and Figure 7). The scroll compressor does not repeat suction and exhaust at each compression because of the compression method. Furthermore, it has low noise and low vibration compared with a reciprocating compressor or rotary compressor, and is mostly used in air conditioner compressors that make a comfortable living environment.

The bearings used in these scroll compressors are described below:

(1) A plain bearing is adopted as a thrust bearing that is positioned just under the Turing scroll and directly receives the high load from the compression chamber due to the narrow space.

(2) A cylindrical roller bearing with high radial load capacity is used just under the thrust bearing to receive the radial load with the turning of the Turing scroll.

(3) A deep groove ball bearing is adopted for the shaft end that holds the motor (rotor).

In small-sized compressor for household air conditioners, plain bearings are usually used because of their low cost. However, rolling bearings have been increasingly examined in recent years due to their high efficiency and high reliability.

In scroll compressors for refrigeration and air conditioning, refrigerant oil is also used as the lubricating oil for the bearings. Due to its chemical makeup, this refrigerant often becomes a very low viscosity. This low-viscosity lubricating environment sometimes causes failures such as wear or seizure on the raceway surfaces or rolling contact surfaces of rolling bearings. When operational conditions are especially severe, microscopic flaking (peeling damage) sometimes occurs.

NSK's unique material technology[4] has led to a countermeasure material that exerts an effect on this microscopic flaking. With this material, retained austenite is increased and fine carbide and nitride are contained. A rotational test of this countermeasure bearing was carried out under a lubricating environment of refrigerant oil mixed with refrigerant, and results showed that a longer life could be obtained (Figure 8 and Photo 2).

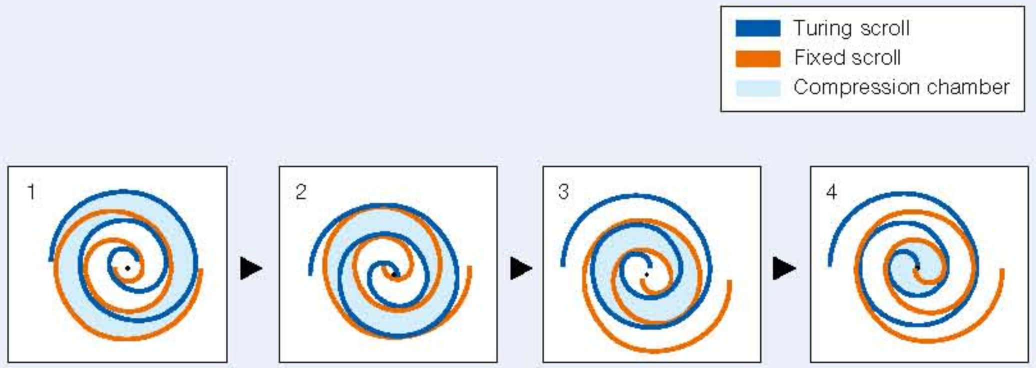

Fig. 6 Compression process of a scroll compressor[2)]

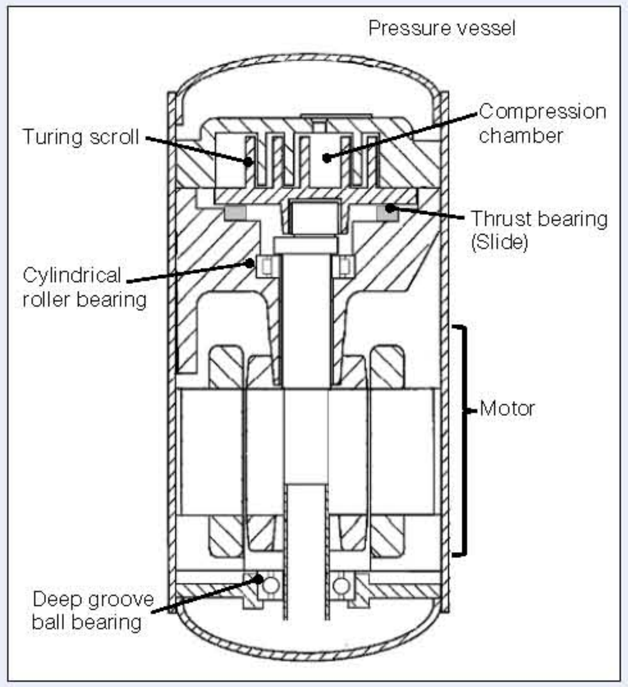

Fig. 7 Scroll compressor

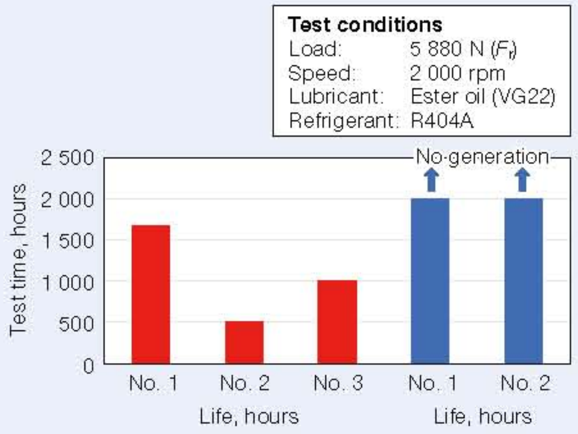

Fig. 8 Refrigerant environment test results

Photo 2 Peeling failure after refrigerant environment testing

4.3 Bearings for screw compressors

The basic structure of screw compressors used in refrigeration and air conditioner applications and air compression applications, is the same in both. The standard twin-screw type used for air compression compresses gas by engaging a paired male rotor and female rotor and rotating the pair in reverse directions to each other.

There is a radial load and thrust load on both of the rotors. On the fixed side, matched angular contact ball bearings are used because it is necessary for the rotor-supporting bearing to support the rotation while maintaining accurate clearance between the rotors or rotor and housing. On the other hand, a cylindrical roller bearing is usually used on the free side for releasing the thermal expansion of the shaft caused by heat generation in the compression process (Figure 9). Compressors with especially high radial load sometimes adopt a cylindrical roller bearing on the fixed side and use matched angular contact ball bearings together.

In an air compressor, a large quantity of oil is injected into the compression chamber to lubricate the contact area of the two rotors, cool the area, and seal the clearance. This oil in the compression chamber is also utilized as the lubricating oil for the bearings; therefore, the bearing cage material must be a good match with the oil. The oil includes an extreme-pressure additive, which makes it a bad match with the nylon resin generally used as cage material. Problems with ill-matched bearing cage materials can happen, especially at high temperatures. To combat these problems in such compressor bearings, NSK uses a uniquely developed material, L-PPS (linear chain polyphenylene sulfide) resin, as the cage material. NSK's L-PPS resin material is superior in wear resistance and suitable for bearings in a wide range of applications other than compressors.

On the other hand, dry, oil-free compressors that do not include oil in the compressed air are used in the medical drug, food, and semiconductor markets, and future extension is predicted in these fields. This kind of compressor does not have any seal such as oil between the two rotors and has a large leak ratio of the compressing gas. Therefore, substantial compression efficiency is ensured by high-speed rotation of up to approximately 8 000 rpm. The bearing arrangement of this compressor is basically the same as that of the oil-injection type, but bearings with different internal specifications, cage material, and cage types are used due to the high rotation speed (Table 1).

Although a machined-brass cage is often used in the compressor bearing of a dry oil-free compressor, this is very expensive due to lathe turning of such high-priced material, and this sometimes causes problems. In such a case, an "L-PPS cage bearing for oil-free compressors" (Photo 3) with high-speed and low heat generation is examined for adoption. This product uses the NSK-developed, superior wear resistance L-PPS resin as a cage material. Table 2 shows the main characteristics.

Because this bearing cage is made of L-PPS resin, the material strength is reduced compared with a conventional machined-brass cage but the centrifugal force is reduced during high-speed rotation. By analyzing the stress

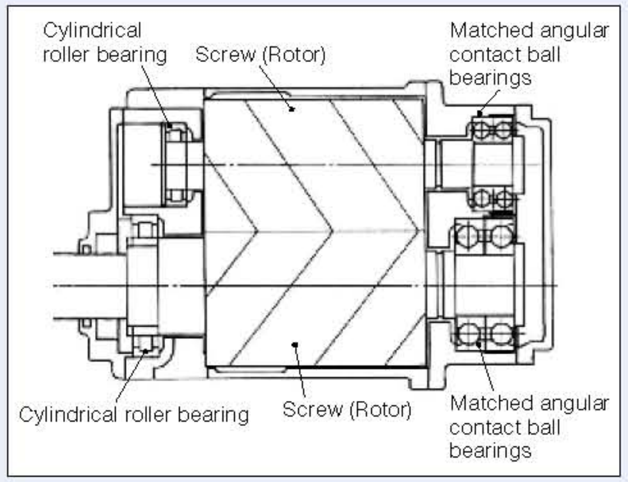

Fig. 9 Screw compressor

Table 1 Characteristics of bearings for oil-injection and oil-free compressors

		Oil-injection type	Oil-free type	Features
Internal specification (contact angle)		Large size	Small size	Restrains heat generation from high-speed operation
Bearing accuracy		Standard accuracy	High accuracy	Stable rotation, vibration
Cage specification	Material	Non-ferrous alloy / resin	Copper alloy	Ensures reliability
	Type	Rolling element guided	Bearing ring guided	Stable rotation, vibration

acting on the cage pocket, the cage has a design and shape that ensure the necessary strength. Additionally, this bearing has lower heat generation, lower torque, and lower vibration (Figure 10 and Figure 11) due to the characteristics of L-PPS, such as high wear resistance and capability for injection molding.

The “L-PPS cage bearing for oil-free compressors” will contribute to increasing the performance of dry oil-free compressors in the future.

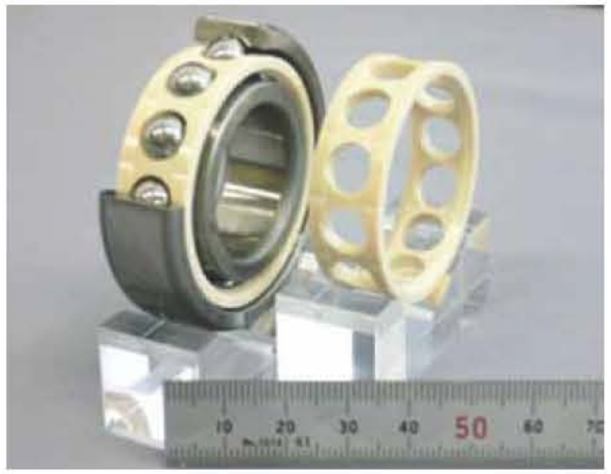

Photo 3 L-PPS cage bearing for oil-free compressors

Table 2 Characteristics of L-PPS cages for oil-free compressor bearings

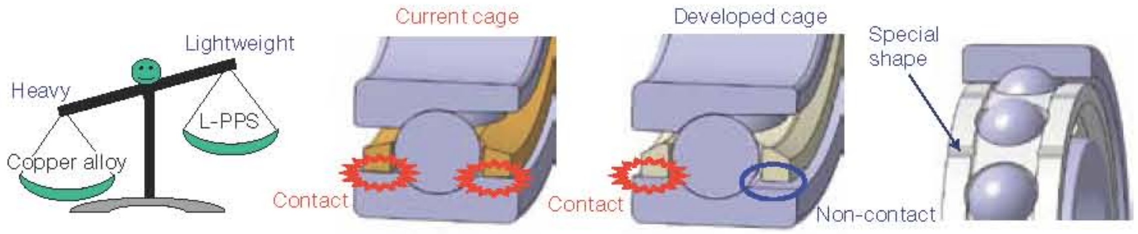

	Current cage	Current cage	Features
Processing method	Cutting	Molding	Improved mass production
Material	Copper alloy	L-PPS	Unique development by NSK (high accuracy) ⇒ Low vibration, wear resistance
Specific gravity (mass)	8.25	1.6	Lightweight ⇒ Low torque, low vibration
Riding surface	Both sides	One side	Low friction ⇒ Low torque
Outer shape	Standard	Special	Improved lubrication ⇒ Low vibration

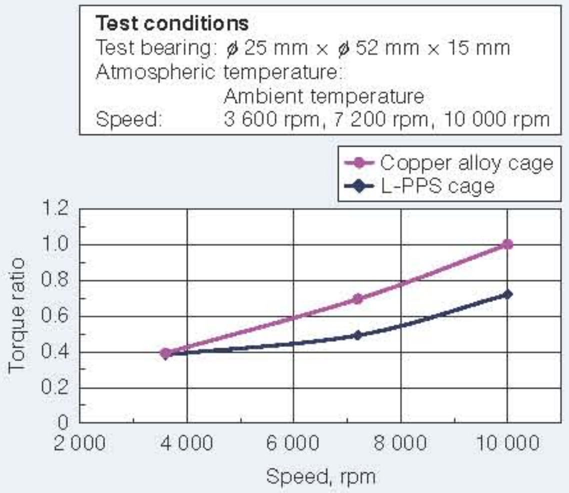

Fig. 10 Torque measurement results

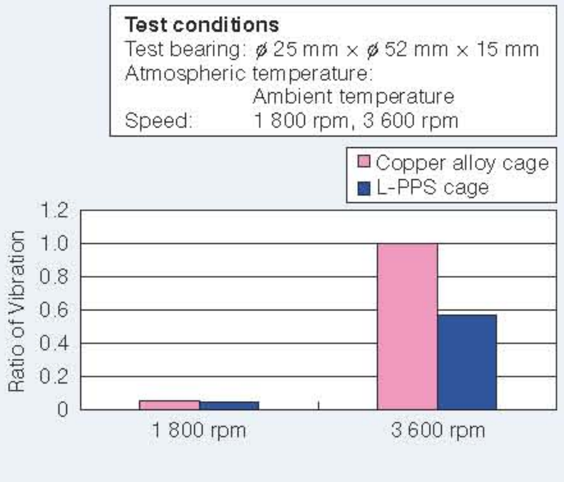

Fig. 11 Vibration test results

5. Conclusion

Along with the demand for and trends of compressors, we discussed the bearings used in reciprocating compressors, scroll compressors, and screw compressors.

Compressors are indispensable in our daily life as the power source of much infrastructure and are used by a wide variety of industries and production facilities. NSK contributes to society now and in the future by continuously developing and designing the bearings used in these compressors.

References

1) Statistics, “Order situation of compressors per demand sector,” Industrial Machinery, 756 (2013. 9) 63.
2) S. Higashi, “Bearing Technology for Industrial Compressors,” NSK Technical Journal, 683 (2009) 12–17.
3) K. Iso, “HAB Grease Countering White Structure Flaking,” NSK Technical Journal, 679 (2005) 28–35.
4) NSK catalog, “Super-TF Bearings and HI-TF Bearings,” CAT. No. 399, 3–4.

Keisuke Kimura

Development of the TOUGHCARRIER for Automotive Manufacturing Equipment

Hiroki Yamaguchi
Linear Technology Center

ABSTRACT

NSK has developed the TOUGHCARRIER—a new single-axis actuator that is the first in the industry to offer considerably higher load capacity by using rollers as rolling elements in the linear guide component while maintaining the same cross-sectional profile as conventional single-axis actuators. The TOUGHCARRIER is suitable for automotive manufacturing equipment that generally requires high-load capacity and compact-sized components.

In this article, we describe the structure, features, and relationship between load and deformation/service life of the TOUGHCARRIER.

1. Introduction

In 1991, NSK was the first in the world to combine a ball screw, linear guide, and base in a product developed and commercialized as the MONOCARRIER1).Since then, the MONOCARRIER has contributed to the electric operation, automation, and compactness of manufacturing machinery in various industries.

Recently, mixed production of many automobile body types in the same production line (flexible line) to flexibly respond to fluctuations in demand has been increasing. For quality improvement or environmental measures, adoption of a linear motion unit, such as a MONOCARRIER, that matches the electric operation of a piece of equipment or tool has been increasing. Because the conventional linear motion unit uses balls as the rolling element for the guide component, load-bearing performance is sometimes insufficient as linear motion units for automobile manufacturing facilities mostly receive high moment loads generated by the position of high load or load away from the guide element when processed or welded. Therefore, compact linear motion units that are usable with ease are required to operate even under severe conditions.

To respond to these requirements, NSK developed the linear motion unit “TOUGHCARRIER2)” (Photo 1), which increases load-bearing performance greatly by adopting rollers as the rolling element for the guide component while maintaining the same cross-sectional dimensions as a conventional linear motion unit.

Here, we will introduce the structure and features of this compact and integrated linear motion unit. The “TOUGHCARRIER,” with its ultra-high load capacity, is most suitable for general industrial machinery, especially automobile manufacturing facilities, and when element deformation and high load act to influence life.

Photo 1 TOUGHCARRIER2)

2. Structure and Features

2.1 Compact structure

The TOUGHCARRIER is a linear motion unit with an integrated feed system and guide system like the conventional MONOCARRIER. The units share many of the following structures and features.

The MONOCARRIER3) (Photo 2) has an all-in-one structure that integrates each part of a single-axis table unit4) (Photo 3), conventionally consisting of a ball screw, linear guide, the base itself, and support bearings. Therefore, the MONOCARRIER is more lightweight and compact than a conventional single-axis table unit due to the all-in-one structure. Additionally, the workload for design, assembly, and adjustment of alignment accuracy is reduced, and the replacement of each unit is easy because all the linear motion elements are unitized.

Figure 1 shows the structure of a MONOCARRIER. The slider has both functions of screw shaft recirculation and linear guide recirculation and therefore moves smoothly along the rail in the longitudinal direction by rotating the screw shaft by motor.

NSK provides the MCM series for those seeking light weight and compactness and the MCH series where the rigidity of beam is increased to make it possible to use the rail as a structural member. Additionally, NSK provides multiple model numbers with the different cross-sectional dimensions in each series.

On the other hand, the TOUGHCARRIER uses rollers as the rolling element for the guide component of the integrated linear motion unit to respond to inquiries and requests from users, including conventional requests for light weight, compactness, ease of replacement, and reduction of design and assembly work. Size was reduced with higher load capacity thanks to the increased load capacity of the guide element compared with the conventional MONOCARRIER. Figure 2 shows the cross-section of the guide element for the conventional MONOCARRIER, and Figure 3 shows the cross-section of the guide element for a TOUGHCARRIER.

Photo 2 MONOCARRIER3)

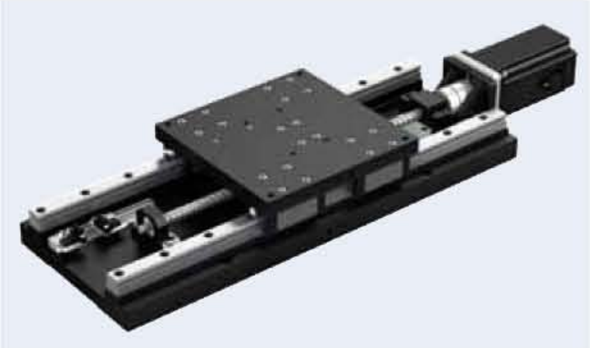

Photo 3 Conventional single-axis table unit4)

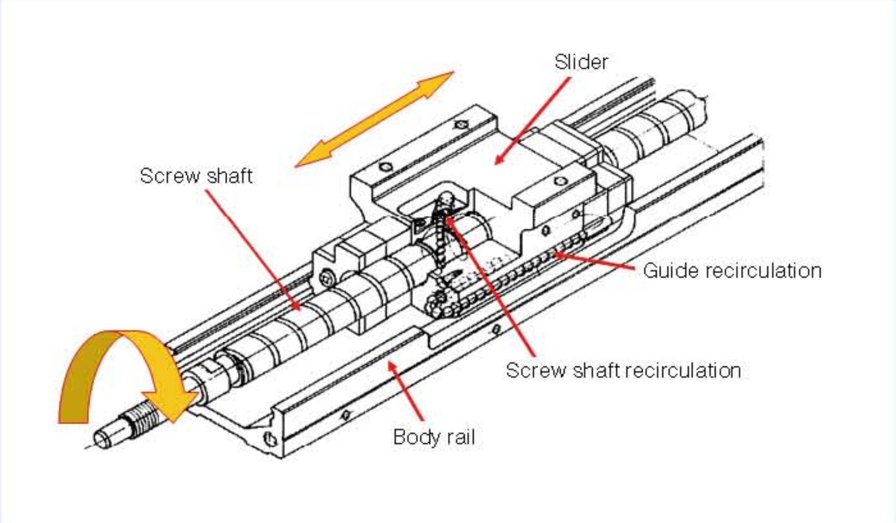

Fig. 1 Structure of a MONOCARRIER

2.2 High load capacity and long life

The TOUGHCARRIER achieves high load capacity by changing the rolling elements in the linear guide component from balls to rollers without changing the cross-sectional dimensions of the conventional MONOCARRIER. This is accomplished by forming the shape of each part with consideration of strength and element deformation under high load and locating each part at the optimum position, in addition to utilizing the already developed technology for the roller guide RA series that has been commercialized by NSK.

Comparisons of the MONOCARRIER and TOUGHCARRIER can be seen in Figure 4 and Figure 5. Figure 4 shows values of dynamic load rating that define the length of life, and Figure 5 shows values of static load rating that define the permissible maximum load of production facilities that incorporate a linear motion unit. The vertical axis shows the load capacity calculated by ISO standards, and the horizontal axis shows model numbers with different cross-sectional dimensions. The TOUGHCARRIER has a dynamic load rating of more than 2 times higher than that of the MONOCARRIER, which translates to a more than 10 times longer life, and has an approximately 3 times higher static load rating—a level that puts the TOUGHCARRIER at the top of the world in ultra-high load capacity. Because the TOUGHCARRIER has sufficient load capacity, the size can be reduced.

Here, an example of durability test results under high load conditions is shown. Assuming the usage in an actual machine, a durability test was carried out under high yawing moment load (Figure 6).

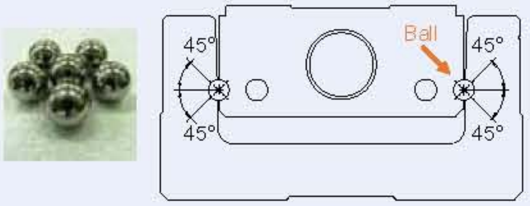

Fig. 2 Cross-sectional shape of the linear guide element of a MONOCARRIER

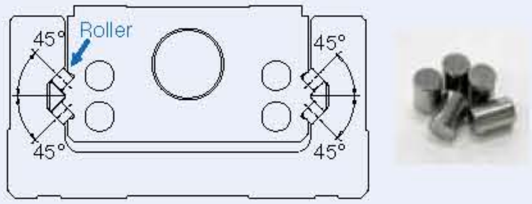

Fig. 3 Cross-sectional shape of the linear guide element of a TOUGHCARRIER

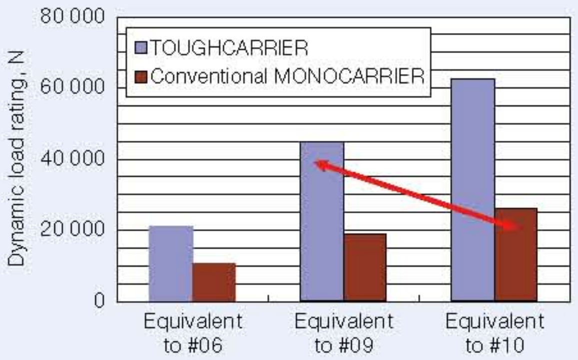

Fig. 4 Comparison of dynamic load rating

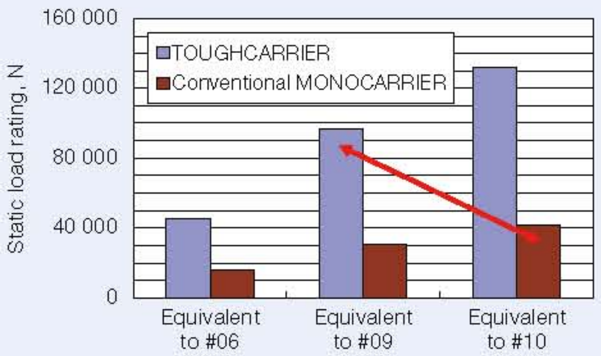

Fig. 5 Comparison of static load rating

Figure 7 shows the appearance of each raceway surface after running for the calculated life (*L* hours). The running traces generated were the same level as those of the conventional roller guide RA series. Flaking or partial wear did not occur, and it was possible to run without any problem after the test. During this durability test, the TOUGHCARRIER did not have abnormal wear on the raceway surface or other parts such as the rollers, even when drastically run over the calculated life.

The guide element of a TOUGHCARRIER is made for high load capacity in automobile production facilities. At the same time, the ball screw and support bearing elements are designed for balanced and high load capacity like the guide element because the axial load is assumed to be higher than the conventional MONOCARRIER based on predicted usage for industrial facilities, such as those with semiconductor manufacturing equipment.

Furthermore, the TOUGHCARRIER includes new specifications for increased rollers compared with the conventional roller guide RA series and standard pre-packed lubricant suitable for usage under high load conditions to achieve maximum high load capacity.

2.3 High rigidity

NSK found the optimum design of the TOUGHCARRIER by applying advanced analysis technology5) and achieved high rigidity by defining the cross-sectional shape for reducing element deformation as quickly as possible (Figure 8). Figure 9 shows example rigidity measurement results in compressive and tensile directions. The TOUGHCARRIER shows a rigidity of 5 times higher than that of the MONOCARRIER.

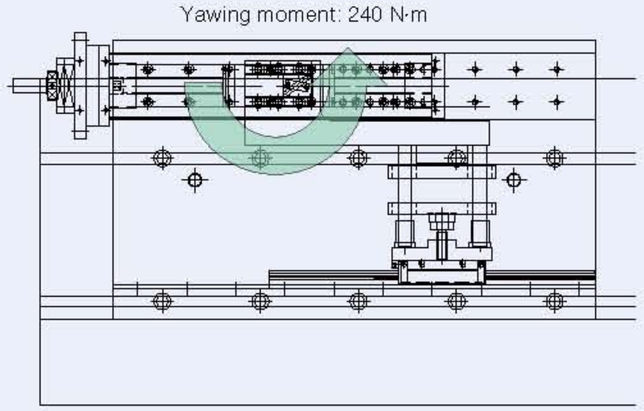

Fig. 6 Endurance test of a TOUGHCARRIER

Fig. 7 Appearance of the raceway surfaces after testing

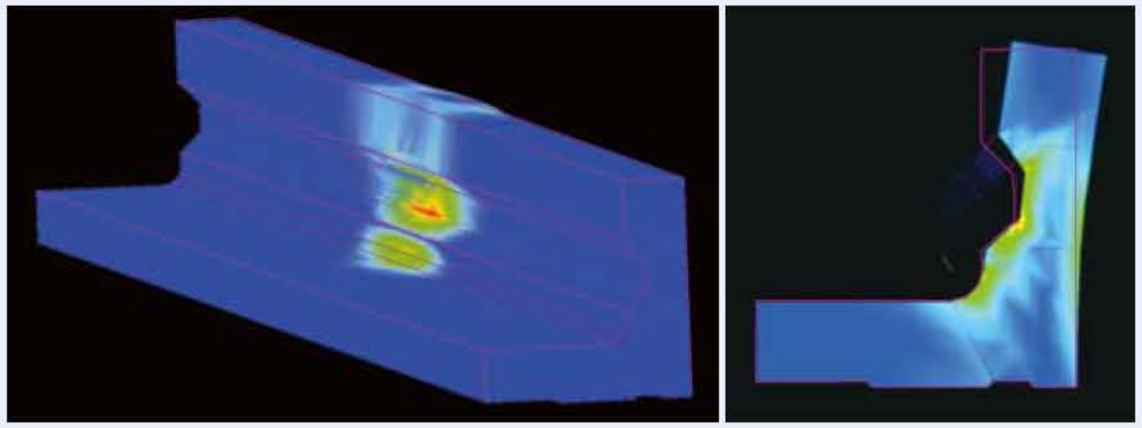

Fig. 8 Deformation analysis of a TOUGHCARRIER

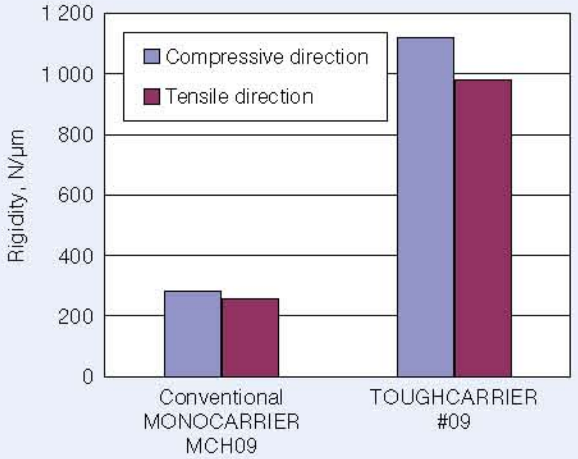

Fig. 9 Comparison of actual rigidity

2.4 Specifications against foreign matter environments

The TOUGHCARRIER is standard-equipped with the "NSK K1" lubrication unit that contributes to stable operation, even in very harsh environments with high potential for foreign matter entry, such as a spattering environment.

Figure 10[6] shows the usage results of NSK K1 in the field for a linear guide in a welding machine on an automobile production line. In the case where NSK K1 was not used, large damage occurred on the ball and raceway surfaces after 10 months of operation. In the case where NSK K1 was used, however, no damage occurred after 3 years of operation, and the conditions to enable the run were maintained. The effectiveness of NSK K1 was confirmed in a spattering environment. Because NSK K1 is a lubrication unit, long-term maintenance-free operation is possible.

Fig. 10 Example usage results of NSK K1 in the field[6]

Covered condition

Condition with the cover removed

Contamination test conditions

Fig. 11 Anti-spatter cover

Additionally, an anti-spatter cover (Figure 11) is provided as a specified item against foreign matter in such an environment. This specification includes installing covers on the upper surface and side surfaces, as well as covering the rail opening section by fireproof cloth so as to restrict the clearance generated by the standard cover. The cover prevents performance reduction by restricting the intrusion of spatter into the linear motion unit, even in a welding environment and without large increases in either cross-sectional or longitudinal dimensions. Yet, for proper function of this anti-spatter cover, it is necessary to examine the strength of the spacer blade located on the slider depending on the amount of load.

3. Load and Deformation/Service Life

3.1 Effect of element deformation under high load

Under external load, the rail of the TOUGHCARRIER deforms to open both sleeves as shown in Figure 8, the surfaces for holding rollers are not parallel, and deviation of roller load distribution occurs (Figure 12). The influence of this element deformation cannot be ignored in a usage environment where a large load is anticipated, such as in automobile production facilities. In accordance with the increase of external load, this deviation of load distribution

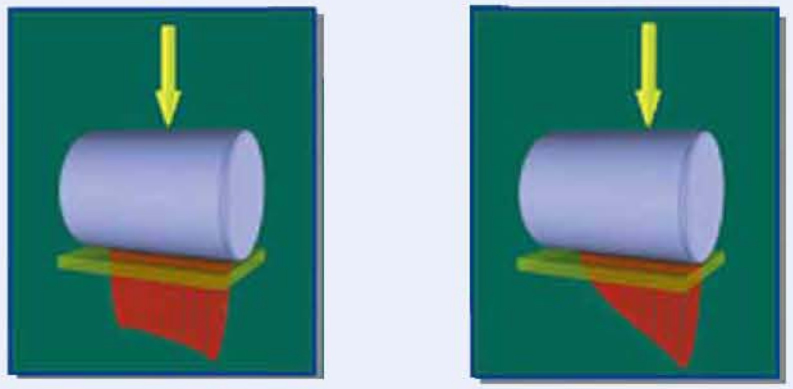

Fig. 12 Deviation of load distribution[5]

increases, in the worst case resulting in an effect on durability.

When a TOUGHCARRIER is used as the space axis where the rail bottom is not fixed, such as the upper axis of multi-axis combination, usage conditions become more severe due to the increase of element deformation of rail sleeves, even under the same load as a fixed rail bottom to the equipment mounting.

3.2 Life calculation results considering the unilateral contact of roller

Fatigue life L (km) of the roller guide can be generally calculated by the load F (N) on the slider and the load rating C (N) of the roller guide in accordance with the following simple equation:

$$L = 50 \times \left(\frac{C}{F}\right)^{\frac{10}{3}} \qquad (1)$$

C: Dynamic load rating (N), (Load when the life reaches 50 km)

In addition, the calculation is practically carried out by multiplying load F in equation (1) by load factor (f_w) as a safety factor. The load factor (f_w) should be between 1.0 and 1.5 in the absence of impact and vibration from outside the unit.

When used under high load conditions where element deformation of the rail cannot be ignored, such as when used in automobile production facilities, deviation of roller load distribution occurs and the actual life is assumed to be lower than the life calculated by equation (1). Even in such a case, NSK can simulate the actual life by using an analysis system that can grasp various properties of a TOUGHCARRIER guide element in detail. This system can handle both the analysis of elastic deformation and surface pressure distribution of the roller contact area, and element deformation analysis using FEM modeling for the slider and rail at the same time. Furthermore, the accurate distribution of contact surface pressure including partial stress concentration can be obtained by utilizing the high-speed, detailed analysis method for surface pressure[7] in the above-mentioned analysis system.

Figure 13 and Figure 14 show examples of life calculation results under high load conditions using NSK's analysis system. The horizontal axis in the figures shows the magnitude of load acting on the TOUGHCARRIER, and the vertical axis shows the life ratio calculation results obtained by the analysis system when the life calculation result obtained by equation (1) does not consider the effect of rail element deformation as "1". Additionally, Figure 13 shows the assumed results when the rail bottom is used as the space axis without being fixed, and Figure 14 shows the assumed results when the rail bottom is fixed to the equipment mounting.

Using the results of TOUGHCARRIER TCH09 as a sample, a large difference was not found between the life calculation result using equation (1) and the life calculation result obtained by the analysis system for load in the compressive direction, but the life calculation result obtained by the analysis system becomes approximately 13 % to 36 % lower than that of equation (1) when the load is in the tensile direction and the rail element deformation is not negligible. Also, in the case of an unfixed rail bottom, (Figure 13) increased rail element deformation results in a lower life ratio.

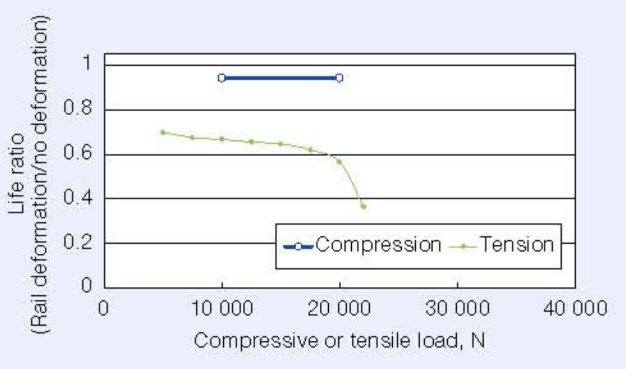

Fig. 13 Example lifetime calculation results using NSK's analysis system (rail bottom is not fixed)

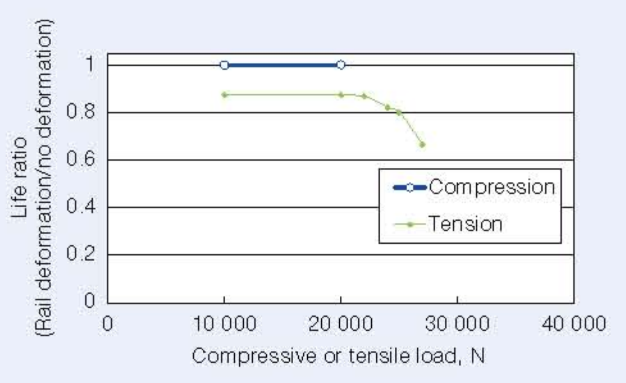

Fig. 14 Example lifetime calculation results using NSK's analysis system (rail bottom is fixed)

Additionally, the life ratio rapidly decreases when the load exceeds 20 000 N, as seen in Figure 13, and also when the load exceeds 25 000 N, as seen in Figure 14. This is because partial stress concentration occurs due to the increasing bias of excessive roller load distribution.

From these results, it is advantageous to fix the rail bottom for use because doing so mitigates rail element deformation, and the life ratio and load amount where the life ratio rapidly decreases are higher compared with the case of a rail bottom without fixing.

3.3 Example of permissible load and relaxation of element deformation

For a TOUGHCARRIER, life is simulated using the analysis system for each model number and load direction. The load factor (f_w) depends on the fixing method of the rail bottom and the permissible load that does not generate roller partial stress concentration resulting in rapid reduction of life. This is defined in Table 1 so that the life can be simply calculated using equation (1) even under high load conditions. The optimum load factor or permissible load differs in each model number and load direction, but the simulation results under the most severe conditions are made to be the representative examples to err on the side of caution.

Dynamic load acting on the guide element is generally between 5 % and 10 % of the static load rating for general industrial machinery. The permissible load of the TOUGHCARRIER exceeds this, and it can be used at ease even under high load conditions.

Additionally, static load acting on the guide element is recommended to be less than 50 % of the static load rating in order to keep a safety factor greater than "2" against the static load rating.

Furthermore, element deformation of rail sleeves can be mitigated by setting a backup such as a backboard attached on the rail bottom when used under high load conditions (Figure 15 and Figure 16). This also is advantageous for life and permissible load.

Table 1 Load factor and permissible load of the linear guide element of a TOUGHCARRIER

	Load factor	Permissible load
When rail bottom is not fixed	1.5	Less than 13% of static load rating/moment
When rail bottom is fixed	1.2	Less than 17% of static load rating/moment

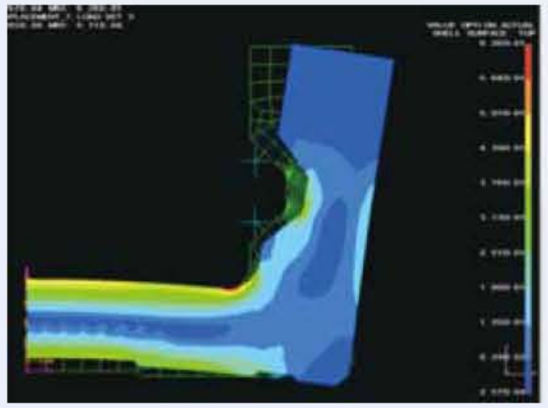

Fig. 15 Example deformation analysis (rail bottom is not fixed)

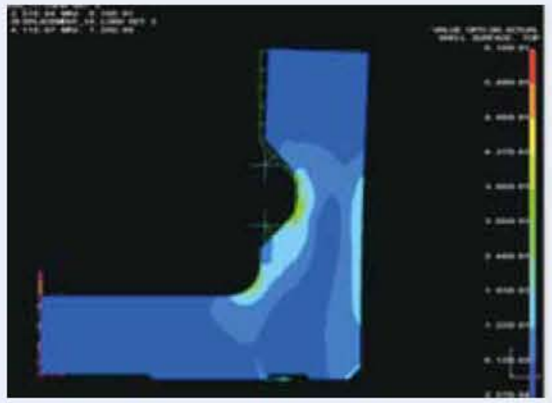

Fig. 16 Example deformation analysis (rail bottom is fixed)

4. Conclusion

In 1991, NSK was the first in the world to develop and commercialize the MONOCARRIER—a combined ball screw, linear guide, and base. Then, NSK marketed the roller guide RA series in 2004. Based on the great amount of know-how obtained by these developments, NSK has now developed a compact and tough integrated linear motion unit to match technological trends of electric operation in hydraulic transmission equipment in general industry, including the automotive industry.

NSK will continue to provide solutions suitable for each market in various industries in the future.

References

1) Y. Mizumura, S. Tsukakoshi, and H. Yamaguchi, "Features and Applications of Monocarrier as Linear Actuator," NSK TECHNICAL JOURNAL, No. 659 (1995) 20–30.
2) NSK catalog, "TOUGHCARRIER," CAT. No. 3421.
3) NSK catalog, "Monocarriers ultra-large lead, low-noise MCM Series," CAT. No. JSP-080620.
4) NSK catalog, "Precision Positioning Tables," CAT. No. 3418.
5) J. Matsumoto, "Numerical Analysis Technology on NSK Linear Guides for Machine Tools," NSK TECHNICAL JOURNAL, No. 676 (2003) 33–41.
6) NSK catalog, "Lubrication unit NSK K1," CAT. No. 3331.
7) S. Natsumeda, "Application of MLMI to Contact Problems in Rolling Bearings," NSK TECHNICAL JOURNAL, No. 668 (1999) 29–37.

Hiroki Yamaguchi

Development of a Nut Cooling Ball Screw

Junji Minakuchi, Yutaka Nagai and Kazuhito Yamamoto
NSK Ltd.

ABSTRACT

In order to suppress expansion of the ball screw shaft in machine tools with rising temperatures, forced cooling using a hollow ball screw has been widely adopted. However, to hollow out the shaft of the ball screw requires a special process and is a problem in terms of cost and lead time. To solve these problems, we developed a nut cooling ball screw. We will present an overview of this product.

Translated and reprinted from Japan Society for Precision Engineering 2011 Spring Meeting academic lecture Proceedings with permission from JSPE.

1. Introduction

Recently, traverse speed in various industrial machinery, such as NC machine tools or robots, has been rapidly increasing for the purposes of high efficiency and high productivity. Figure 1 shows the rapid traverse speed in machining center units exhibited at the Japan International Machine Tool Fair (JIMTOF) for the past 8 events. We can see the trend towards higher device speed in the figure, as the number of high-speed machines exceeding 40 m/min tended to increase over time.

Ball screws used for the traverse mechanism of these machines are designed in order to reduce frictional loss by replacing sliding contact with rolling contact, and the amount of heat generation caused by the drive torque is not so high. With the higher speeds stated above, however, heat generation is increasing, and reduction of the positioning accuracy of the screw shaft by thermal expansion is reaching a measurable level.

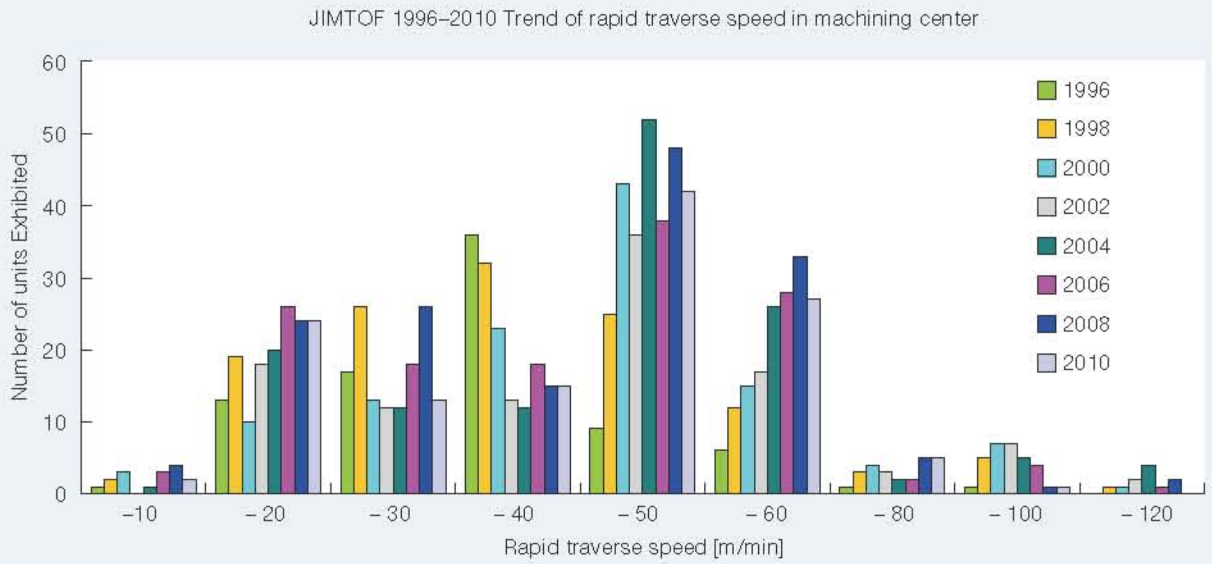

Fig. 1 Trend of increasing rapid traverse speed in machining centers

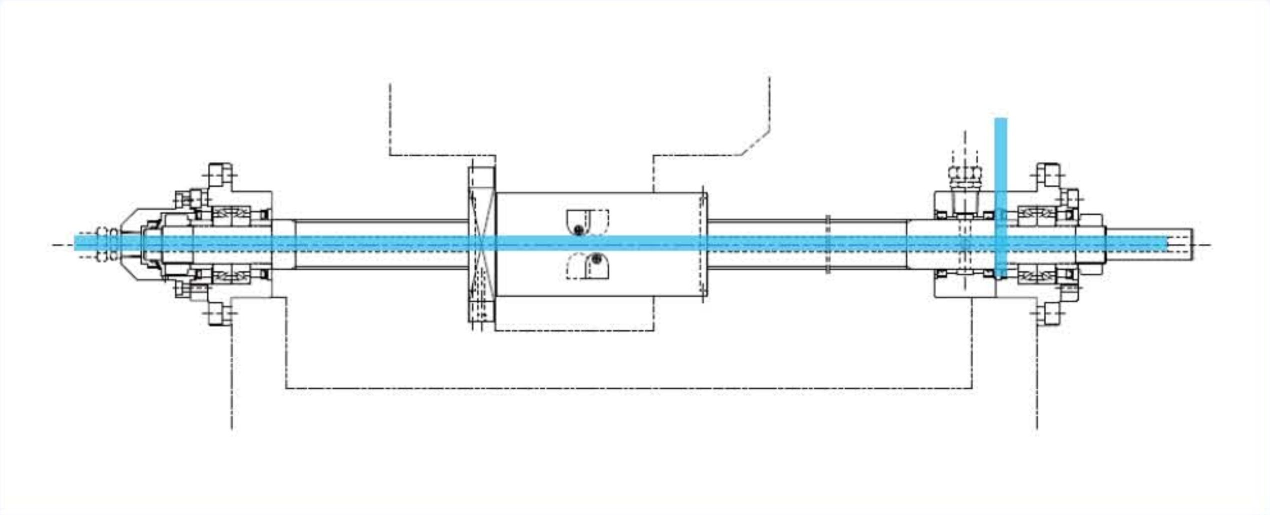

Fig. 2 Forced cooling in a hollow shaft ball screw

Additionally, ball screws for machine tools are generally preloaded to remove backlash and promote high-accuracy positioning, but this preload is a factor in heat generation as well.

For achieving both higher speed and higher accuracy of a traverse system using a ball screw, it becomes necessary to cool the ball screw itself. Hollow-shaft ball screws (Figure 2) have been produced by NSK since the 1980s to respond to these needs and have been adopted in many machine tools. However, a special processing machine is needed for the process of hollowing the relatively long and thin screw shaft, and the increase in production cost and lead time causes problems. In addition, machine tool manufacturers that attach importance to temperature control of the whole machine, especially temperature control of the surrounding table for mounting work, have recently called for achieving further accuracy.

Because of these situations, NSK took up the challenge to develop a ball screw that does not require hollowing of the screw shaft and has a cooling nut nearer to the table than the screw shaft. The development process and performance are introduced in the following sections.

2. The Challenge of a Nut Cooling Ball Screw

The ball screw nut is equivalent to the outer ring of a rolling bearing. In bearings used for high-speed main spindles, cooling of the outer ring is avoided due to the fear of preload increase and seizure by thermal contraction. Ball screws are considered to have a similar tendency. So, preload fluctuation during nut cooling was examined and the internal design was realized so that the preload did not increase.

Whereas shaft center cooling directly cools the screw shaft, which directly impacts traverse accuracy, nut cooling suppresses heat generation of the screw shaft by cooling the nut. Therefore, the nut cooling structure and cooling effect were investigated to get the equivalent cooling effect as shaft center cooling.

3. Using a Nut Cooling Ball Screw without Increasing the Preload

As stated above, cooling the bearing outer ring generates thermal contraction by the difference of temperature between the inner and outer rings. However, a ball screw has some extent of length in the axial direction, which is different from a bearing. Therefore, thermal contraction in the axial direction generates additional thermal contraction in the radial direction when the nut is cooled. The authors focused attention on this point and adopted a preload in the extended direction as the preload type the nut cooling ball screw (Figure 3). This offsets the influence of the preload increase by thermal contraction in the radial direction, and a ball screw was created without changing the preload amount, even though the nut was cooled.

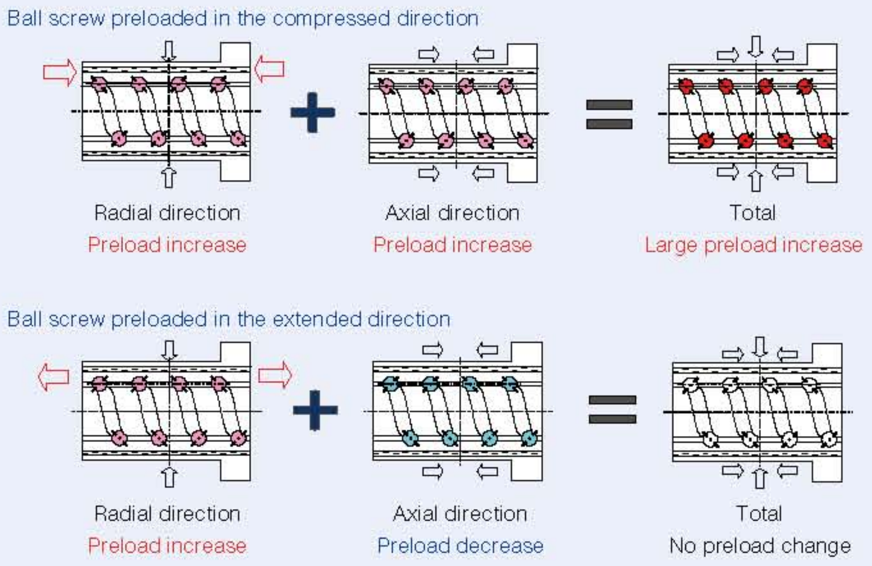

Fig. 3 Relationship between preloaded direction and thermal contraction direction

4. Cooling Capacity Equivalent to a Hollow Shaft Ball Screw

The basic cooling mechanism of a nut cooling ball screw is designed to circulate coolant into the through hole in an axial direction as shown in Figure 4. This mechanism enables the radial dimension to be identical to that of conventional ball screws for machine tools, which allows for easy replacement. In addition, it is possible to produce nut cooling ball screws with a general-purpose processing machine.

Next, the cooling capacity of this model is considered. Because the convection heat transfer coefficient by heat exchange in tube is proportional to the 0.8th power of the Reynolds number, the thinner the tube diameter, the higher the flow speed and resulting increase in cooling efficiency. Because the nut is generally shorter than the screw shaft, it is possible to bore a hole smaller than the through hole for shaft center cooling. Additionally, due to the longer contact length between the coolant and nut, the larger the cooling area; therefore, longer length and numerous through holes improve cooling. Although the individual through hole length of the nut cooling ball screw is short, setting up multiple cooling holes on the circumference of a circle secures sufficient overall length. The cooling effect was calculated using these parameters, the nut was designed to make the cooling capacity equivalent to shaft center cooling, and subsequent prototypes were evaluated.

Figure 5 shows temperature rise test results with each cooling system. The temperature rise values of shaft center cooling and nut cooling are equivalent, and the above-mentioned calculation results can be experimentally confirmed.

Here we consider the driving pattern of the nut and its cooling effect. The total heat release of a ball screw is calculated by multiplying the following three items:

1) Coefficient of heat transfer
2) Contact length of coolant and heat generation area
3) Difference of temperature between the coolant and heat generation area

The contact length of coolant and the heat generation area for shaft center cooling refers to the heat-generating area on the shaft, that is, the stroke length. When the nut stroke is short in shaft center cooling, the cooling effect is also small. Because coolant circulates in the nut, which is the heat-generating area in nut cooling, the length of the cooling area remains unchanged and the cooling effect does not depend on the driving pattern of the nut.

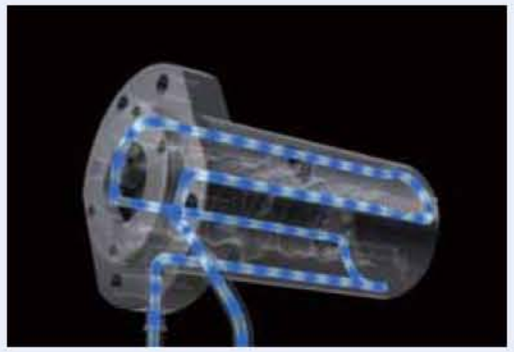

Fig. 4 Nut cooling mechanism

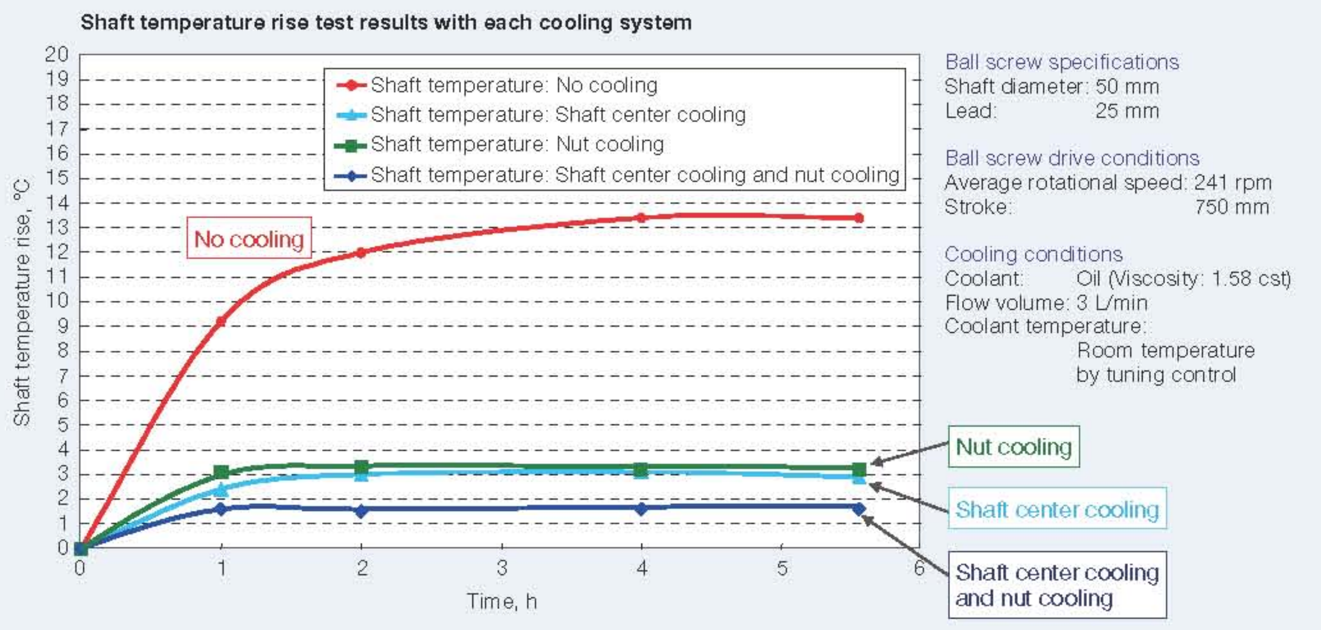

Fig. 5 Temperature rise test results

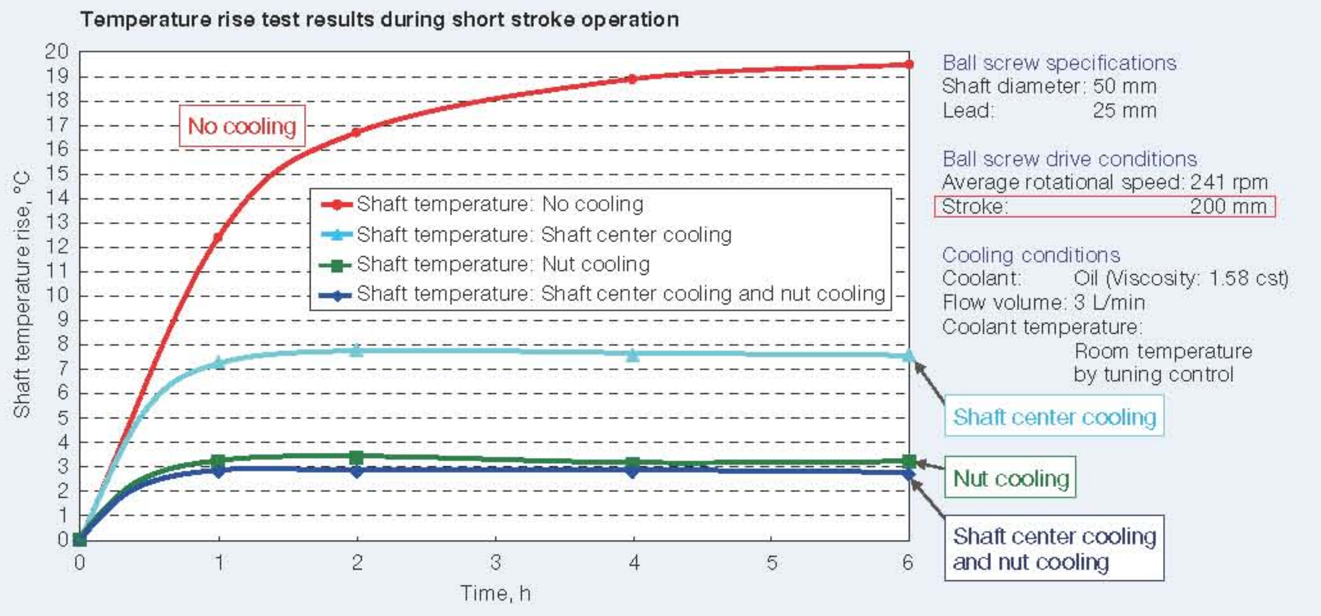

Fig. 6 Temperature rise test results during short stroke operation

Figure 6 shows the test results when making the stroke shorter with the temperature rise test conditions in Figure 5. Here the temperature rise values of shaft center cooling are larger than those in Figure 5, but the temperature rise values of nut cooling remain unchanged. From this result, the above-mentioned thought is experimentally confirmed.

5. Temperature Distribution

Figure 7 shows the temperature distribution results of a test table measured by thermography with no cooling, shaft center cooling, and nut cooling. It was found that shaft center cooling and nut cooling both highly reduce the screw shaft temperature compared with no cooling. It was also confirmed that nut cooling has a higher reduction effect on table temperature compared with shaft center cooling. Because the heat capacity of the test table is smaller than that of an actual table, however, it is likely that the effect on an actual machine will be smaller.

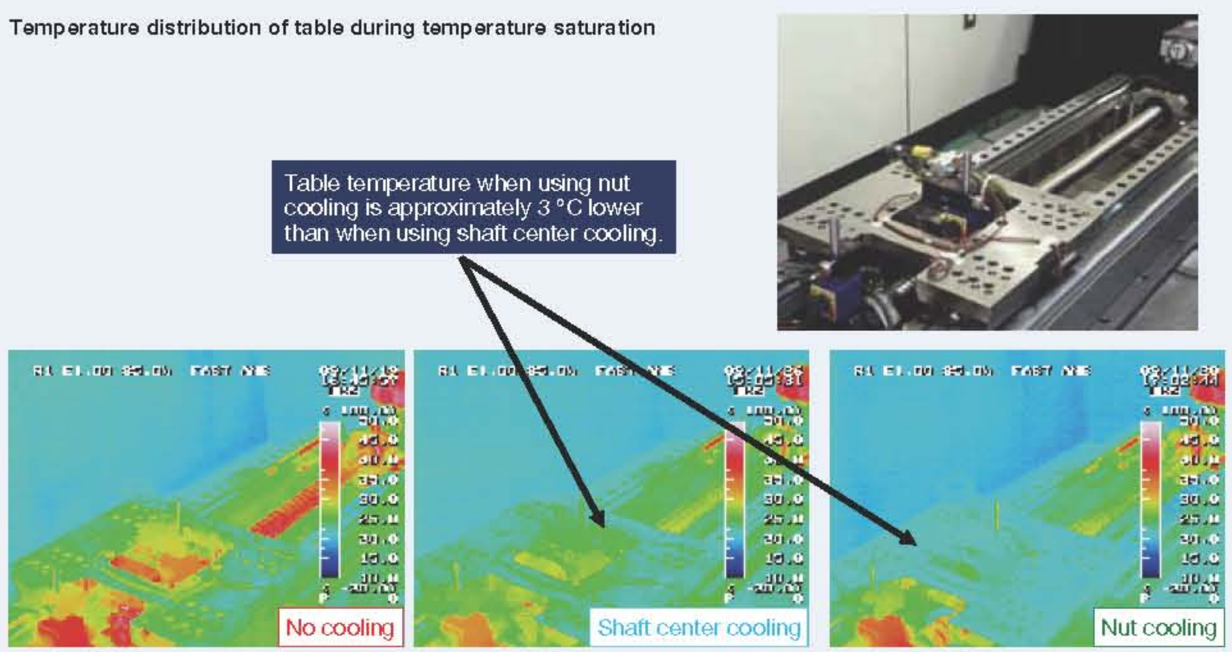

Fig. 7 Temperature distribution measurement results

6. Conclusion

The performance of the nut cooling ball screw was described with a focus on preload fluctuation and the cooling effect of nut cooling. We consider that the developed ball screw is low-cost and has the equivalent or more of a cooling effect than the shaft center cooling ball screw, and the adoption results are increasing. We look forward to making further contributions to the development of machine tools in the future.

Junji Minakuchi

Yutaka Nagai

Kazuhito Yamamoto

Ultra-High-Speed Precision NSKROBUST Angular Contact Ball Bearings for Main Spindles of Machining Centers

The bearings for the main spindles of machining centers have specific performance requirements, such as high-speed operation, high precision, and low heat-generation. In particular, demand is growing stronger not only for reduced runout per rotation (repetitive runout, RRO) in respect to running accuracy but also for reduced non-repeated runout per rotation (non-repetitive runout, NRRO). To meet these needs, NSK has created new ultra-high-speed precision NSKROBUST angular contact ball bearings for the main spindles of machining centers (Photo 1). These bearings utilize a newly developed TS cage, which successfully reduces the NRRO value by half during high-speed rotation and reduces temperature increase by 20 %. Further details are introduced below.

1. Configuration (Structure) and Specifications

Ultra-high-speed angular contact ball bearings for machine tools come in a lineup consisting of the ROBUST Series S Type, H Type, X Type, and Spinshot II XE Type to meet various purposes.

The ultra-high-speed precision NSKROBUST angular contact ball bearing for main spindles of machining centers are characterized by adoption of the new TS cage developed for H, X, and XE Type bearings with an inner diameter φ ranging between 30 and 100 mm and particularly designed to meet high-speed performance needs.

2. Features

The newly developed TS cage is made of high-rigidity super engineering plastic. Thanks to minimal deformation during high-speed rotation and high dimensional stability, this material allows for an even more optimized internal design and minimum runout of the cage during high-speed rotation.

The 70 mm inner-diameter-type bearing from this series was compared with a conventional bearing equipped with a standard phenol cage. The NRRO value of the new ROBUST Series bearing in the 12 600 rpm high-speed rotation range was 1/2 that of a conventional NSK bearing (Figure 1). Temperature increase in the 20 000 rpm range was lower in the new bearing by 20 % (Figure 2).

Photo 1 Ultra-high-speed precision NSKROBUST angular contact ball bearings for main spindles of machining centers

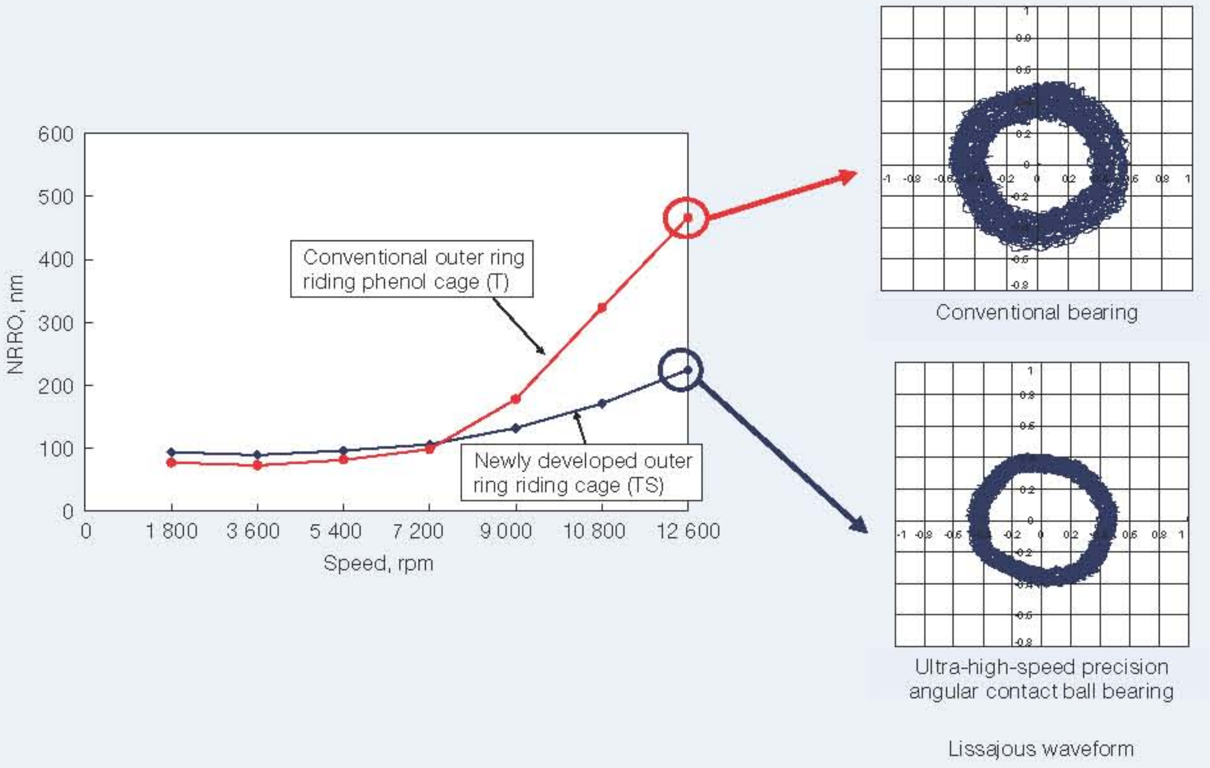

Fig. 1 NRRO measurement of bearing only

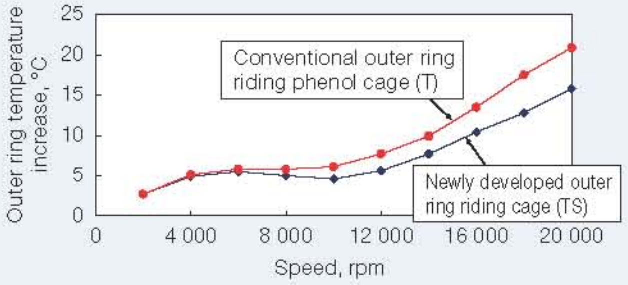

Fig. 2 Bearing temperature test results

3. Applications

This bearing is superior for main spindles of machining centers requiring both very high speeds and high running accuracy, such as mold machining devices.

4. Summary

Compared with conventional bearings with a phenol cage, the ultra-high-speed precision NSKROBUST angular contact ball bearing for main spindles of machining centers reduces the NRRO value by half during high-speed rotation and reduces temperature increase by 20 %. These functional improvements not only further improve the speed and machining accuracy of the main spindle but also contribute to high workpiece quality in mold-making and the like.

Long-Life Thrust Ball Bearings with a Highly Reliable Cage for Agricultural Machinery HSTs

With increased global population, demand for food, biofuel, and so forth has increased, and subsequently, demand has also risen for agricultural machines. Agricultural machines such as tractors, combines, and the like use hydraulic static transmissions (hereafter called HSTs, Figure 1) as continuous variable transmissions. In recent years, engine output has become higher and higher in order to enhance the work efficiency of agricultural machines. This increases the load on bearings, leading to growing demand for thrust ball bearings with long lifespans and high reliability for use in HSTs.

The following text introduces long-life thrust ball bearings with a highly reliable cage for agricultural machinery HSTs (Photo 1) These bearings developed by NSK have a lifespan of more than twice as long as conventional thrust ball bearings used in the HSTs of agricultural machines.


Photo 1 A long-life thrust ball bearing with a highly reliable cage for agricultural machinery HSTs

1. Features

This special bearing has a lifespan of over twice that of conventional ball bearings thanks to the following technologies. (Figure 2)

(1) Material technology

Flaking occurs with conventional ball bearings when used under high load conditions. This product adopts EP steel, which has strong resistance to internal fatigue under high load conditions, for its inner and outer rings. A special heat treatment for resistance to surface fatigue is also carried out on the inner ring, outer ring, and balls to prevent flaking.

(2) Adoption of a highly reliable cage

Depending on the lag or lead of the balls, large forces or repeated stress on the cage is generated. Particularly under high load conditions, conventional iron cages are unable to tolerate this repeated stress and occasionally break down. To resolve this, NSK uses plastic resistant to repeated stress to enhance cage reliability under high load conditions.

2. Specifications

Product numbers and specifications are shown in Figure 3.

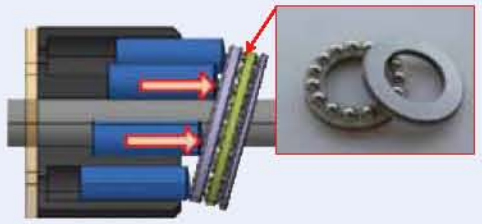

An HST (Hydraulic Static Transmission) is a static continuously variable mechanism that combines a hydraulic pump and hydraulic motor. Thrust ball bearings for HSTs are used tilted against the part that receives piston load as shown in Figure 1. They have the following characteristics:

- As bearings are used in the tilted state, they bear axial load + a force component (radial load).
- Given that the load on the bearing differs according to the piston position, the bearings bear eccentric load.

Fig. 1 A hydraulic static transmission (HST) with thrust ball bearings

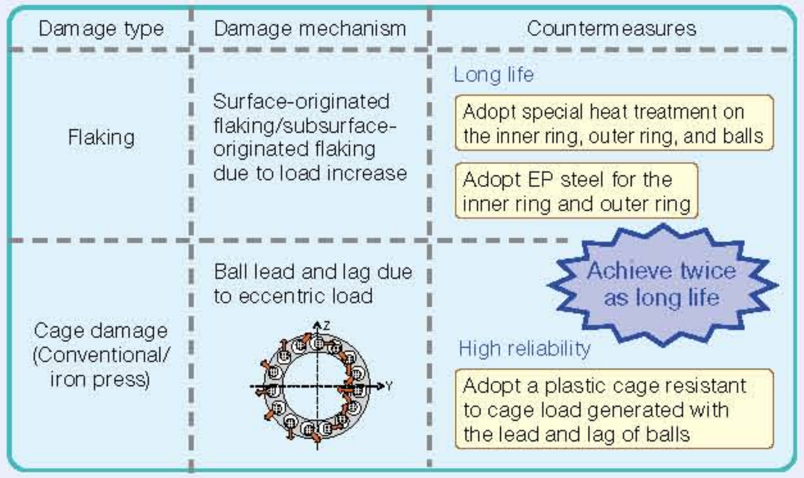

Damage type	Damage mechanism	Countermeasures
Flaking	Surface-originated flaking/subsurface-originated flaking due to load increase	Long life Adopt special heat treatment on the inner ring, outer ring, and balls Adopt EP steel for the inner ring and outer ring
Cage damage (Conventional/ iron press)	Ball lead and lag due to eccentric load	Achieve twice as long life High reliability Adopt a plastic cage resistant to cage load generated with the lead and lag of balls

Fig. 2 Types of bearing damage and countermeasures

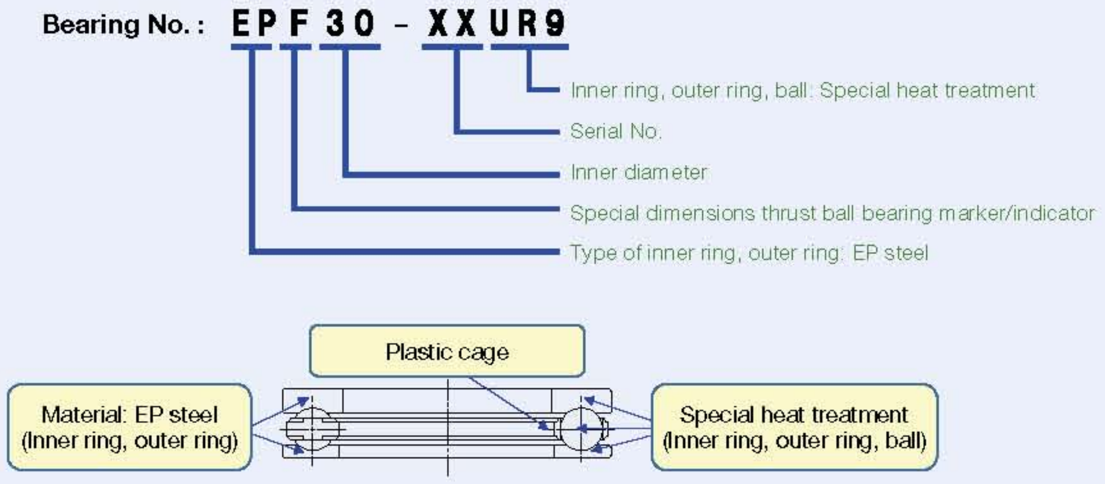

Fig. 3 Specifications and example bearing number for a long-life thrust ball bearing with a highly reliable cage for agricultural machinery HSTs

3. Summary

NSK has already started mass production of long-life thrust ball bearings with a highly reliable cage for agricultural machinery HSTs. We will continue our product development efforts to respond to needs for higher reliability and longer life.

Cylindrical Roller Bearings for Centrifugal Chillers

Centrifugal chillers are mainly used for the air-conditioning of large facilities such as office buildings, factory buildings, and so forth.

With the growing need to reduce CO_2 and conserve energy to fight global warming, demand for centrifugal chillers with high energy efficiency has increased in recent years. Air-conditioning systems of large facilities tend to consume massive power and fuel, which makes them a prime target from the perspective of environmental preservation.

Cylindrical roller bearings that can absorb axis elongation caused by temperature increase are suitable for use at the free end of a compressor axis. However, given that centrifugal chillers are used at high speeds where the $d_m \cdot n$ value ranges from 1 200 000 to 1 300 000, this leads to concern for skidding caused by relative slippage between the roller and inner ring raceway and subsequent damage of the rib face and roller end face. To date, combined angular contact ball bearings have been used as a result of this problem.

The following introduces new cylindrical roller bearings for centrifugal chillers (Photo 1), considered to be the best bearings for supporting the free end of the compressor axis in centrifugal chillers.

1. Features

(1) Skidding resistance

Photo 2 shows an example of the inner ring raceway after a skidding test.

By optimizing the internal design, skidding damage does not occur in high-slipping speed ranges, resulting in high PV values that significantly exceed the actual usage conditions of the centrifugal chiller (Photo 2).

Photo 1 Newly developed cylindrical roller bearing for centrifugal chillers

Test conditions
Rotating speed: 40 000 rpm
PV value: 125
Slipping speed: 28
Test time: 10 h
(Note) PV value and slipping speed are ratios in respect to actual values of identical conventional applications.

Photo 2 Inner ring raceway of a newly developed bearing after skidding test

Figure 1 shows an analysis of the relationship between radial load and PV value.

(2) High reliability in high speeds

Optimization of the design of the outer ring rib and improvement of accuracy have enhanced wear resistance and seizure resistance of the rib face and roller end face edge in high-speed rotations over four times the limiting speed of standard cylindrical roller bearings.

Bearing: Cylindrical roller bearing (NU307)
Size: ϕ 35 mm × ϕ 80 mm × 21 mm
Speed: 40 000 rpm
(Note) The PV value and slipping speed are ratios in respect to conventional allowances.

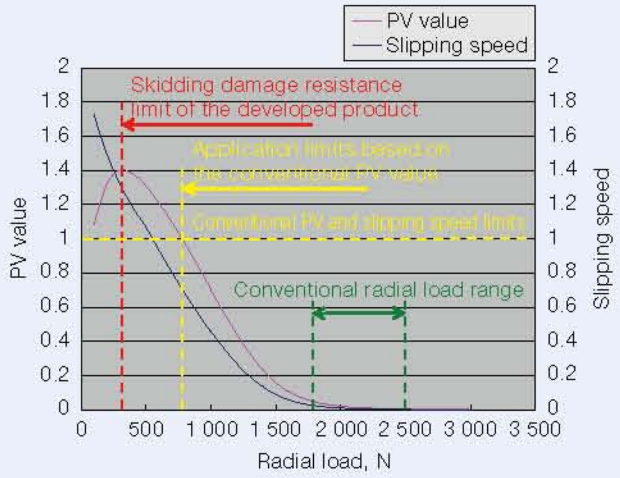

Fig. 1 Analysis of the relationship between radial load and PV value

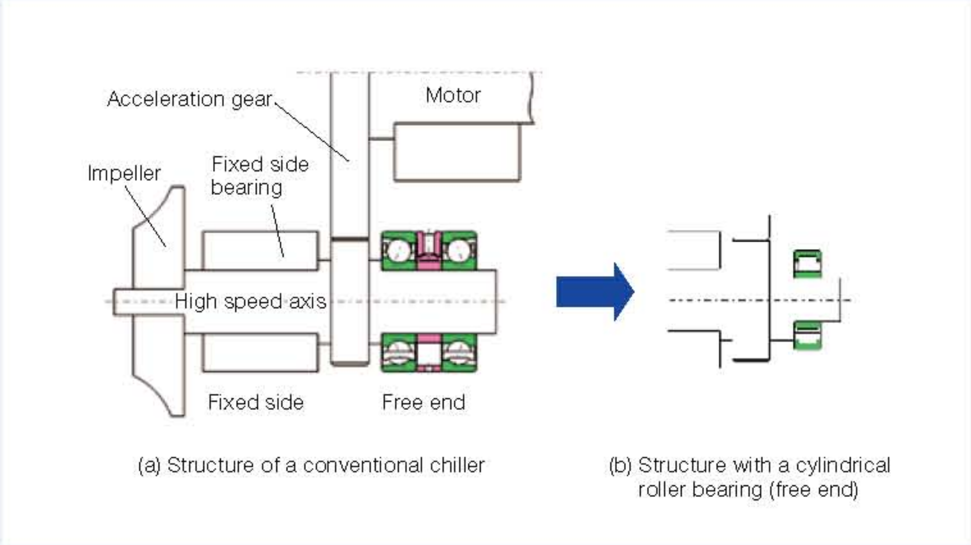

(a) Structure of a conventional chiller

(b) Structure with a cylindrical roller bearing (free end)

Fig. 2 Structure of a centrifugal chiller around the bearings

(3) Compact and low torque features

Bearings have been made compact by reducing the number of rows of bearings (no need for spacers) and increasing the load volume of the bearing (Figure 2). The external dimensions have been made about 30 % smaller and the total bearing width has been reduced by about 70 %.

In addition to reduction in bearing torque with the decrease in the number of rows and bearing size, the addition of a notch to the outer diameter of the cage has improved lubricant oil drainage, allowing for realization of even lower torque.

Figure 3 shows a graph of calculated torque when a double-row angular contact ball bearing with an inner diameter φ of 50 mm is replaced with the newly developed cylindrical roller bearing with a φ 35 mm diameter. The graph shows that the torque has been considerably reduced by about 50 %.

2. Applications

This bearing is intended to support the free end of the compressor axis of centrifugal chillers.

In particular, it is suited for use under light load conditions such as in structures with built-in (gearless) motors.

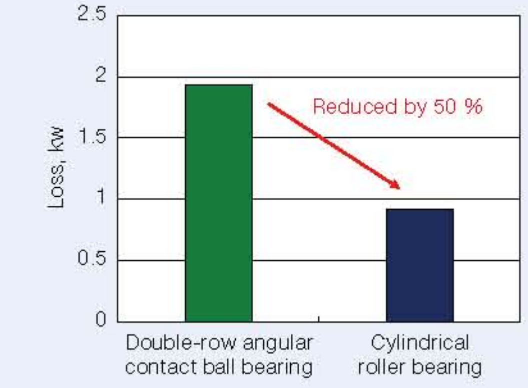

Fig. 3 Comparison of torque between an angular contact ball bearing and the newly developed cylindrical roller bearing

3. Summary

Cylindrical roller bearings for centrifugal chillers contribute to the realization of compact, low-loss centrifugal chiller compressors and high efficiency centrifugal chillers.

BNEQARTET—Long-Life Ball Bearings for Washing Machines

In the European and Chinese markets, general horizontal-axis washing machines have larger or longer drums to increase washing capacity. This, however, increases the load on the bearings supporting the drum and reduces their life. Therefore, demand for long-life ball bearings is increasing.

In response to such demand, NSK has commercialized BNEQARTET—long-life ball bearings for washing machines (Photo 1).

1. Configuration, Structure, and Specifications

The bearing ring, which is the main component of this long-life ball bearing, is made of a material developed by NSK by optimizing alloy components and using unique techniques to control material cleanliness. As a result, we have produced ball bearings that resist various types of damage to achieve long life.

2. Features

(1) Long life in regard to subsurface-originated flaking

The main reasons for subsurface-originated flaking are changes in material cleanliness and composition. Cracks occur and advance from the areas around material inclusions where stress accumulates, eventually leading to flaking. With the new product, alloy components were optimized and material cleanliness was managed to improve bearing quality and realize long life (Figure 1).

(2) Long life in regard to other damage types

In addition to subsurface-originated flaking, there are various other types of flaking including surface-originated flaking caused by the concentration of stress originating from indentations on the bearing ring surface, white structure flaking caused by the generation of hydrogen due to the decomposition of lubricant, and high-temperature flaking. The developed material allows the ball bearings to achieve long life by resisting a diverse range of damage types (Figures 2 to 4).

3. Applications

These bearings are suitable not only for supporting horizontal drum-type washing machines but also can be used under high load conditions in general industrial machines and the like.

Table 1 shows the product lineup.

Photo 1 BNEQARTET—long-life ball bearings for washing machines

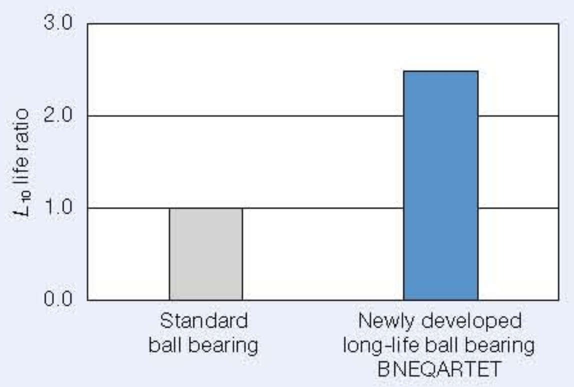

Fig. 1 Life ratio regarding subsurface-originated flaking

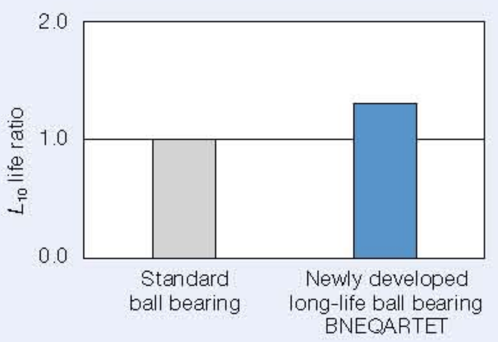

Fig. 2 Life ratio regarding surface-originated flaking

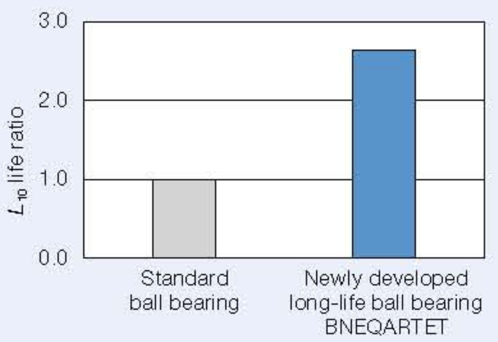

Fig. 3 Life ratio regarding white structure flaking

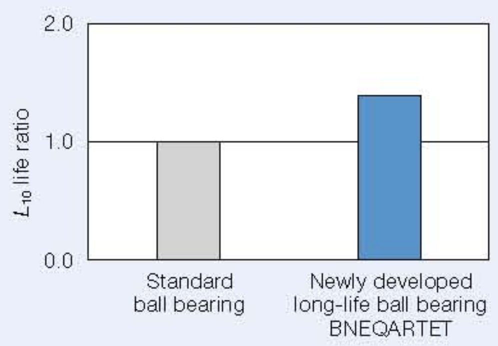

Fig. 4 Life ratio regarding high-temperature flaking

Table 1 Product lineup of long-life ball bearings for washing machines

Model No.	Main dimensions (mm)		
	Inner diameter	Outer diameter	Width
6205	25	52	15
6206	30	62	16
6305	25	62	17
6306	30	72	19
6307	35	80	21

4. Summary

Long-life ball bearings for washing machines were developed to withstand high load conditions. We will continue our development efforts to meet the needs of our diverse users.

SPACEA Series—Solid-Lubricant-Coated Bearings for High Temperatures

Solar batteries, LEDs, lithium ion batteries, and so forth are manufactured in clean environments to achieve high quality and yield. In particular, during deposition and baking processes under high-temperature conditions, grease or conventional binders contained in solid-lubricant film become the source of outgas. For this reason, except for high-end models, deposition and baking systems have short lives and non-lubricated bearings need to be frequently replaced. Realizing long bearing life is therefore a huge challenge.

NSK has developed unique solid-lubricant-coated bearings with excellent durability under high temperatures that do not contain binders that cause outgassing (Photo 1).

Photo 1 Newly developed bearing

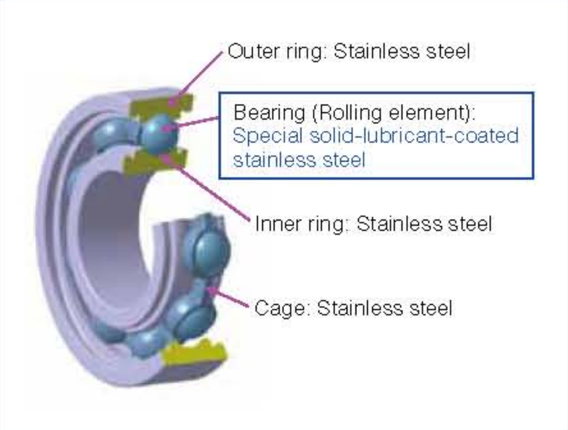

Fig. 1 Newly developed bearing structure

1. Configuration, Structure, Specifications

Figure 1 shows the structure and specifications of the developed product.

Balls using the bearings are made of martensitic stainless steel and coated with a newly developed special solid lubricant, which is one of the main features of this product. The bearing consists of martensitic stainless steel inner and outer rings and an austenitic stainless steel cage and shield plate.

The developed product is available in twelve sizes as shown in Table 1.

2. Features

(1) Durability

The newly developed special solid lubricant coating is used in the bearings to improve adherence with base materials such as stainless steel. Compared with conventional non-lubricated bearings, life in air is three times longer and life in vacuum is eight times longer (Figure 2).

(2) Low outgas

When outgas exceeds a certain level, it affects the quality of products, resulting in decreased yield. With these bearings, very little outgas is produced, much like conventional non-lubricated bearings, due to the use of a solid-lubricant coating that does not contain binders, the cause of outgas (Figure 3).

Outgas refers to a gas component mainly discharged from organic substances such as binders. Binders are substances such as resin that enhance adhesion of solid lubricants to the base material.

Table 1 Boundary dimensions of solid-lubricant-coated bearings for high temperatures

Basic bearing number	Main dimensions (mm)		
	Inner diameter	Outer diameter	Width
608	8	22	7
6000	10	26	8
6200		30	9
6001	12	28	8
6201		32	10
6002	15	32	9
6202		35	11
6003	17	35	10
6203		40	12
6004	20	42	12
6204		47	14
6006	30	55	13

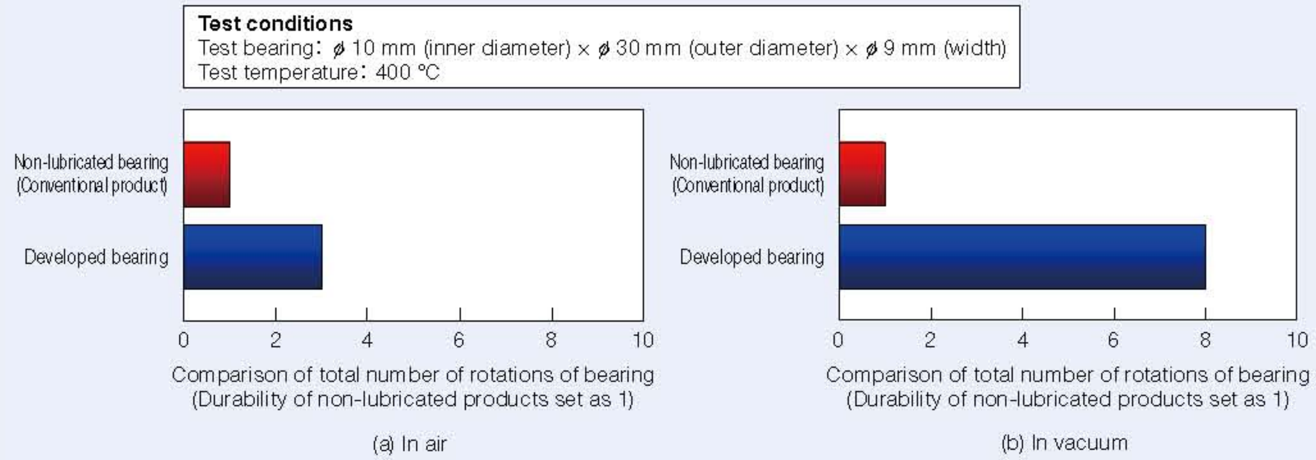

Fig. 2 Life ratio comparison of durability test results under high temperature conditions

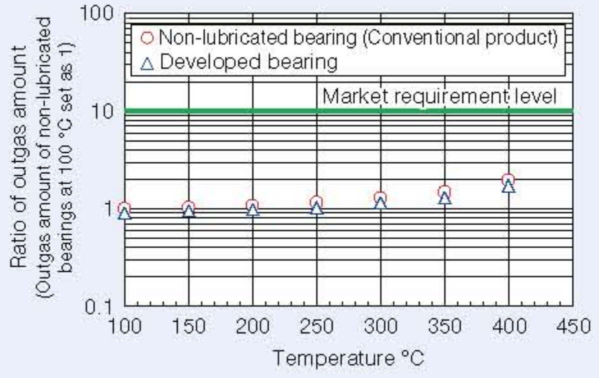

Fig. 3 Outgassing from bearings

3. Applications

This product is suitable for high temperature applications such as deposition and baking systems used in the production of solar batteries, LEDs, and lithium ion batteries.

Use of this product allows for a long lifespan in high temperature systems and extends maintenance intervals. Because very little outgas is produced, clean manufacturing environments can be maintained.

4. Summary

"SPACEA Series—solid-lubricant-coated bearings for high temperatures" contribute to extending maintenance periods in high temperature conditions as well as maintaining clean manufacturing environments.

NSK will continue its efforts to develop highly functional products and enhance the SPACEA series in order to meet sophisticated demands in a broad range of industrial fields.

Ball Screws with X1 Seals for Machine-Tool Applications

Ball screws normally used for machine tools are shielded with covers and the like, but still, entry of foreign particles such as machining dust and coolant cannot be completely prevented. In recent years, more and more machine tools have used an automatic greasing mechanism to lubricate ball screws. However, the grease used for such mechanisms has high fluidity, causing it to flow out of the ball screws easily. For this reason, ball screws for machine tools require dust resistance and grease-sealing capacity (the ability to retain grease).

In 2005, NSK developed highly dust-resistant contact-type lip seals, and since then, they have been widely applied in the presence of various types of foreign particles. In 2007, we developed the "Grease-Sealed-Type A1 Seals," which are popularly used in the injection molding machine market. Now, by improving these sealing technologies, we have developed and commercialized ball screws with X1 seals. These seals offer high dust resistance and grease sealing capacity suitable for machine tools.

1. Structure and Specifications

Ball screws use two types of our newly developed X1 seals: a dust-proofing seal with a lip at its tip that is tilted towards the outside of the nut, and a grease retaining seal tilted towards the inside of the nut (Figure 1).

The following shows the product specifications:

(1) Suitable model: X1 seals are compatible with the following two types of nuts (Figure 2):
- HMS for machine tools (Nut type ZFRC)
- HMD for machine tools (Nut type EM)

(2) Tolerance class: JIS C3, C5
(3) Combination of shaft diameter and lead: Shown in Table 1 Product Lineup.

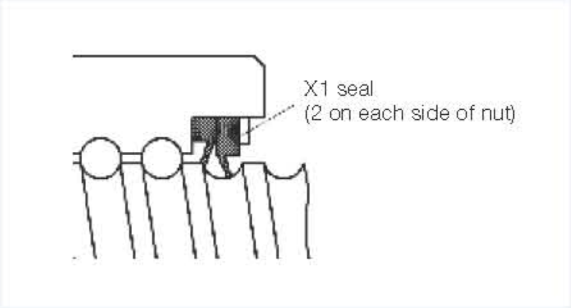

Fig. 1 Structure of the newly developed X1 seal

2. Features

(1) High dust resistance

X1 seals have remarkably improved ability to prevent the entry of foreign particles due to their enhanced seal design.

Comparative tests conducted to verify dust resistance confirmed that the penetration rate of foreign particles is 1/30 that of standard seals (Figure 3). X1 seals are thus expected to improve the durability of ball screws in the presence of various foreign particles compared to standard seals.

(a) HMS type

(b) HMD type

Fig. 2 Ball screw with X1 seals

Table 1 Product lineup

(a) HMS type

Model	Shaft diameter [mm]	Lead [mm]	Basic load rating [kN]	
			Dynamic load C_a	Static load C_{0a}
ZFRC4010-10	40	10	52.0	137
ZFRC4012-10		12	61.0	155
ZFRC4508-10	45	8	37.3	118
ZFRC5010-10	50	10	57.7	175
ZFRC5012-10		12	77.6	214

(b) HMD type

Model	Shaft diameter [mm]	Lead [mm]	Basic load rating [kN]	
			Dynamic load C_a	Static load C_{0a}
EM4016-4E	40	16	57.1	130
EM4020-6E		20	66.9	165
EM4516-4E	45	16	59.6	145
EM4520-6E		20	69.1	186
EM5016-4E	50	16	61.8	160
EM5020-6E		20	73.2	206

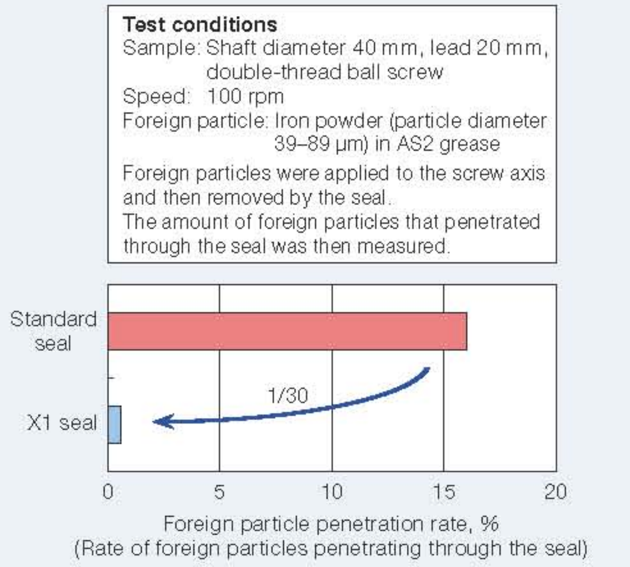

Test conditions
Sample: Shaft diameter 40 mm, lead 20 mm, double-thread ball screw
Speed: 100 rpm
Foreign particle: Iron powder (particle diameter 39–89 μm) in AS2 grease

Foreign particles were applied to the screw axis and then removed by the seal.
The amount of foreign particles that penetrated through the seal was then measured.

Fig. 3 Penetration rate test results

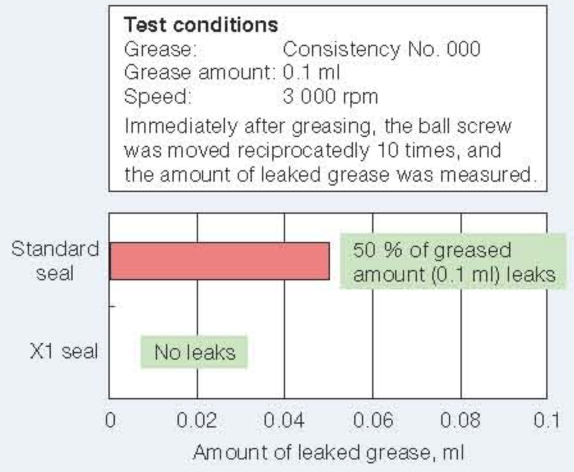

Test conditions
Grease: Consistency No. 000
Grease amount: 0.1 ml
Speed: 3 000 rpm
Immediately after greasing, the ball screw was moved reciprocatedly 10 times, and the amount of leaked grease was measured.

Fig. 4 Amount of leaked grease immediately after greasing

(2) Improved grease retention

The grease retention ability of the ball screws with X1 seals is excellent, especially during automatic greasing. When standard seals are used, half of the grease applied may leak due to scattering immediately after greasing under certain conditions. In contrast, X1 seals are able to prevent leakage by scattering and the like (Figure 4).

Contamination of retained grease is controlled by high dust resistance (see (1)), allowing for minimum greasing of ball screws with X1 seals. Furthermore, X1 seals are effective for preventing the scattering of grease.

(3) Low torque

The X1 seal is designed so that a total of four seals can be attached to one nut, two on each side. This raises concerns regarding increased heat generation, but low heat generation has been realized by optimizing the seal shape and using lip material with low friction characteristics.

3. Applications

These ball screws are suitable for machine tools and applications requiring high dust resistance and grease-sealing capacity.

4. Summary

Ball screws with X1 seals are intended mainly for machine tools, but NSK is planning to expand the product lineup for use in other applications.

HTF-SRE Large, High-Speed, High-Load Capacity Ball Screws

Hydraulic cylinders are often used for driving units designed to absorb high load in injection molding machines.

In recent years, however, electrical driving units such as rotary motors and ball screws have been increasingly used thanks to their improved controllability, environmental friendliness, lack of hydraulic oil, and energy-saving features such as reduced power consumption. Some innovative applications of these electrical driving units include the electrically driven injection molding machine and servo press, which mostly use HTF high load ball screws.

Medium and small injection molding machines are mainly used for the molding of thin-walled products like mobile phones, the light-guiding plates of LCD panels, and connectors in automobiles. These molding processes require molten resin to be supplied at high speed to the tip of narrow grooves in the mold. In 2005, NSK commercialized the HTF-SRC ball screw for such high-speed injection applications. On the other hand, molding machines for disks and PET bottle caps require many cycles to enhance production volume. For these products, shortening the mold open/close time is indispensable for shortening the cycle time. To meet such shorter and high-speed mold open/close needs, NSK commercialized the HTF-SRD ball screw in 2007.

As such small and medium molding machines are produced in large lots, the combination of shaft diameter and lead is limited. For this reason, the costs of producing the rotatable parts of these ball screws, which have especially complicated shapes, can be reduced by using molds.

Furthermore, over the last couple of years, large injection molding machines for producing large resin parts, such as automobile inner panel interior parts and storage cases, are facing needs for high-speed injection and high-cycle molding that until now had been necessary only in small- and medium-sized molding machines. Likewise, demand for high-cycle molding are also strong for servo presses for press-molding the body panels of automobiles. Presently, large, conventional tube recirculation HTF-type ball screws are used for these machines, but they present two problems:

(1) Large steel balls are used to enhance load resistance, but this increases shock load on the circulation parts during ball rotation, preventing increases in rotational speed.

(2) Large machines are produced in small numbers, and the required combinations of shaft diameter and lead are broad.

NSK has thus developed the HTF-SRE ball screw: a large, high-speed, high-load capacity ball screw (Photo 1) that adopts a new ball-circulation method to resolve these problems.

1. Features

The HTF-SRE ball screw adopts a recirculation method that uses a deflector, a component designed to scoop balls in the tangential direction to realize smooth ball rotation (Figure 1), and a conventional high-load HTF design. New HTF-SRE ball screws now have the following features:

(1) High speed

Use of the deflector-circulation method is based on a design that scoops balls in the tangential direction of the lead, achieving a feed speed of 1.4 to 2 times that of HTF ball screws with the conventional tube-recirculation method.

(2) Supports diverse shaft diameter and lead combinations

The deflector used in recirculation can be made easily by machining and supports diverse shaft diameter/lead combinations.

(3) Improved resistance to momentum

To prevent the balls from colliding, a resin-holding piece is inserted between the balls (S1 specifications). This sharply enhances resistance to momentum.

Photo 1 HTF-SRE ball screw

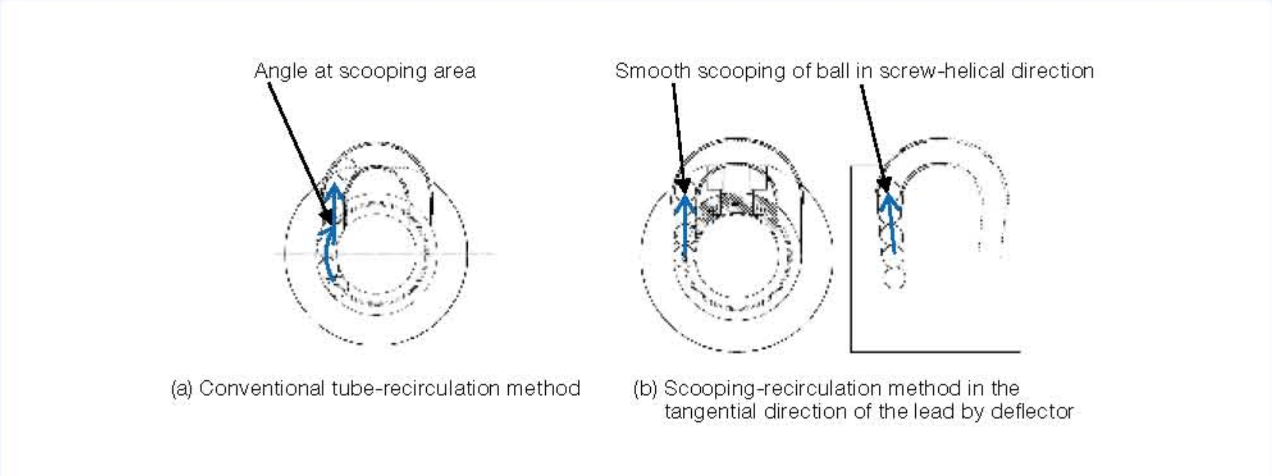

(a) Conventional tube-recirculation method

(b) Scooping-recirculation method in the tangential direction of the lead by deflector

Fig. 1 Comparison of conventional tube-recirculation and deflector-tangential-recirculation

2. Specifications

- Ball recirculation method: Scooping of ball in tangential direction by deflector
- Permissible $d{\cdot}n$ value: 100 000
  (d: Shaft diameter (mm), n: Rotational speed (rpm))
- Accuracy: JIS C5, Ct7
- Table 1 shows shaft diameter/lead combinations.
- Table 1 also shows maximum rotational speed (allowable rotational speed) based on the $d{\cdot}n$ value allowance.
- Table 2 shows the maximum feed speed for typical combinations of shaft diameter and lead.

3. Applications

HTF-SRE ball screws are suitable for large injection molding machines requiring high-speed injection, machines requiring high-speed mold opening/closing, and high-speed servo presses.

Table 1 Combination of shaft diameter and lead and allowable rotational speed

Shaft diameter (mm)	Lead (mm)							Allowable rotational speed (rpm)
	25	…	30	…	70	…	80	
140	←	—	—	—	→			714
160	←	—	—	—	—	—	→	625
200			←	—	—	—	→	500

Note 1 Any lead can be used within the supported range (←→).
Note 2 For leads above 50 mm, double-thread screws can also be used.

Table 2 Maximum feed speeds for typical combinations of shaft diameter and lead

Unit: rpm

Shaft diameter (mm)	Lead (mm)							
	25	30	32	40	50	60	70	80
140	297	357	380	476	595	714	833	—
160	260	312	333	416	520	625	729	833
200	—	250	266	333	416	500	583	666

NSK Roller Guides Equipped with V1 Seals

Roller guides refer to linear guides with rolling elements made of rollers. They are used in various applications requiring high rigidity and high-load capacity, such as in machine tools. However, in production sites generating fine powder, the entry of foreign particles into the roller guide can cause abnormal wear of the raceway surface, circulatory problems, and damage in a short time.

To help prevent this, roller guides are covered, but this is not 100 % effective. To prevent damage caused by foreign particles, it is important to enhance the dust resistance of the roller guides themselves.

NSK roller guides equipped with V1 seals are roller guides with remarkably enhanced dust resistance thanks to the use of newly developed V1 seals (Photo1).

1. Structure and Specifications

NSK roller guides equipped with V1 seals consist of an RA series roller guide and newly developed V1 seals with high dust resistance (Figure 1).

The new V1 contact seals are made of materials with higher wear resistance than that of conventional sealing materials. They are able to demonstrate strong, long-lasting dust resistance against foreign particle entry from the edge of the slider.

Furthermore, by inserting the NSK K1 lubricating unit between the highly dust-resistant V1 seals and sliders, the lubricity of the seal and raceway surface can be improved.

Figure 1 shows the attachment of lubrication unit NSK K1 to both sides of a slider. The number of units attached can be increased as necessary.

To prevent foreign particles from accumulating in the rail attaching holes, a hole cap and upper rail cover with excellent dust resistance are available.

Presently, the lineup of NSK roller guides equipped with V1 seals consists of three models: RA35, RA45, and RA55.

2. Features

(1) High dust resistance

The reduction of the foreign particle entry into the roller guide contributes to a longer life span of roller guides in environments where they are exposed to such particles.

Photo 1 NSK roller guides equipped with V1 seals

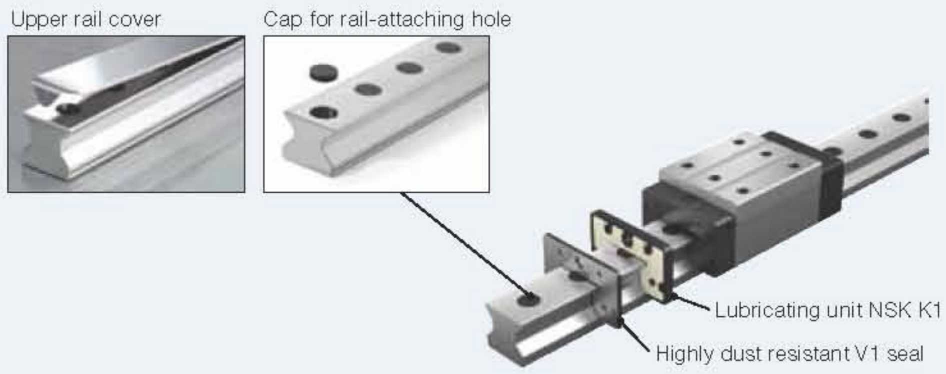

Fig. 1 Structure of the roller guide equipped with V1 seals

(2) Improved seal durability

The V1 seals boast higher wear resistance than before due to an improved shape and new material, allowing them to maintain high dust resistance over a long period of time. Moreover, even if the lubricated state of the seal-sliding surface is poor, damage such as gouging is less likely to occur.

Figure 2 shows the results of a wear resistance test of the seal. It compares the wear amount of a V1 seal and a conventional seal run under the same working conditions. The results show that V1 seals have improved wear resistance compared with conventional seals.

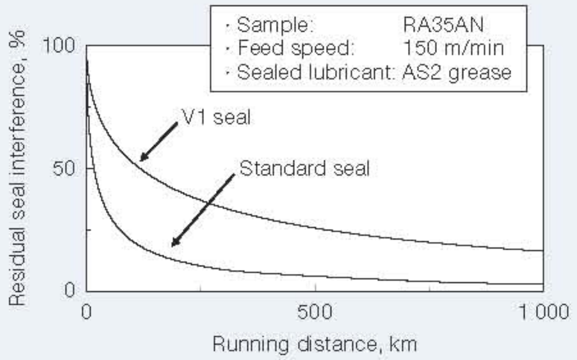

Fig. 2 Seal durability test results: amount and rate of wear

3. Applications

These roller guides are suitable for machine tools used in environments where considerable fine powder is produced, such as during the cutting of cast iron, graphite, and the like.

4. Summary

Developed based on the roller guide RA series popularly used in machine tools, NSK roller guides equipped with V1 seals have been designed for improved durability against foreign particles.

The current lineup consists of three models, RA35, RA45, and RA55, in order to meet the various needs of machine tool users. NSK plans to introduce other models to meet market needs.

Random-matching, High-Precision-Grade RA Series Roller Guides

Among NSK's linear guide products, the medium preload products of the RA series roller guides, which use rollers as their rolling element, boast the world's highest level of performance (high load capacity and high rigidity) and are used extensively, mainly in machine-tool applications. The slight preload products of this series have an optimized preload to meet long life needs and are used in many areas, such as liquid crystal manufacturing machines and transportation equipment.

The market demands that NSK deliver products in a short time and improve equipment precision. To meet these short delivery times, NSK was the first in the industry to offer Random-matching ball guides, which allow various rails and slides to be combined as desired. NSK also offers this Random-matching feature in the roller guide RA series but only with middle preload products with a precision (P6) grade.

To meet further high-precision needs, NSK has developed Random-matching, high-precision (P5) grade RA series roller guides consisting of not only middle preload products but also slight preload products (Photo 1).

1. Features

(1) Improved motion accuracy (running parallelism)

Running parallelism is a precision parameter indicating the linearity of slide motion. When the slide moves, it can be expressed as variations in the mounting datum surface of the slide in respect to the mounting datum surface of the rail. By processing the raceway of the rail and the mounting datum surface at high accuracies, the Random-matching, high-precision-grade RA series, which has a running parallelism that is equivalent to high-precision (P5) grade accuracy, is realized, even in slight preload products. As a result, the series improves equipment precision (Figure 1).

(2) Long life

As the amount of preload has been reduced in slight preload products, their life has been increased by about 4 times that of medium preload roller guides and about 8 times that of ball guides. These developed products also include slight preload products to respond to needs for long life in Random-matching products.

Photo 1 Random-matching, high-precision-grade RA series roller guides

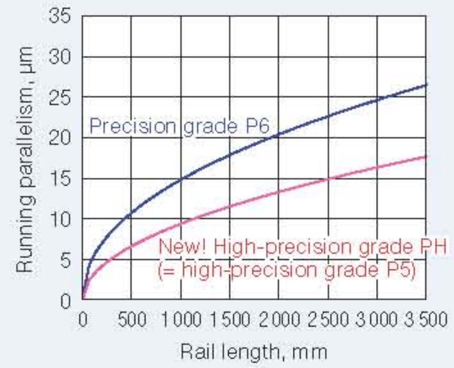

Fig. 1 Running parallelism of Random-matching, high-precision-grade RA series

Table 1 Lineup of Random-matching, high-precision-grade RA series

Series size	Slide model						Random-matching, high-precision grade (PH)	
	AN	AL	BN	BL	EM	GM	Slight preload ZZ	Medium preload ZH
RA25	○	○	○	○	○	○	○	○
RA30	○	○	○	○	○	○	○	○
RA35	○	○	○	○	○	○	○	○
RA45	○	○	○	○	○	○	○	○
RA55	○	○	○	○	○	○	○	○
RA65	○	—	○	—	○	○	○	○

(3) Response to short delivery needs

As the Random-matching, high-precision RA series roller guides are handled as standard stock, NSK can meet short delivery deadlines when slides need to be added or replaced. Thus, changes in slide models can be dealt with flexibly when sudden design changes occur.

(4) Long-term, maintenance-free operation

The lubrication unit "NSK K1" supplies lubrication oil to the raceway during sliding by seeping oil from porous resin with a large amount of lubrication oil. Mounting this unit allows long-term, maintenance-free operation.

2. Specifications

Table 1 shows the combination of product sizes and slide models. Size refers to the approximate rail width (mm). The slide model is classified according to its appearance as shown in Figure 2. It is possible to combine slides of different models to one rail.

3. Applications

Medium preload products are suitable for applications requiring high rigidity such as machine tools, automotive manufacturing equipment, and so forth, while slight preload products are suitable for a broad range of purposes such as transportation equipment involved in liquid crystal manufacturing.

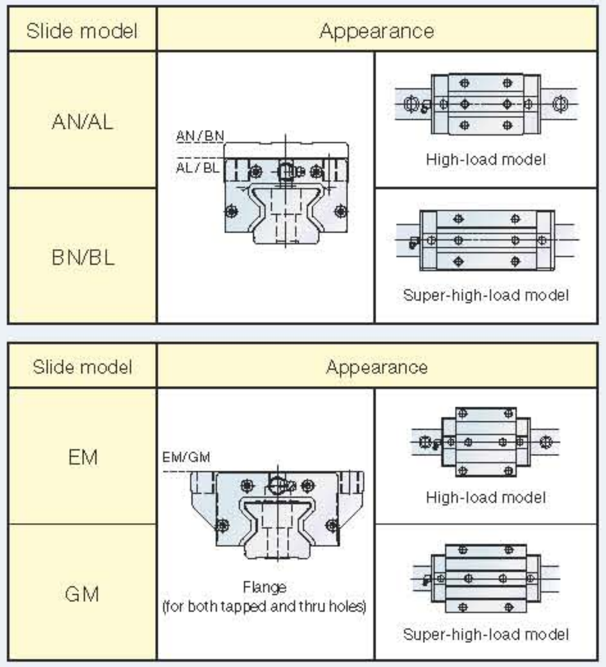

Fig. 2 Roller slide models

The Effects of Hydrogen on Microstructural Change and Surface Originated Flaking in Rolling Contact Fatigue

Hideyuki Uyama, Hiroki Yamada, Hideyuki Hidaka, and Nobuaki Mitamura
Basic Technology Research Center, NSK Ltd.

ABSTRACT

The effects of hydrogen on microstructural change and surface originated flaking in rolling contact fatigue were investigated using JIS-SUJ2 bearing steel specimens charged with hydrogen. Under clean lubrication conditions, subsurface originated flaking occurred and the rolling contact fatigue life was reduced and the amounts of the microstructural change called white structure that formed in the specimens increased as the hydrogen content increased. The localized microstructural changes were found in the hydrogen-charged specimens by electron microscope observations. It is supposed that the localization of plasticity was enhanced by hydrogen during the process of rolling contact fatigue. Under contaminated lubrication conditions, which included debris in the lubricating oil, surface originated flaking occurred and the rolling contact fatigue life of the hydrogen-charged specimens became shorter than the uncharged specimens, although white structure was not observed around the flaking. Enhancement of fatigue crack formations due to hydrogen was observed in specimens with artificial dents. It is presumed that hydrogen facilitated the formation of fatigue cracks on the raceway surface.

Reprinted with permission from Japanese Society of Tribologists, Tribology Online, Volume 6, Number 2, Pages 123–132, Year 2011.

1. Introduction

In response to global energy and environmental problems, hydrogen is being developed as a potential new carrier of clean and sustainable energy. One example is the development of the hydrogen fuel cell system. In the hydrogen fuel cell systems, many metallic components are exposed to an environment rich in hydrogen. It is known that the hydrogen can diffuse into the metallic components and cause degradation of their mechanical properties. Therefore, to fully utilize hydrogen as energy carrier, it is important to study the effect of hydrogen on the mechanical properties of metallic components.

Over a period of many years, there have been numerous studies about the hydrogen degradation of mechanical properties. This phenomenon is called hydrogen embrittlement, and many models about the mechanism have been proposed[1–8]. Some of them suggest that hydrogen embrittlement is not due to brittle fracture[2, 6–8], for example, Birnbaum and Sofronis[6] showed that hydrogen enhances localized plasticity and Nagumo et al[8]. suggested that hydrogen increases atomic vacancies and causes unstable plasticity.

In the case of rolling contact fatigue, there are some studies that have suggested that hydrogen generated by the decomposition of lubricant or water in the lubricant decreases the rolling contact fatigue life[9–18]. Some of them pointed that hydrogen causes microstructural change called white structure or white etching area (WEA)[15–18]. It suggested that types of lubricant, slip between rolling elements and rings, and static electricity affect hydrogen generation and diffusion into bearing steels.

On the effects of hydrogen gas atmosphere, some studies showed that the rolling contact fatigue life decreases with the formation of the white structure[19, 20].

It is clear that bearing life becomes shorter and white structure is formed due to hydrogen as mentioned above. However, the basic mechanism is not clear, although this phenomenon seems to be concerned with a hydrogen embrittlement mechanism. Therefore, the objective of this study is to understand the basic role of hydrogen in the rolling contact fatigue process.

It is known that the rolling contact fatigue life depends on the lubrication conditions and that the flaking mode due to rolling contact fatigue is mainly classified as either subsurface originated flaking or surface originated flaking[21]. The subsurface originated flaking occurs by stress concentration at a non-metallic inclusion in the steel under clean lubrication condition, which does not include debris in the lubricant. The surface originated flaking initiates around dents on the raceway surface under contaminated lubrication conditions, which includes debris such as iron particles in the lubricant. It is very important to investigate hydrogen effects on the rolling contact fatigue process under different lubrication conditions, because the flaking mechanism could change. Especially, under contaminated lubrication conditions, which has not been studied before. Therefore, the objective of this study is to understand hydrogen effects on surface originated flaking under contaminated lubrication conditions.

2. Experimental

2.1 Specimens

Flat disk type specimens with a diameter of 65 mm and a thickness of 6 mm were used in the rolling contact fatigue test. The specimens were made of JIS-SUJ2 bearing steel, equivalent to SAE 52100. The specimens were hardened by austenitising at 1 113 K, followed by quenching in oil at 333 K. After hardening, the specimens were tempered at 443 K to produce a final hardness of 740 HV. The surface of specimens was ground and then lapped to produce a polished surface.

2.2 Charge with hydrogen

Before rolling contact fatigue testing, the specimens were charged with hydrogen by immersing them in NH_4SCN aqueous solution at 323 K for 24 h. Three solutions with different concentrations were used to charge the specimens with different amounts of hydrogen. After charging with hydrogen and prior to rolling contact fatigue testing, the specimens were kept cold using dry ice to prevent the diffusion of hydrogen. The rolling contact fatigue testing was started less than 2 h after charging with hydrogen.

The surface roughness of the specimens became worse due to the chemical reaction that occurred during charging with hydrogen. The surface roughness of the uncharged specimen was about 0.01 μm Ra, and that of the hydrogen-charged specimen was about 0.05 μm Ra.

2.3 Measurement of hydrogen content in steel

Using the thermal desorption analysis (TDA) with a mass spectrometer, the measurement of the hydrogen content of some of the specimens after charging with hydrogen was carried out. Sections cut from these specimens were heated in a vacuum chamber in the TDA equipment. The hydrogen was released out of the steel and then detected by the mass spectrometer. It was expected that the hydrogen content in the specimens would decrease with time after charging with hydrogen and during the fatigue testing because hydrogen can diffuse in steel even at around room temperature. Therefore, hydrogen measurements of several specimens kept at 313 K for different durations were carried out. This temperature is almost the same temperature at which the fatigue testing was carried out.

2.4 Rolling contact fatigue testing under clean lubrication conditions

Thrust bearing test machines were used for rolling contact fatigue testing under clean lubrication conditions. Figure 1 shows a schematic of the test machine. The upper race was a 51305 thrust bearing ring and the lower race was the specimen mentioned above. The rolling elements were 6 balls with a diameter of 9.525 mm. The retainer used was made of brass. The lubricating oil used was ISO-VG68, which did not contain debris. The maximum contact pressure was 3.8 GPa and the rotating speed was 1 000 rpm. The film parameter Λ was about 3.4, which was calculated using the minimum film thickness determined by the Dowson-Higginson equation and the surface roughness of the hydrogen-charged specimen. A vibration sensor was used to detect flaking occurrence. The rolling

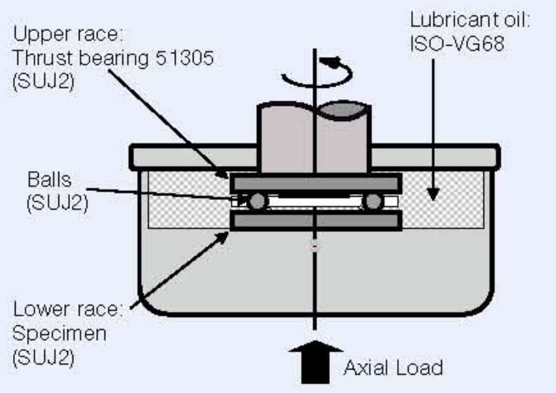

Fig. 1 A schematic of the thrust bearing test machine

contact fatigue test was stopped when the vibration value drastically increased and then the specimen surface was observed by an optical microscope to judge the flaking occurrence.

After the fatigue testing, the microstructure adjacent to the area of flaking on some of the specimens was examined using an optical microscope. The cross sections for the observations were cut out of the specimen as shown in Figure 2. The cross section was polished and lapped followed by etching using picral. In some cases, a scanning electron microscope (SEM) and a transmission electron microscope (TEM) were also used to examine the microstructure. The focused ion beam (FIB) method was used to make thin film samples for TEM observation.

2.5 Rolling contact fatigue testing under contaminated lubrication conditions

The same test machines were used for rolling contact fatigue testing under contaminated lubrication conditions. The lubricating oil was contaminated with particles of high carbon steel with a size of 74–147 μm and a hardness of 870 HV. The fatigue testing was carried out at the maximum contact pressure of 3.1 GPa. The contact pressure was lower than that under the clean lubrication conditions mentioned above because it is expected that the rolling contact fatigue life under contaminated lubrication conditions would be shorter than under clean lubrication conditions. The other test conditions were the same as those used for the clean lubrication conditions.

2.6 Rolling contact fatigue testing using specimens with artificial dents

51305 thrust bearing rings with artificial dents were used as the specimens to observe in detail the formation of fatigue cracks initiated around dents on the raceway surface. The artificial dents were produced using a Rockwell hardness tester with a weight of 588 N. Each specimen had 4 dents made on the raceway surface 90 degree apart. The diameter of the artificial dents was about 300 μm and the depth was about 50 μm as shown in Figure 3. The specimens with the artificial dents were charged with hydrogen using 1 mass% NH_4SCN aqueous solution and used as the lower race in the thrust bearing test machines. The rolling elements were 3 balls with a diameter of 9.525 mm. The lubricating oil used was ISO-VG32, which did not contain debris. The maximum contact pressure was 3.1 GPa and the rotating speed was 1 000 rpm.

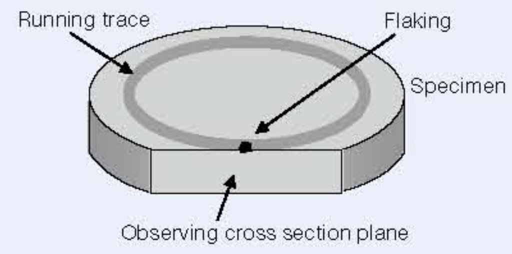

Fig. 2 Observing direction of the microstructure

3. Results and Discussion

3.1 Result of hydrogen content measurement

Figure 4 shows the change of the hydrogen content in the specimen with time after charging with hydrogen. The hydrogen content in the uncharged specimen was about 0.03 mass-ppm. On the other hand, the hydrogen content in the specimen immediately after being charged with hydrogen using a 20 mass% NH_4SCN aqueous solution was about 1.2 mass-ppm. Both of the initial hydrogen contents in the specimens hydrogen-charged using 1 mass% and 0.3 mass% NH_4SCN aqueous solution were about 0.5 mass-ppm. The hydrogen contents in the hydrogen-charged specimens decreased with time after the hydrogen charge because hydrogen diffused out of the steel. Therefore, in this study the hydrogen content in the hydrogen-charged specimens gradually decreased during the rolling contact fatigue testing.

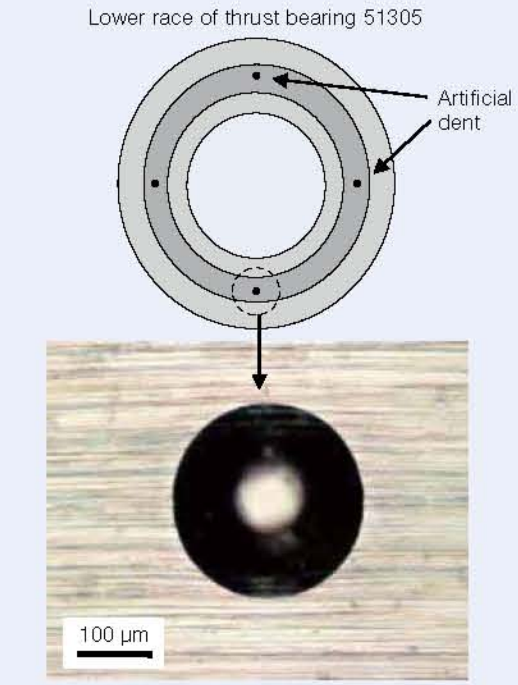

(a) An artificial dent on test specimen surface

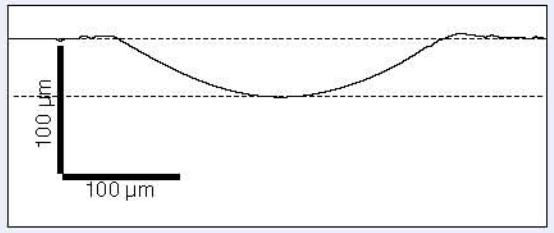

(b) The profile of an artificial dent

Fig. 3 The shape of an artificial dent on the raceway

3.2 Results on rolling contact fatigue tests under clean lubrication condition

Figure 5 shows the results of the rolling contact fatigue tests under the clean lubrication conditions. The horizontal axis shows the life expressed as the number of stress cycles. 1×10^7 cycles corresponds to about 56 h in testing time. Flaking did not occur and the tests were suspended in the uncharged specimens. On the other hand, flaking occurred in most of the hydrogen-charged specimens. It was noticeable that the fatigue life of the specimens that had been hydrogen-charged using the 20 mass% NH_4SCN aqueous solution was much shorter. This was because the hydrogen content in these specimens was higher than in the other specimens as shown in Figure 4. There was no clear difference in the fatigue life of the specimens that were hydrogen-charged using the 1 mass% or 0.3 mass% NH_4SCN aqueous solutions because the hydrogen contents were almost the same in these specimens as shown in Figure 4. It suggests that the rolling contact fatigue life depends on the hydrogen content of the specimen.

Figure 6 (a) shows the microstructure adjacent to the area of flaking in a specimen that was hydrogen-charged using the 20 mass% NH_4SCN aqueous solution. A large amount of the white structure and many fatigue cracks were observed. On the other hand, in the case of the specimens hydrogen-charged using 1 mass% or 0.3 mass% NH_4SCN aqueous solutions, there was either less or no white structure observed in the microstructure adjacent to the area of flaking as shown in Figure 6 (b) and (c). It seems that the amount of the white structure corresponds to the hydrogen content of the specimen.

Figure 7 is the area in Figure 6 (b) magnified by a SEM and shows the white structure, ranging from 2 to 5 μm in width, together with a small crack. A thin film sample was cut out of this area using the FIB method to enable observation by a TEM as shown in Figure 8.

Figure 9 (a) shows the TEM dark field image of the area shown in Figure 7. The black banded area corresponds to the white structure and the thin white line corresponds to the small crack. Figure 9 (b) is the area of the white structure further magnified and shows that the microstructure appears to consist of an ultra-fine grained structure. Figure 9 (c) shows the diffraction pattern of the white structure. It also suggests that the microstructure consist of an ultra-fine grained structure because the diffraction pattern was a circle. Also, it should be noted that the area adjacent to the white structure in Figure 9 (a) was martensite with a lath structure, which is almost the same as the structure of a new specimen before testing. Figure 9 (d) shows the diffraction pattern of the area adjacent to the white structure. It also suggests that this area was martensite with a lath structure because the diffraction pattern consisted of a discrete spot. Therefore

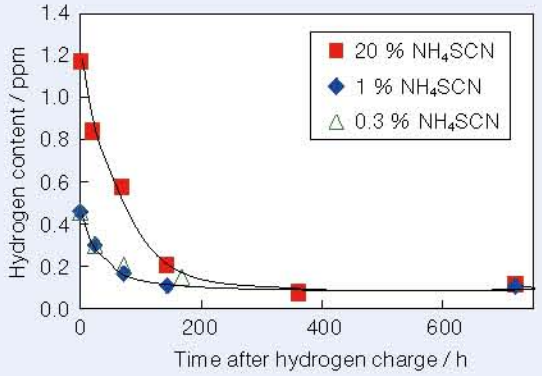

Fig. 4 The variation in hydrogen contents with time after hydrogen charge

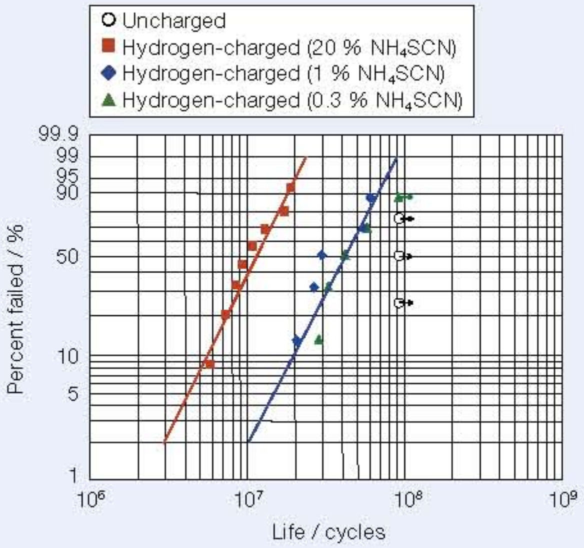

Fig. 5 The results of rolling contact fatigue tests under the clean lubrication conditions

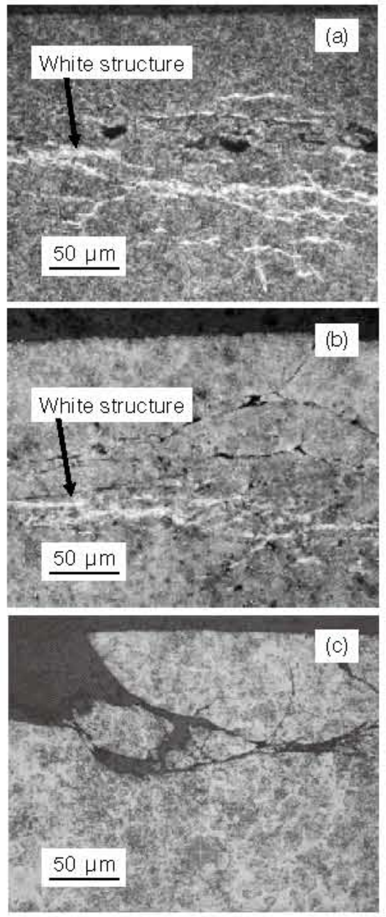

Fig. 6 The microstructure adjacent to the flaking in the hydrogen-charged specimens
(a) 20 mass % NH$_4$SCN, 1.1×10^7 cycles
(b) 1 mass % NH$_4$SCN, 2.8×10^7 cycles
(c) 0.3 mass % NH$_4$SCN, 3.4×10^7 cycles

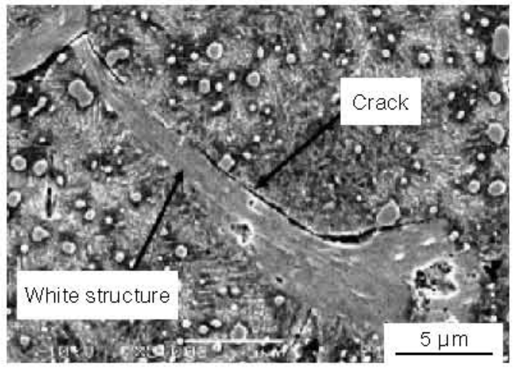

Fig. 7 SEM image of the white structure: magnification of Fig. 6 (b)

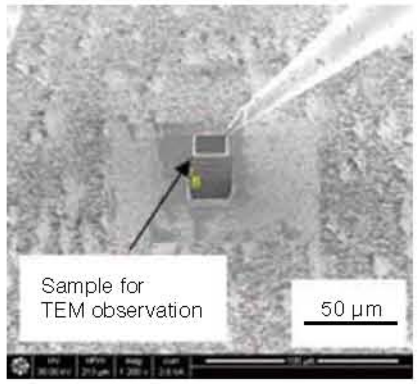

Fig. 8 A sample for TEM observation cut out by FIB method

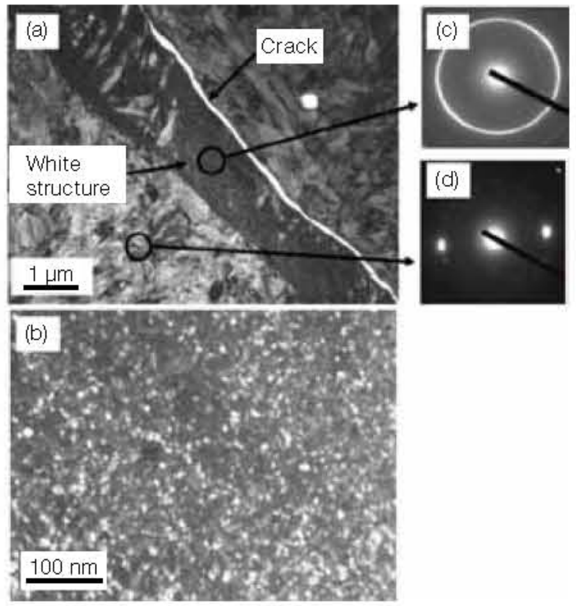

Fig. 9 TEM images of the area including the white structure in Fig. 7
(a) Dark field image of Fig. 7 magnified
(b) Dark field image of the white structure in Fig. 9 (a) magnified
(c) Diffraction pattern of the area of the white structure in Fig. 9 (a)
(d) Diffraction pattern of the area adjacent to the white structure in Fig. 9 (a)

no sign of any microstructural changes were observed in the area adjacent to the white structure. This suggests that the microstructural change due to hydrogen occurred in a localized area several microns in width.

Figure 10 is the area shown in Figure 6 (c) magnified using a SEM. Some small line like microstructural changes were observed although no white structure was observed using an optical microscope. This area of the specimen was also cut out of using the FIB method to be observed by a TEM.

Figure 11 (a) shows the TEM dark field image of the area including the small line like microstructural change shown in Figure 10. A white banded area about 100 nm in width can be seen, which corresponds to the small line structure. The magnified area and the diffraction pattern show that the small line structure consists of an ultra-fine grained structure as shown in Figure 11 (b) and (c). This is the same structure as the white structure shown in Figure 9. Therefore it suggests that the small line like microstructural change represented the early stage in the formation of the white structure. Also in this specimen, the area adjacent to the ultra-fine grained structure had a martensite structure as shown as Figure 11 (d). Therefore, even if the white structure cannot be observed using an optical microscope, highly localized areas of microstructural change up to 100 nm in width can still be present due to hydrogen.

3.3 Discussion on microstructure change

It is reported that microstructural changes can occur during rolling contact fatigue under high temperature and high contact pressure conditions, even in the case where hydrogen has no influence22–24). Therefore, it is necessary to compare this fatigue process with the fatigue process involving hydrogen.

Figure 12 shows the microstructure after rolling contact fatigue testing under high temperature (test temperature: 403 K) and high contact pressure conditions (maximum contact pressure: 5.6 GPa). First, dark etching area was observed in the wide area of high shear stress as shown in Figure 12 (a). This microstructural change is called DEC (dark etched constituent). With further stress cycles, regular and parallel white bands were formed within DEC area as shown in Figure 12 (b). This phenomenon is known as WEC (white etched constituent).

Mitamura et al.24) reported the mechanism of microstructural change under high temperature and high contact pressure conditions using TEM observations. They showed that within DEC martensite laths had changed to a dislocation cell structure due to cyclic plasticity and that WEC had an ultra-fine grained structure, which was formed by further cyclic plasticity. It suggests that in the case of the rolling contact fatigue process without hydrogen, a martensite structure changes to a dislocation cell structure and DEC is observed, which gradually progresses over a wide area and then parts of the dislocation cell structure change to the ultra-fine grained structure and WEC is observed. In other words, the dislocation cell structure must exist widely around the ultra-fine grained structure.

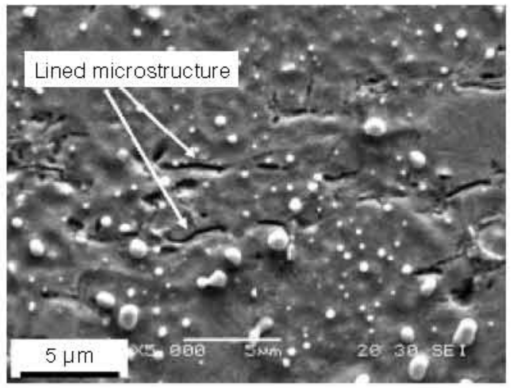

Fig. 10 SEM image of Fig. 6 (c) magnified

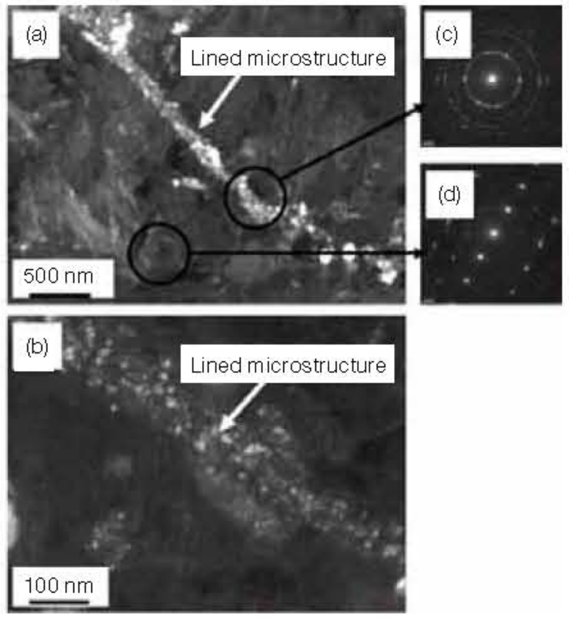

Fig. 11 TEM images of the area including the lined microstructure in Fig. 10
(a) Dark field image of Fig. 10 magnified
(b) Dark field image of the lined microstructure in Fig. 11 (a) magnified
(c) Diffraction pattern of the area of the lined microstructure in Fig. 11 (a)
(d) Diffraction pattern of the area adjacent to the lined microstructure in Fig. 11 (a)

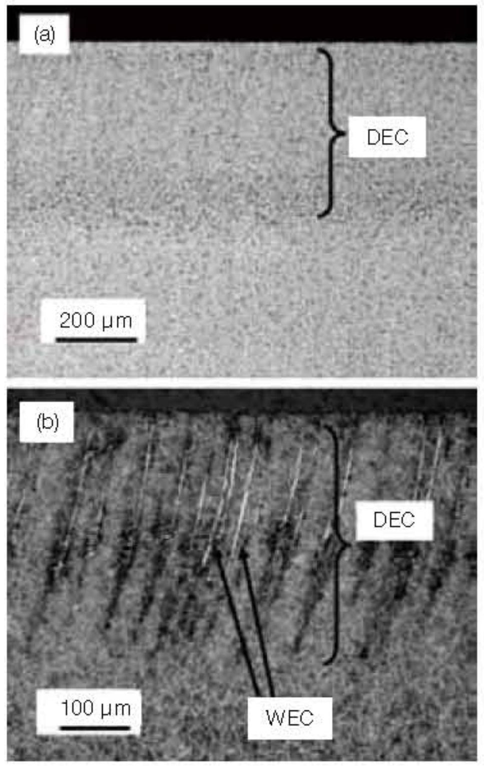

Fig. 12 The microstructural changes after testing under a high temperature (403K) and a high contact pressure condition (5.6GPa)
(a) 4.3×10^6 cycles
(b) 2.3×10^7 cycles

On the other hand, in the hydrogen-charged specimens in this study, the area adjacent to the ultra-fine grained structures were not dislocation cell structures as shown in Figure 9 and Figure 11. Therefore in the case where hydrogen affected the process of rolling contact fatigue, the microstructural changes progress in localized areas and then ultra-fine grained structures are formed there. The microstructural change is caused by cyclic plasticity. It is supposed that hydrogen localizes the plasticity in the rolling contact fatigue process.

It has been reported in studies about delayed fracture[6–8] and tension-compression fatigue fracture[25, 26] that hydrogen localizes plasticity. Therefore, it is presumed that the basic role of hydrogen in the rolling contact fatigue process is the same as in the case of both the delayed fracture and the tension-compression fatigue fracture. It is supposed that localization of plasticity accelerates crack formation and propagation as well as microstructural change, which result in a reduction in the rolling contact fatigue life.

3.4 Results on rolling contact fatigue tests under contaminated lubrication conditions

Figure 13 shows the results of the rolling contact fatigue tests in the hydrogen-charged specimens and the uncharged specimens under the contaminated lubrication conditions. The fatigue life of the hydrogen charged specimens was significantly shorter than that of the uncharged specimens.

The flaking in all of the specimens initiated from around dents on the raceway surface as shown in Figure 14. It is supposed that the fatigue cracks initiated at the edge of the dents due to the stress concentration there.

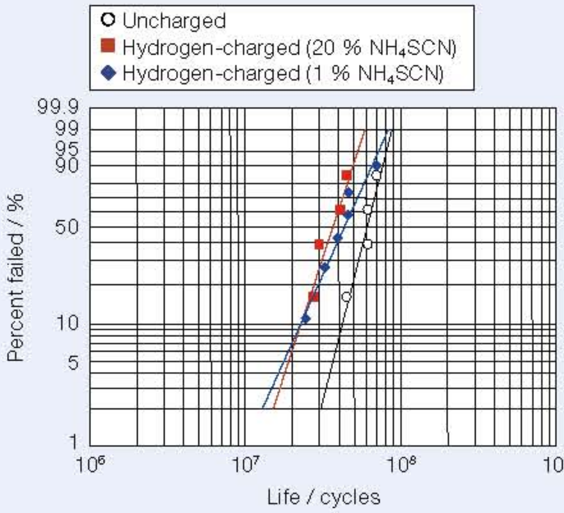

Fig. 13 The results of the rolling contact fatigue tests under the contaminated lubrication conditions

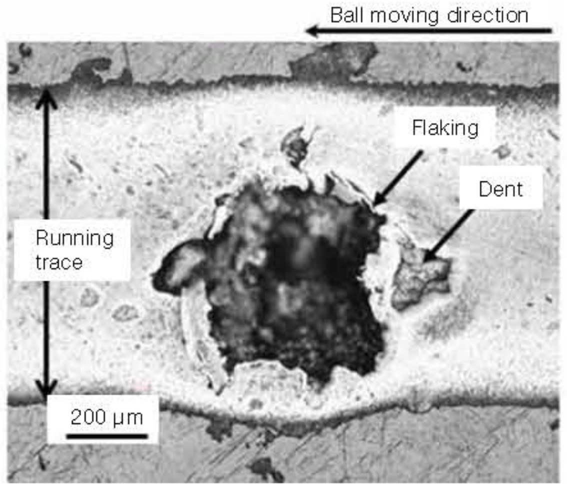

Fig. 14 The flaking on the raceway surface in the hydrogen-charged specimen under the contaminated lubrication conditions
(20 mass % NH_4SCN, 4.2×10^7 cycles)

Figure 15 shows the microstructure around the flaking initiated around a dent in a hydrogen-charged specimen. No microstructural change such as white structure was observed in association with the flaking, although small amounts of white structure were formed about 1 mm away from the flaking area. Namely, in the case of surface originated flaking, the formation of the white structure was not the main cause of the shorter life in the hydrogen-charged specimen.

Figure 16 shows the raceway surface of a hydrogen-charged specimen and an uncharged specimen after testing. It seems that more cracks are observed in the hydrogen-charged specimen. It suggests that the reduction of the fatigue life in the hydrogen-charged specimen under the contaminated lubrication conditions was concerned with crack formations initiated around dents.

3.5 Results on rolling contact fatigue testing using specimens with artificial dents

In order to investigate hydrogen effects on fatigue crack formations around dents on the raceway surface, observations of cracks around the artificial dents were carried out after various testing times. Figure 17 shows the surface and the microstructure of the artificial dent specimen charged with hydrogen after rolling contact fatigue testing. Cracks were found around the edge of the artificial dent as shown in Figure 17 (a) and (b). White structure was not observed around cracks in the artificial dent specimen as shown in Figure 17 (c) and (d).

Figure 18 shows the ratio of the fatigue crack formation around the artificial dents after various testing times in the hydrogen-charged specimen and the uncharged specimen. The ratio of the fatigue crack formation in the vertical axis means the ratio of the number of the artificial dents with fatigue cracks to the number of artificial dents observed after testing. The rolling contact fatigue tests were carried out several times and at scheduled rotational cycles all artificial dents were observed in each test, namely, 8–16 artificial dents were inspected for crack formation to get each plot in Figure 18. It suggests that hydrogen enhanced fatigue crack formations around the artificial dents.

However, it is possible that the change in the surface condition due to the chemical reactions during the charging with hydrogen affected the formation of fatigue cracks and the rolling contact fatigue life. Therefore rolling contact fatigue life tests were carried out using the hydrogen-charged specimen, the uncharged specimen and the aged specimen with the artificial dents. The aged specimens were charged with hydrogen and then kept at room temperature for two weeks, consequently the hydrogen diffused out of the specimen. The initial hydrogen contents of the hydrogen-charged specimen, the

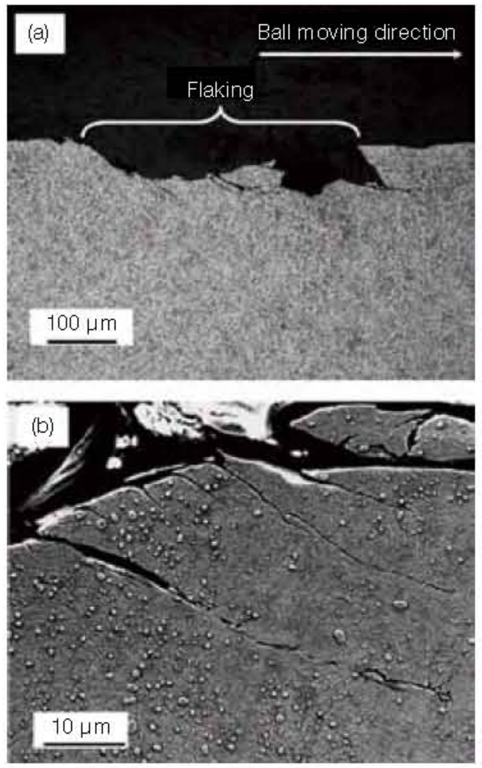

Fig. 15 The microstructure of the hydrogen-charged specimen under the contaminated lubrication conditions
(20 mass % NH_4SCN, 4.2×10^7 cycles)
(a) By an optical microscope
(b) By a SEM

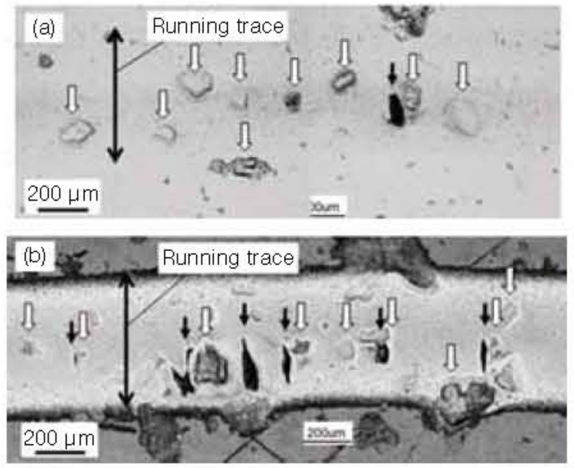

Fig. 16 The raceways after testing under the contaminated lubrication conditions
(a) Uncharged specimen, 6.3×10^7 cycles
(b) Hydrogen-charged specimen, 20 mass % NH_4SCN, 4.6×10^7 cycles
*Black arrows show cracks and white arrows show dents

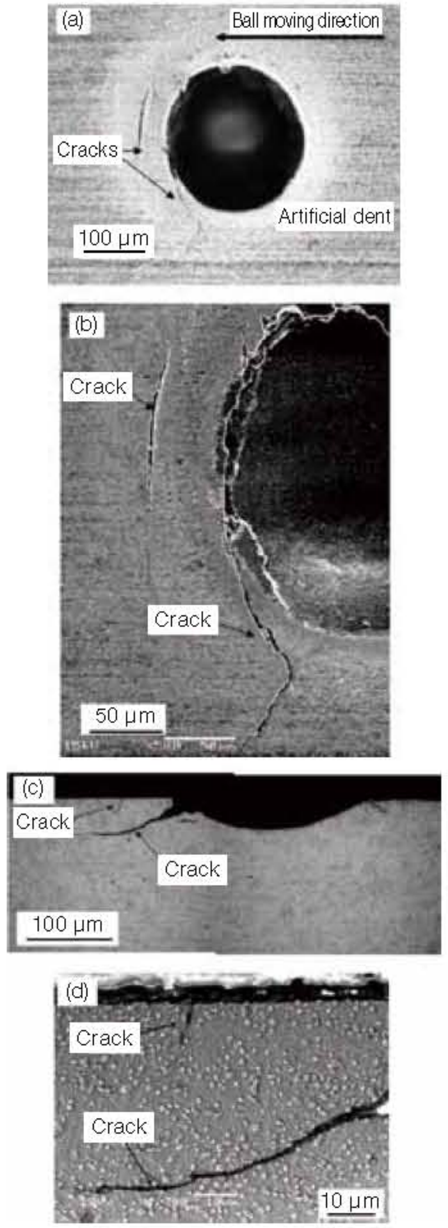

Fig. 17 The artificial dent with cracks after testing (hydrogen-charged specimen, 1.8 × 10^6 cycles)
(a) The surface by a optical microscope
(b) The magnified surface by a SEM
(c) The microstructure by a optical microscope
(d) The magnified microstructure by a SEM

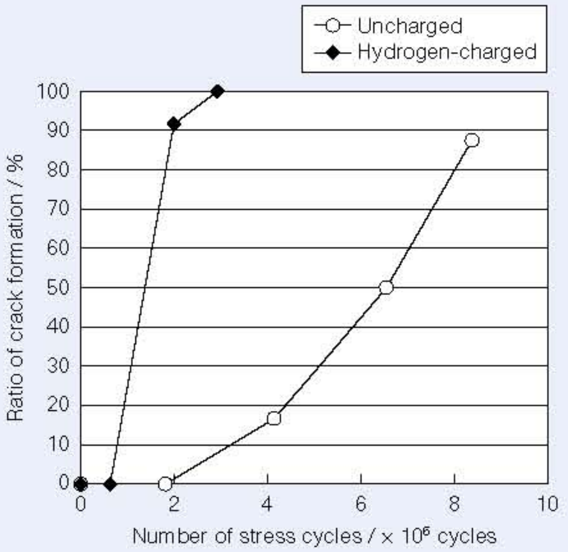

Fig. 18 The ratio of crack formation initiated around the artificial dents

uncharged specimen and the aged specimen were 0.84 mass-ppm, 0.13 mass-ppm and 0.15 mass-ppm respectively when the fatigue tests were started.

Figure 19 shows the results of the fatigue life tests in the hydrogen-charged specimen, the uncharged specimen and the aged specimen. There is no significant difference in the fatigue lives of the uncharged and aged specimens, however, the fatigue life of the hydrogen-charged specimen was significantly shorter. This suggests that the change in the surface condition during charging with hydrogen does not significantly affect the fatigue life. Consequently, it is presumed that the reduction in the rolling contact fatigue life of the hydrogen-charged specimens under the contaminated lubrication conditions was due to the enhancement of fatigue crack formation around dents by hydrogen.

It is reported that hydrogen enhances fatigue crack initiation and propagation in tension-compression fatigue[26], rotating bending fatigue[25] and torsion fatigue[27]. They suggested that these phenomena are due to the localization of plasticity at the fatigue crack tip caused by hydrogen. The present study suggests that the same mechanism can be used to explain the rolling contact fatigue process under contaminated lubrication conditions.

Hydrogen causes different phenomena on two types of rolling contact fatigue mentioned above. Under clean lubrication condition, hydrogen decreased the rolling contact fatigue life due to accelerating the microstructural change in bearing steel. Under contaminated lubrication condition, hydrogen enhanced the fatigue crack formation originated around dents on the specimen surface and decreased the rolling contact fatigue.

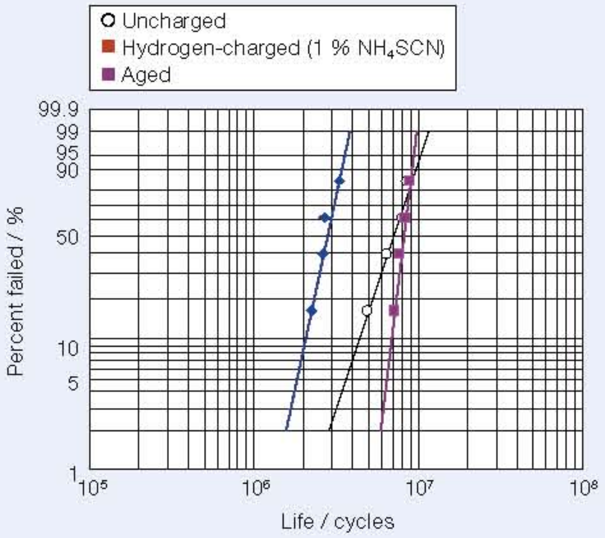

Fig. 19 The results of rolling contact fatigue tests using the specimens with the artificial dents

4. Conclusions

The following conclusions were obtained from the rolling contact fatigue tests and the observation of the microstructure in the hydrogen-charged specimens of bearing steel.

(1) Under clean lubrication condition, subsurface originated flaking occurred and the rolling contact fatigue life of the hydrogen-charged specimens was shorter than the life of the uncharged specimen.
(2) The white structure was formed adjacent to the area of flaking in the hydrogen-charged specimens. TEM observations showed the white structure consisted of an ultra-fine grained structure. However, no microstructural changes were observed in the areas adjacent to the ultra-fine grained structure. This suggests that the localized microstructural changes were caused by hydrogen. Therefore it is supposed that the basic role of hydrogen in the process of rolling contact fatigue is to localize plasticity.
(3) Under contaminated lubrication condition, surface originated flaking occurred and the rolling contact fatigue life of the hydrogen-charged specimen was also reduced. However, white structure was not observed in association with the flaking.
(4) In the rolling contact fatigue testing using the specimens with the artificial dents, the enhancement of fatigue crack formation initiated at the artificial dents occurred in the hydrogen-charged specimen. Therefore it is supposed that hydrogen accelerated fatigue crack formations around dents and decreased the rolling contact fatigue life under contaminated lubricant conditions.

References

1) Troiano, A. R., “The Role of Hydrogen and Other Interstitials in the Mechanical Behavior of Metals,” Transaction of the ASM, 52, 1960, 54–80.
2) Beachem, C. D., “A New Model for Hydrogen Assisted Cracking (Hydrogen “Embrittlement”),” Metallurgical Transactions, 3, February, 1972, 437–451.
3) Oriani, R. A. and Josephic P. H., “Equilibrium Aspects of Hydrogen-Induced Cracking of Steels,” Acta Metal., 22, September, 1974, 1065–1074.
4) Matsui, H. and Kimura, H., “The Effect of Hydrogen on the Mechanical Properties of High Purity Iron. I. Softening and Hardening of High Purity Iron by Hydrogen Charging during Tensile Deformation,” Materials Science and Engineering, 40, 1979, 207–216.
5) Hirth, J. P., “Effects of Hydrogen on the Properties of Iron and Steel,” Metallurgical Transactions, 11A, June, 1980, 861–890.
6) Birnbaum, H. K. and Sofronis, P., “Hydrogen Enhanced Localized Plasticity – a Mechanism for Hydrogen Related Fracture,” Materials Science and Engineering, A176, 1994, 191–202.
7) Lynch, S. P., “Environmentally Assisted Cracking: Overview of Evidence for an Adsorption-Induced Localized-Slip Process,” Acta Metal, 36, 10, 1988, 2639–2661.
8) Nagumo, M., Ishikawa, T., Endoh, T. and Inoue, Y., “Amorphization Associated with Crack Propagation in Hydrogen-Charged Steel,” Scripta Materialia, 49, 2003, 837–842.
9) Ciruna, J. A. and Szieleit, H. J., “The Effect of Hydrogen on the Rolling Contact Fatigue Life of AISI 52100 and 440C Steel Balls,” Wear, 24, 1973, 107–118.
10) Ray, D., Vincent, L., Coquillet, B. and Guirandenq, P., “Hydrogen Embrittlement of a Stainless Ball Bearing Steel,” Wear, 65, 1980, 103–111.
11) Mizuhara, K., Taki, T. and Yamanaka, K., “Anomalous Cracking of Bearing Balls under a Liquid-Butane Environment,” Tribology International, 26, 2, 1993, 135–142.
12) Newlands, C., Olver, A. and Brandon, N., “Gaseous Evolution of Hydrogen from Hydrocarbon Oil and Grease Lubricated Contacts,” Tribology and Interface Engineering Series, 41, 2003, 719–726.
13) Imran, T., Jacobson, B. and Shariff, A., “Quantifying Diffused Hydrogen in AISI-52100 Bearing Steel and in Silver Steel under Tribo-Mechanical Action: Pure Rotating Bending, Sliding-Rotating Bending, Rolling-Rotating Bending and Uni-Axial Tensile Loading,” Wear, 261, 2006, 86–95.
14) Kohara, M., Kawamura, T. and Egami, M., “Study on Mechanism of Hydrogen Generation from Lubricants,” Tribology Transactions, 49, 2006, 53–60.
15) Tamada, K. and Tanaka, H., “Occurrence of Brittle Flaking on Bearings Used for Automotive Electrical Instruments and Auxiliary Devices,” Wear, 199, 1996, 245–252.
16) Kino, N. and Otani, K., “The Influence of Hydrogen on Rolling Contact Fatigue Life and Its Improvement,” JSAE Review, 24, 2003, 289–294.
17) Fujita, S., Mitamura, N. and Murakami, Y., “Research of New Factors Affecting Rolling Contact Fatigue Life,” Proceedings of

WTC 2005, Washington, 2005, 63400.
18) Iso, K., Yokouchi, A. and Takemura, H., “Research Work for Clarifying the Mechanism of White Structure Flaking and Extending the Life of Bearings,” SAE Technical Paper Series, 2005–01–1868, 2005, 1–11.
19) Matsumoto, Y., Murakami, Y. and Oohori, M., “Rolling Contact Fatigue under Water-Infiltrated Lubrication,” Proceedings of 6th International Symposium on Bearing Steels, Phoenix, Bearing Steel Technology, ASTM STP 1419, 2002, 226–243.
20) Endo, T., Dong, D., Imai, Y. and Yamamoto, Y., “Study on Rolling Contact Fatigue in Hydrogen Atmosphere – Improvement of Rolling Contact Fatigue Life by Formation of Surface Film,” Tribology and Interface Engineering Series, 48, 2005, 343–350.
21) Furumura, K., Murakami, Y. and Abe, T., “The Development of Bearing Steels for Long Life Rolling Bearings under Clean Lubrication and Contaminated Lubrication,” Proceedings of 4th International Symposium on Bearing Steels, San Diego, Creative Use of Bearing Steels, ASTM STP 1195, 1993, 199–210.
22) Swahn, H. and Vingsbo, O., “Martensite Decay During Rolling Contact Fatigue in Ball Bearings,” Metallurgical Transactions, 7A, August, 1976, 1099–1110.
23) Osterlund, R. and Vingsbo, O., “Phase Changes in Fatigued Ball Bearings,” Metallurgical Transactions, 11A, May, 1980, 701–707.
24) Mitamura, N., Hidaka, H. and Takaki, S., “Microstructural Development in Bearing Steel during Rolling Contact Fatigue,” Material Science Forum, 539–543, 2007, 4255–4260.
25) Uyama, H., Nakashima, M., Morishige, K., Mine, Y. and Murakami, Y., “Effects of Hydrogen Charge on Microscopic Fatigue Behaviour of Annealed Carbon Steels,” Fatigue and Fracture of Engineering Materials and Structures, 29, 12, 2006, 1066–1074.
26) Murakami, Y., Kanezaki, T., Mine, Y. and Matsuoka, S., “Hydrogen Embrittlement Mechanism in Fatigue of Austenitic Stainless Steels,” Metallurgical and Materials Transactions, 39A, June, 2008, 1327–1339.
27) Fujita, S., Matsuoka, S., Murakami, Y. and Marquis, G., “Effect of Hydrogen on Mode II Fatigue Crack Behavior of Tempered Bearing Steel and Microstructural Changes,” International Journal of Fatigue, 32, 6, 2010, 943–951.

Hideyuki Uyama

Hiroki Yamada

Hideyuki Hidaka

Nobuaki Mitamura

Efficiency Improvement in Half-Toroidal CVTs

Norihisa Kobayashi, Nagao Dohi, Hiroki Nishii, Toshirou Toyoda, Sachiko Noji
NSK Ltd.

ABSTRACT

There has been strong social demand for fuel economy enhancement. One possible solution is to improve the efficiency of half-toroidal continuously variable transmissions (CVTs). An advanced efficiency assessment method will be introduced in this paper. The new method was applied in CVT design optimization. In this new method, the load values used for designing the parts are derived while considering the deformation effect. This optimized design has potential to improve efficiency by up to 1 % over the conventional design without compromising fatigue life.

Translated and reprinted with permission from Society of Automotive Engineers of Japan, Preprinted Paper for Academic Lecture Presentation, No.74–13, (2013).

1. Introduction

Recently, social demand for low-fuel consumption in automobiles has developed out of consideration for the environment and energy savings. Reducing the weight of vehicles is proceeding as a measure to achieve this, and further reduction in the weight of half-toroidal CVTs is a significant technical issue.

Because a half-toroidal CVT transmits power by traction force, it generates a great force inside itself. However, due to reductions in rigidity to further reduce weight, elastic deformation of the supporting members is increasing, and the influence of this deformation on variator efficiency is becoming non-negligible. To respond to this, the authors constructed a new method of efficiency calculation that takes this deformation into account. Furthermore, the application of this highly efficient variator design was investigated. This paper reports these results.

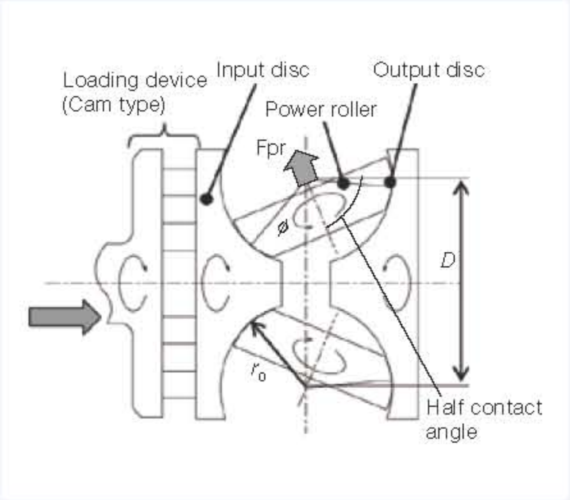

Fig. 1 Structure of a half-toroidal variator

2. Sophistication of the Efficiency Calculation Method

2.1 Loss in the half-toroidal variator

A half-toroidal CVT variator consists of a pair of discs with toroidal forms that face each other and a roller interposed between these discs, also known as a power roller (Figure 1). Power transmission at the contact point of the disc and power roller is conducted because the traction oil solidifies under high pressure. The oil solidifies due to a loading device that exerts a great force on this contact point. In addition, a thrust bearing is located on the back face of the power roller to support the axial component of power roller rotation of the clamping force (power roller thrust force or F_{pr}) at the contact point caused by the half-cone angle.

Loss occurs at the contact point of the disc and power roller within the contact ellipse from slippage in the geometrical normal direction on the contact surface because of the axis of rotation. Combined with the loss in the power roller bearing, this becomes a main factor in half-toroidal variator loss.

2.2 Sophistication of the traction-surface efficiency calculation

Ochiai et al. reported an efficiency calculation method that considers disc deformation and the backward displacement of the power roller using the non-linear finite element method (FEM)[1]. Additionally, they proposed a practical method that limits the variable related to power roller backward displacement to just the amount of power roller swing motion and input disc displacement[2].

However, the deformation of the disc itself tends to increase due to light weight. As shown in Figure 2, in half-toroidal variators for front-wheel, front-drive (FF) vehicles, the output disc moves from elastic deformation of the supporting member due to the reaction force of gears located on the periphery of the output disc. Because of this, the reduction of efficiency calculation accuracy is a problem under the current method.

Oishi et al[3]. proposed a method to investigate the traction-contact position accurately while considering disc deformation, change in half-cone angle by the backward displacement of the power roller, and change in the power roller thrust force. This method was applied to the efficiency calculation program in this study. Although the conventional geometric calculation was carried out using the center of the traction surface of the fixed-member output disc as the coordinate origin, it is possible to perform the calculation while including output disc displacement by replacing the coordinate origin with the initial tilting center. Table 1 shows the comparison of function with the conventional calculation method, and Figure 3 shows the calculation flow.

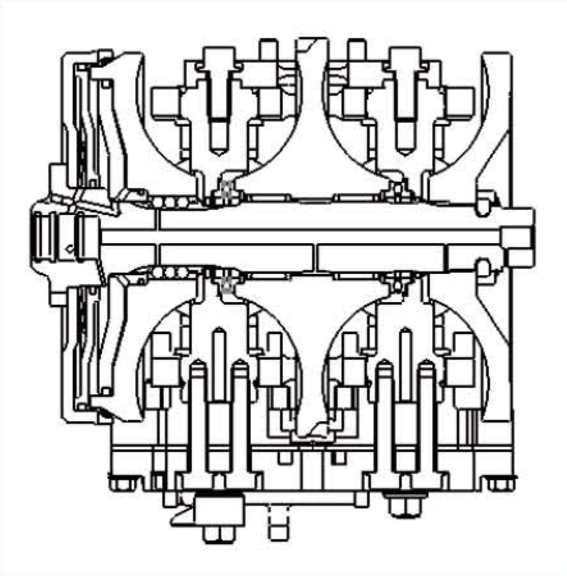

Fig. 2 A half-toroidal variator for FWD vehicles

Table 1

Item	Conventional	Improved
Input disc movement	○	○
Power Roller swing motion	○	○
Deformation of trunnion	○	○
Deformation of discs	–	○
Feedback of Fpr	–	○

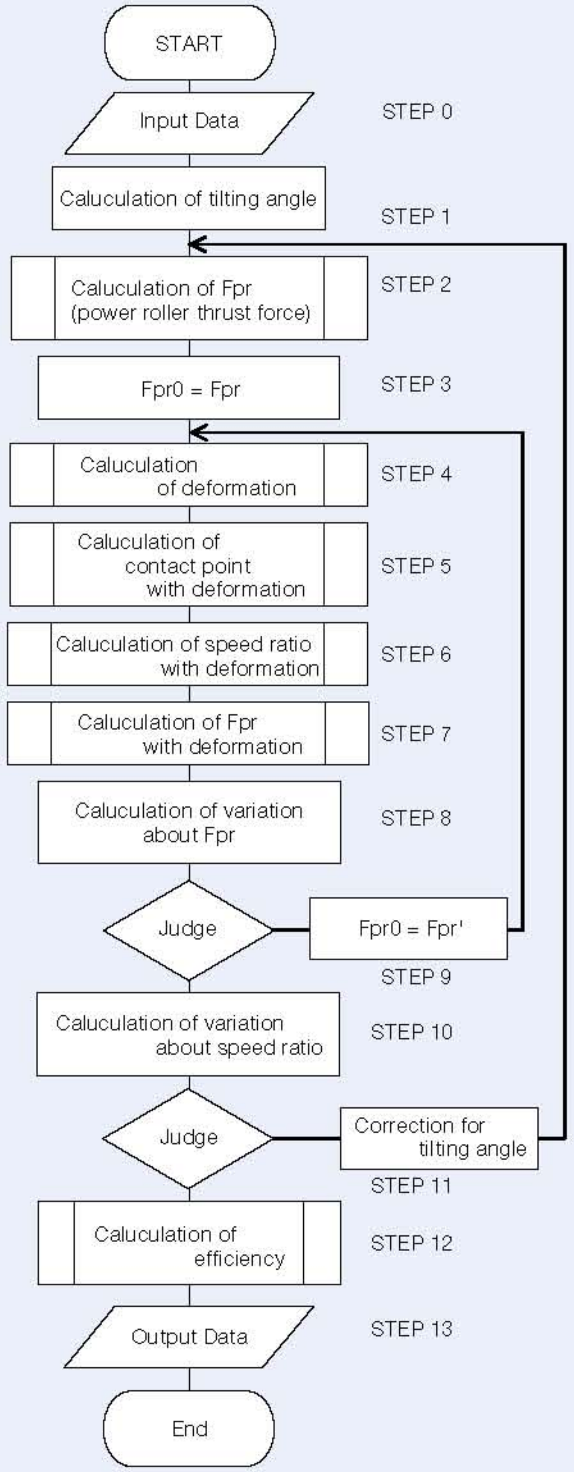

Fig. 3 Calculation flow of the new program

2.3 Sophistication of the power roller bearing efficiency calculation

The influence of variator module deformation on the traction surface has been stated so far, and the influence of trunnion deformation on the power roller bearing is also considered in the new method.

The assembled power roller has a power roller bearing with a Pitch Circle Diameter (*PCD*) that overhangs the support trunnion as shown in Figure 4. When the power roller thrust force acts on the bearing, the load and contact angle acting on each rolling element changes in each phase with the combination of the cross-sectional deformation in Figure 4 and the deformation at section *A-A* in Figure 4. Although their unevenness causes lower life and lower efficiency of the power roller bearing, this can be relieved by adjusting the initial contact angle of the power roller bearing. However, when using a generally simplified, non-linear spring model (in which each rolling element is approximated by non-linear springs), it is difficult to calculate the load on each rolling element while considering trunnion deformation and the contact angle on each rolling element because it is necessary to change the connecting nodal points. Consequently, the calculation must be carried out using non-linear FEM that includes modeling of the rolling elements.

Therefore, the authors of this study divided the model into two phenomena: the displacement of rolling elements and the change of the contact angle and load distribution. The former was calculated by a NSK-developed bearing analysis program[4], and the latter was calculated by linear FEM that is widely prevalent in computer-aided engineering (CAE) so that two tools were used in cooperation for the calculation. This process enabled the designers to calculate the surface pressure on each rolling element while considering the trunnion deformation and variations in the contact angle. Additionally, it became possible to consider the influence of the centrifugal force on the rolling elements by using the bearing analysis program in calculations regarding bearing area.

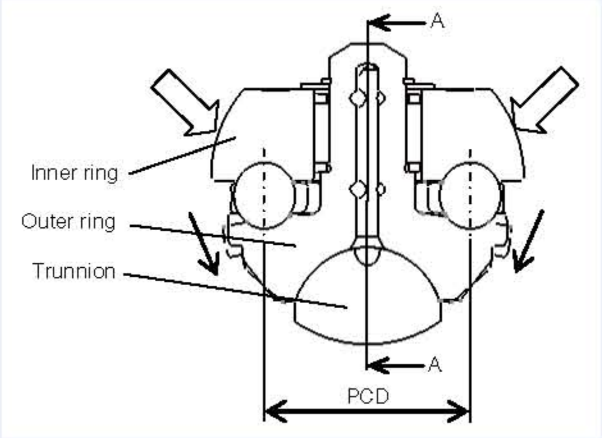

Fig. 4 Cross-Section of an assembly power roller

Figure 5 shows the calculation method. First, the load of the rolling element and contact angle are calculated by a bearing analysis program without considering the deformation. The displacement of each rolling element is analyzed by applying the calculated value to both FEM models of the inner ring and outer ring with the trunnion. The load on and contact angle of each rolling element are calculated again by the bearing analysis program using the displacement of each rolling element as the internal clearance of the rolling element. When variations in the contact angle and the load of each rolling element become less than the threshold value, the calculation is considered to be converged and the calculation ends. Table 2 shows the specifications of the CVT used for the calculation, Table 3 shows the calculation conditions of the bearing, and Figure 6 shows example analysis results.

The inner and outer rings become misaligned and the contact angle of the rolling element changes in phase,

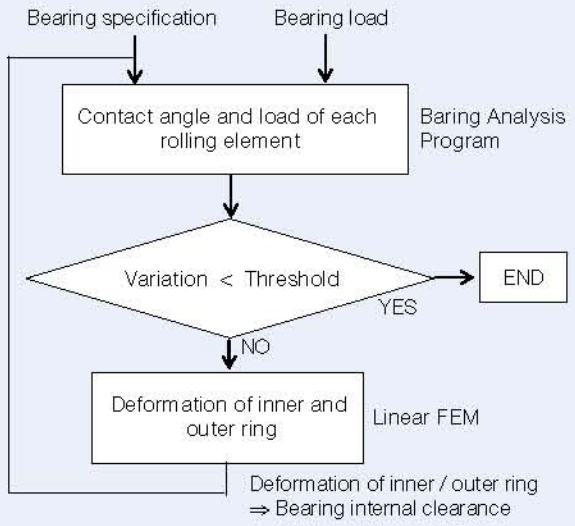

Fig. 5 Calculation flow

Table 2

Cavity diameter	132 mm
Disc radius	40 mm
Half cone angle	62.5 deg
Maximum torque	350 Nm

Table 3

Number of rolling elements	9
Thrust force	16 548 N
Radial force	177 N
Initial contact angle	90 deg
PR rotational speed	3 188 rpm

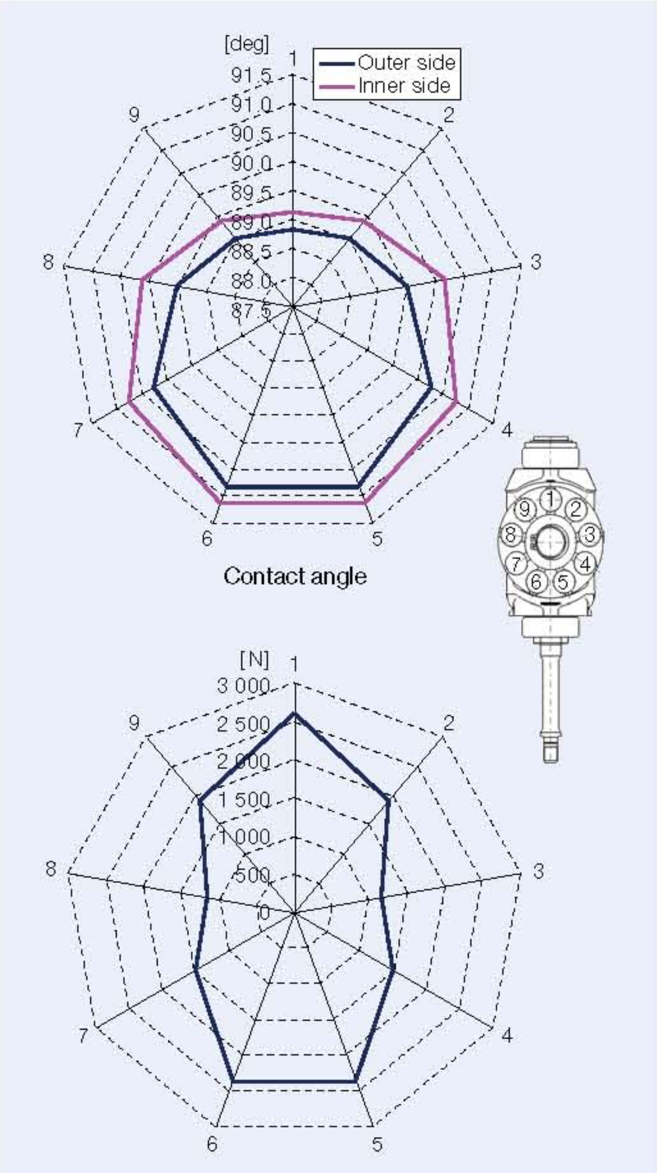

Fig. 6 Contact angle and load of each rolling element

when the traction force, which is the radial force acting in the axis of the tilting direction of the power roller, is applied to the power roller bearing. This phenomenon is confirmed to be repeatable. In addition, the difference in the same rolling element between the contact angle of the inner ring side and the contact angle of the outer ring side due to centrifugal force can be confirmed. Furthermore, the low load ratio of the rolling element of the low-rigidity support member away from the axis can be confirmed.

3. Application to Design of a Highly Efficient Variator

The support member of a power roller is deformed by thrust component force caused by the half-cone angle as stated above, and therefore the power roller moves away from the disc's rotation axis. During this time, the half-cone angle becomes larger, and the contact load on the traction surface and power roller bearing is decreased. It is possible to create a high-efficiency specification of the traction surface and power roller bearing while satisfying the required durability by making a design that considers the contact load with deformation. Table 4 shows the specifications of a base model which was developed by NSK in order to investigate the effects of efficiency improvement in variators.

At first, the surface pressure and efficiency of the base model were calculated. Figure 7 shows the results. This variator efficiency considers only the loss at the traction surface and the loss of the power roller bearing. Due to load reduction by deformation, contact-surface pressure at the traction surface is reduced by approximately 0.36 GPa under maximum underdrive and maximum torque conditions compared with the initial design value.

Table 4

Cavity diameter	124 mm
Disc radius	37.5 mm
PR radius	28.8 mm
Half cone angle	62.5 deg
Maximum torque	380 Nm

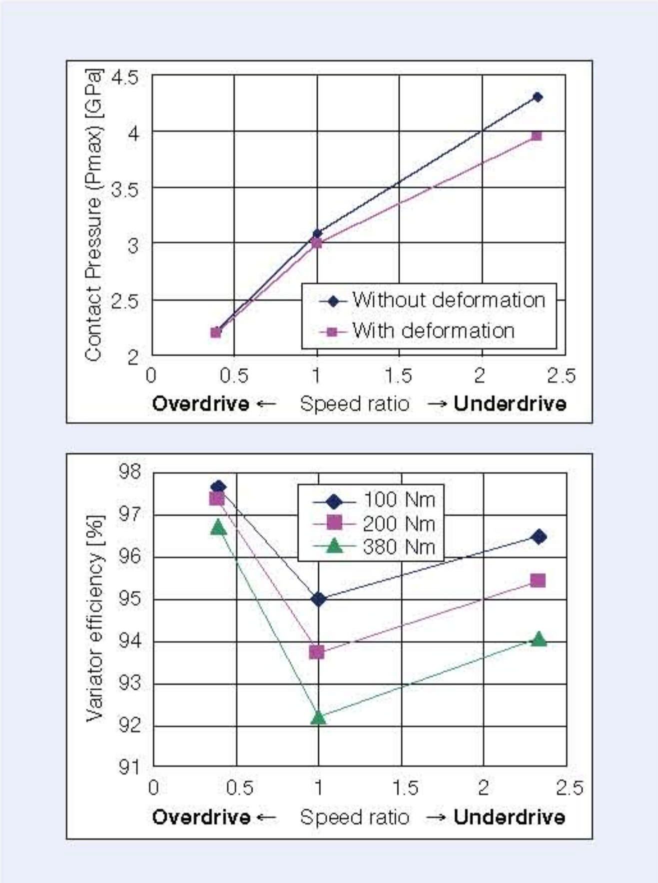

Fig. 7 Contact pressure and variator efficiency

Next, optimization was conducted. The radius of the power roller at the traction surface side was optimized so that the surface pressure in consideration of deformation under maximum underdrive and maximum torque conditions became equal to initial design criteria. The raceway groove radius and initial contact angle of the power roller bearing were also optimized so that the surface pressure of rolling elements became equal to initial surface pressure, and the surface pressure distribution of the raceway was made as uniform as possible. As a result, the radius ratio of the traction surface (power roller traction surface radius / disc traction surface radius) was changed to 92.3 % of the initial value, and the groove radius ratio of the power roller bearing (ball radius / bearing ring radius) was changed to 93.3 % of the initial value. It was possible to modify the model to the low-loss specification.

Figure 8 shows the efficiency improvement after optimization. Efficiency was improved by more than 0.2 % under all speed ratios and torque conditions. Efficiency under a 1:1 speed ratio and maximum torque condition was improved by approximately 1 %.

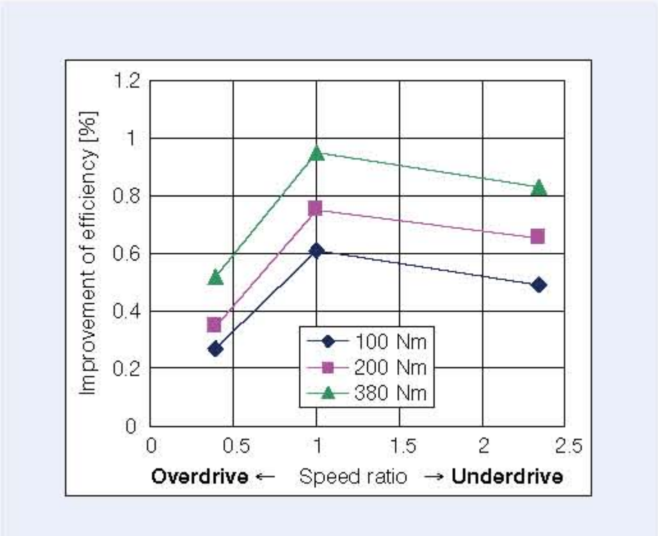

Fig. 8 Improvement of efficiency

4. Conclusion

This paper discussed the new efficiency calculation method for half-toroidal variators and showed the expectation of efficiency improvements by applying these calculations in their design.

The efficiency of variators was calculated by considering the deformation of each part, the load change caused by deformation, and the deformation of trunnions by using the combination of linear FEM and a bearing analysis program.

The efficiency of the variator module designed in consideration of the deformation under load has a potential improvement of up to 1%. Through correlating with actual measured values in the future, NSK will further improve the accuracy of the efficiency calculation method.

References

1) Ochiai et al.: Sophistication of Efficiency Calculation of Toroidal CVT (The second report), Society of Automotive Engineers of Japan, Preprinted Paper for Academic Lecture Presentation, No. 65–03, pp. 9–12 (2003).
2) Ochiai et al.: Sophistication of Efficiency Calculation of Toroidal CVT (The third report), Society of Automotive Engineers of Japan, Preprinted Paper for Academic Lecture Presentation, No. 66–04, pp. 1–4 (2004).
3) Oishi et al.: Development of Wide-Range Half-Toroidal CVT, Society of Automotive Engineers of Japan, Preprinted Paper for Academic Lecture Presentation, No. 26–12, pp. 1–4 (2012).
4) Hirotoshi Aramaki, et al.: Rolling Bearing Analysis Codes "BRAIN"—The Estimation of Rolling Bearing Performance for an Automotive Application, SAE Technical Paper 970586, (1997).

Improvement of Efficiency in Half-Toroidal CVTs

Nagao Dohi, Hiroki Nishii, Norihisa Kobayashi, and Yasunori Oishi
NSK Ltd.

ABSTRACT

In recent years, environmental conservation and energy saving have become concerns all over the world, particularly in the motor vehicle industry, where there is a need to lower fuel consumption. One item to improve on is transmission efficiency, and the use of an engine at optimum operating specifications can help to achieve this improvement. Because of their unique characteristics, half-toroidal continuously variable transmissions (CVTs) are well suited for this purpose. However, in order to obtain these advantages, further efficiency improvement in half-toroidal CVTs is required. This report describes a new method for efficiency improvement, and discusses simulation results and experiment data.

Translated and reprinted with permission from the Society of Automotive Engineers of Japan, Preprinted Paper for Academic Lecture Presentation, No. 66–14, (2014).

1. Introduction

Recently, there has been increased social demand for low-fuel consumption automobiles in order to protect the environment and save energy. In order to achieve optimum operating points that minimize fuel consumption as much as possible, there is a strong trend toward non-stage transmissions, multi-stage automobile transmissions, and wide speed ratio transmissions.

A half-toroidal CVT is a high-response, non-stage transmission mountable on automobiles with large displacement engines. It is already advantageous for operation at optimum points, but further improvement of its efficiency is required to improve fuel consumption. This paper discusses a method for improving the efficiency of half-toroidal CVTs and verified test results.

2. Structure of a Half-Toroidal CVT and Main Loss

2.1 Structure of a half-toroidal CVT

A half-toroidal CVT variator consists of a pair of discs with toroidal forms facing each other and a roller interposed between these discs, known as a power roller (Figure 1–1). Power transmission at the contact point of the disc and power roller occurs through traction oil that solidifies under high pressure. Therefore, a loading device that exerts a great force at the contact point of the disc and power roller is necessary. In addition, a thrust bearing is located at the back face of the power roller to support the axial component of power roller rotation of the clamping force (power roller thrust force or F_{pr}) at the contact point caused by the half-cone angle.

2.2 Main loss in a half-toroidal CVT

Figure 1–2 shows the locations and the rate of main loss in a half-toroidal CVT variator. Main factors of loss are the traction contact area (contact point of disc and power roller) and the power roller bearing.

3. Conventional Methods to Improve Efficiency

Optimizing the specifications of the variator and reducing the clamping force are effective in reducing the main loss that occurs at the contact point of the disc and power roller and the power roller bearing. The following methods have been proposed:

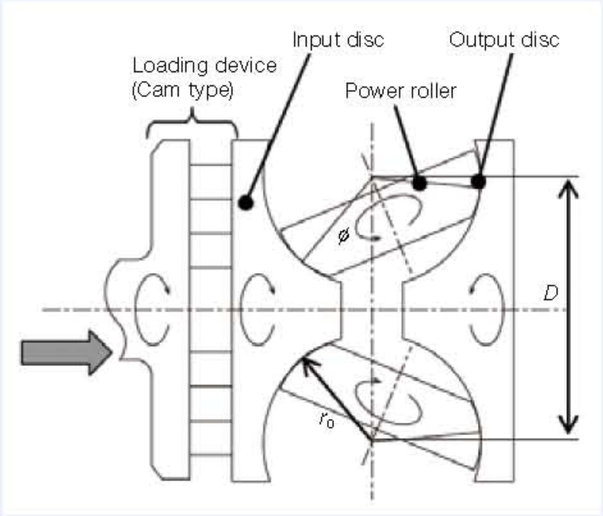

Fig. 1–1 Structure of a half-toroidal variator

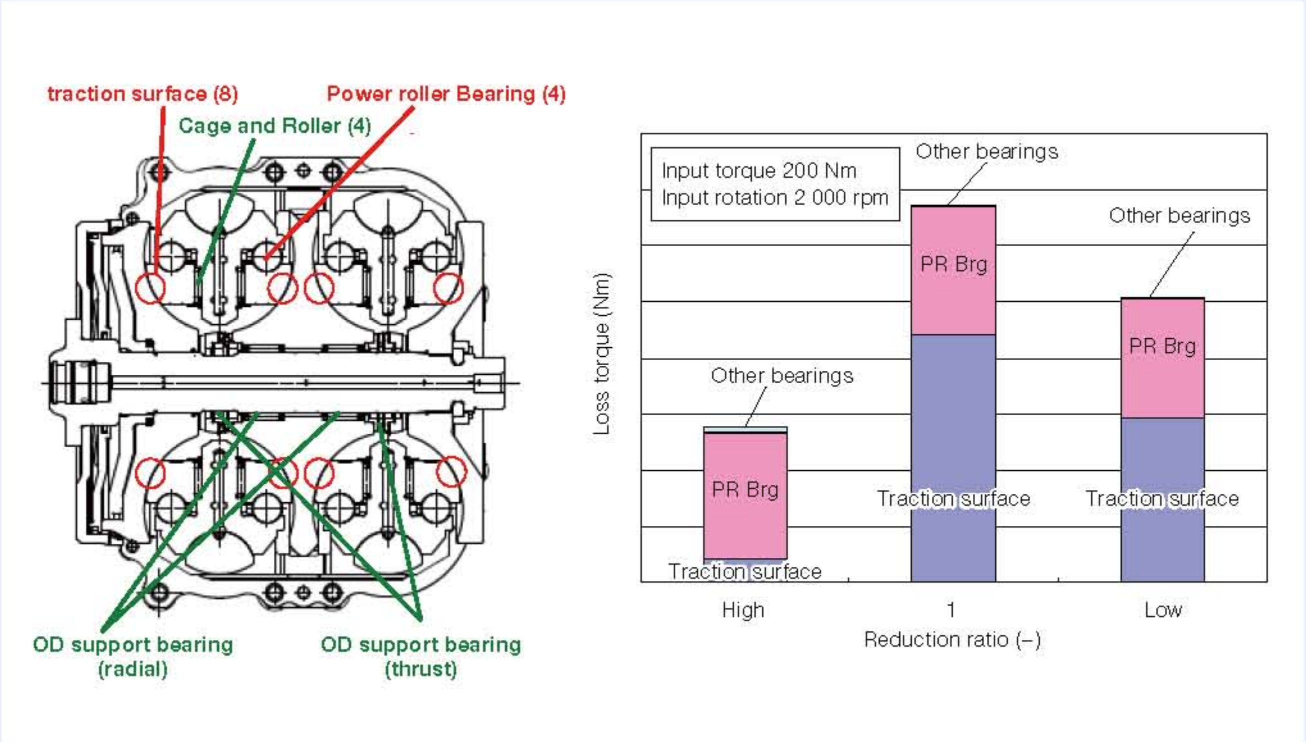

Fig. 1–2 Main loss in a variator

3.1 Reduction of clamping force

When a half-toroidal CVT is used in an actual machine, the coefficient (Driving traction coefficient) with a constant margin for the limiting traction coefficient of oil (as shown in Fig. 2–1) is used to avoid the effects of delay from the loading device and friction, including power roller swing-motion resistance. Therefore, there are two methods for reducing the clamping force: One is to increase the limiting traction coefficient itself, and the other is to reduce the margin anticipated during operation. To this end, development of traction oil that has a higher limiting traction coefficient[1], adoption of a microscopic groove on the traction surface, and adopting a crank trunnion to reduce power roller swing-motion resistance[2] have been reported.

3.2 Optimization of specifications by refining the analysis

Specifications regarding traction surface are decided by the cavity diameter, disc curvature radius, power roller curvature radius, and half-cone angle. Specifications of the power roller bearing are decided by the pitch circle diameter (*PCD*), ball diameter, groove curvature radius, and contact angle. Since these are designed to satisfying the durability requirements, it is effective to improve the durability of each element, to reduce the load of each element, and to improve the calculation accuracy of the actual load considering the deformation of each part. A method to optimize the specification by a sophisticated analysis that estimates the actual load more accurately has been proposed to deal with the above concerns.

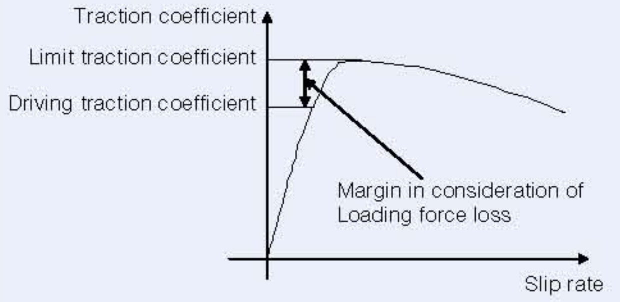

Fig. 2–1 Traction coefficient and slip rate

4. Efficiency Improvement Focused on the Relationship Between Temperature of Contact Point on the Traction Surface and Traction Coefficient

4.1 Relationship between temperature of contact point on traction surface and traction coefficient

For further improvement of variator efficiency, the authors focused on the relationship between the temperature of the contact point on the traction surface and the limiting traction coefficient. Figure 3–1 shows the relationship between the measured temperature of the contact point on the traction surface (surface temperature of the power roller) and the limiting traction coefficient. The limiting traction coefficient and the surface temperature of the power roller are related to each other, and efficiency can be improved because the clamping force can be reduced if the surface temperature can be lowered.

4.2 Relationship between the amount of heat generation in a power roller bearing and on the traction surface and the surface temperature of the power roller

To design the specification while considering the effect of clamping force reduction caused by the reduction of heat generation, it is necessary to accurately estimate the relationship between the amount of heat generation in the power roller bearing, the heat generation on the traction surface, and the surface temperature of the power roller. Therefore, tests regarding power roller surface temperature were carried out by varying the speed ratio so that amount of heat ratio generated in the power roller bearing and on the traction surface differed. The following estimated equation of power roller surface temperature was derived by these test results and calculations regarding amounts of heat generation:

$$\theta_0 = (\theta_{\mathrm{lub}} - 273) + 0.04158\ Q_{brg} + 0.03521\ Q_{contact}$$

θ_0 : Surface temperature of power roller
θ_{lub} : Supply oil temperature
Q_{brg} : Amount of heat generation in the power roller bearing
$Q_{contact}$: Amount of heat generation at the traction surface

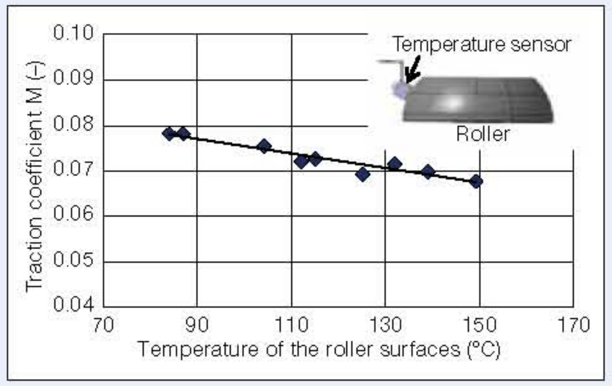

Fig. 3–1 Relationship between temperature of the roller surfaces and traction coefficient

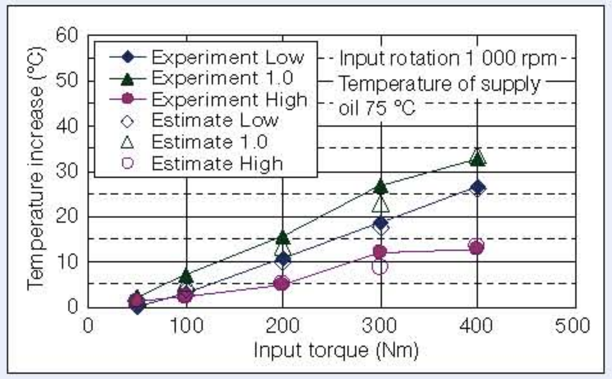

Fig. 4–1 Temperature at traction surfaces

Figure 4–1 shows the comparison between temperature rise estimated by the equation and the measured temperature rise in the experiment. The equation can estimate the temperature of power roller surface almost perfectly.

4.3 The effect of the amount of heat generation at the traction surface and in the power roller bearing on clamping force

Heat generation is reduced by using conventional methods to improve efficiency, such as the reduction of clamping force and the optimization of specifications, and as a result, the temperature of the contact point at the traction surface decreases. Because this increases the limiting traction coefficient, it becomes possible to further reduce the clamping force and then further optimize the specification. These calculations are performed repeatedly in cycles (Figure 4–2). An optimization of specifications that considers these cycles enables improved efficiency.

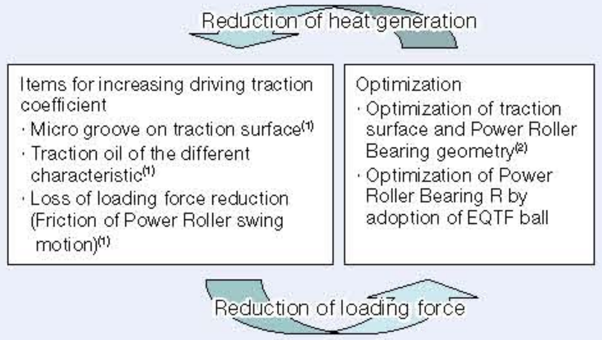

Fig. 4–2 Relationship between reduction of loading force and optimization

5. Examination of Highly Efficient Specifications

5.1 Improved efficiency components

In addition to conventional efficiency improvements[1), 2), 3)], EQTF balls were adopted as the rolling elements of the power roller bearing. An EQTF ball is strengthened by special carbonitriding treatment and can double the bearing life[4)]. If the bearing is designed while considering this extended bearing life, a larger groove radius can be adopted if the ball diameter is made constant, and the amount of heat generation in the power roller bearing can be reduced. Table 5–1 shows the specifications of conventional balls and EQTF balls that enable the same life under the same durability conditions, and Table 5–2 shows the calculated amounts of heat generation. Heat generation in the power roller bearing is lowered by the adoption of EQTF balls.

Table 5–1 Power Roller specification

	Conventional	EQTF ball
Groove radius (mm)	8.044	8.444
Ball diameter (mm)	14.288	14.288

Table 5–2 Power Roller-Brg heat generation

	Power Roller-heat generation (W)		Reduction rate (%)
	Conventional	EQTF ball	
Low	258.237	229.580	11.1
Hight	245.289	219.606	10.5

5.2 Effects of the calculation methods for improving efficiency while considering heat generation

The effects of improved efficiency by adopting efficiency improvements and the method that optimizes specifications while considering heat generation were investigated. Table 5–3 shows the initial variator specification (Start model), and Table 5–4 shows the difference between the Start model and the improved model (Model 1). The Start model has normal steel balls and does not consider the deformation of parts.

Figure 5–1 shows the specific flow of the investigation. The specification of Model 1 is modified from the Start model by adopting efficiency improvements. As stated above, because the temperature at the traction contact point decreases by optimizing the specifications of Model 1, the specification can be optimized again. Thus, the specification of Model 2 is determined. It is then possible to decrease the temperature at the traction contact point by re-optimizing Model 2's specifications in the same way Model 1 was optimized. This loop repeated and the final optimized specification was determined when the temperature decrease at the traction contact point converged. Figure 5–2 shows the estimated temperature at the traction contact point and the rate of increase of the limiting traction coefficient in each loop, Figure 5–3 shows the rate of variator efficiency improvement in each loop, and Table 5–5 shows the optimized final specification. The rate of variator efficiency improvement varies according to the speed ratio of the variator, but efficiency under a 1:1 speed ratio can be improved by 1% or more.

Table 5–3 Start model specification

	Cavity diameter (mm)	Disc radius (mm)	Power Roller radius (mm)	Power Roller Brg (R/Ball diameter) (%)	Half-cone angle (°)	Speed ratio
Start model	124	37.5	28.8	56.3	62.5	2.333–0.364 (6.4)

Table 5–4 Difference between Start model and Model 1

	Start model	Model 1
Loading Force	Without deformation	With deformation
Optimization of geometry	Without deformation	With deformation
Driving traction coefficient	Conventional	With Items
Power Roller - Brg life	Conventional	EQTF ball (200%UP)

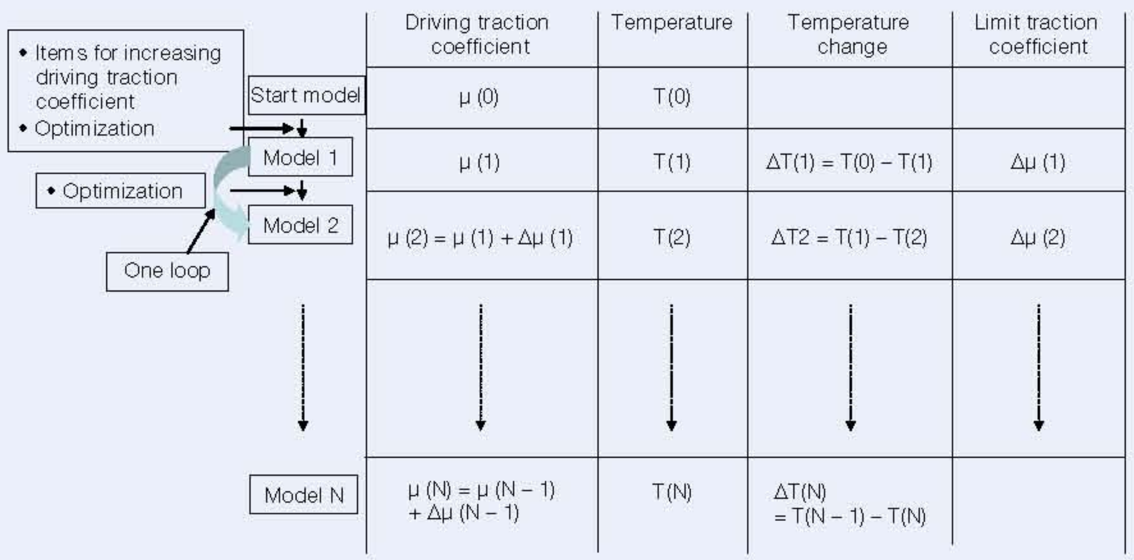

Fig. 5–1 Optimization Flow

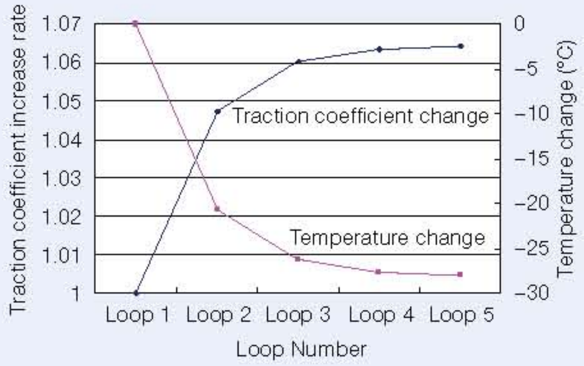

Fig. 5–2 The temperature change and traction coefficient increase in each loop

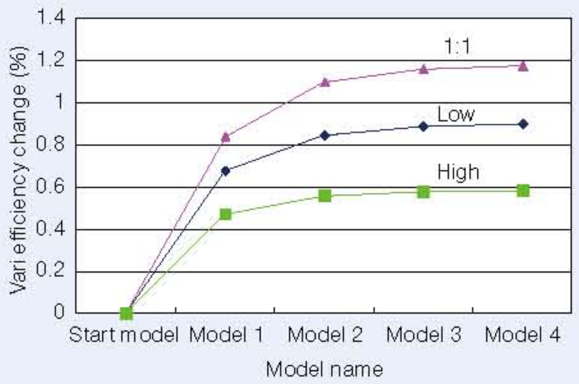

Fig. 5–3 Efficiency Improvement

Table 5–5 Model. N specification

	Cavity diameter (mm)	Disc radius (mm)	Power Roller radius (mm)	Power Roller Brg (R/Ball diameter) (%)	Half-cone angle (°)	Speed ratio
Start model	124	37.5	28.8	56.3	62.5	2.333–0.364 (6.4)
Optimized model	124	37.5	27.79	63.0	62.5	2.333–0.364 (6.4)

6. Verification of Efficiency Improvement Using an Actual Machine

To confirm the validity of the optimization method proposed, a test was carried out using a variator with similar specifications, and the variator was modified by the method in the previous section.

6.1 Simulated efficiency results

The variator efficiency was calculated before and after optimization by the new method. As shown in Table 6–1, calculated efficiency improved by 0.37 % under a high-speed ratio, 1.12 % under a 1:1 speed ratio, and 0.84 % under a low-speed ratio.

6.2 Measured efficiency results

Variator efficiency of both the specifications before and after modification were measured. Table 6–2 shows the test conditions, and Figure 6–1 shows the test results. Measured efficiency of the variator with specifications designed by the new method improved by 0.49% under a high-speed ratio, 1.6% under a 1:1 speed ratio, and 0.8% under a low-speed ratio.

6.3 Comparison of efficiency calculations and measured efficiency results

Table 6–3 shows the summaries of calculated efficiency results and measured efficiency results. The calculated results essentially agree with the measured results under all conditions. In other words, the validity of the new method was confirmed.

Table 6–1 Result of simulation

	Nin (rpm)	Tin (Nm)	Improvement of variator efficiency (%)
High	1 000	100	+ 0.37
1:1	1 000	100	+ 1.12
Low	1 000	100	+ 0.84

Table 6–2 Experiment condition

Ratio	Rev	Input torque	Temperature
High	1 000 rpm	100 Nm 200 Nm 300 Nm	75 °C
1:1			
Low			

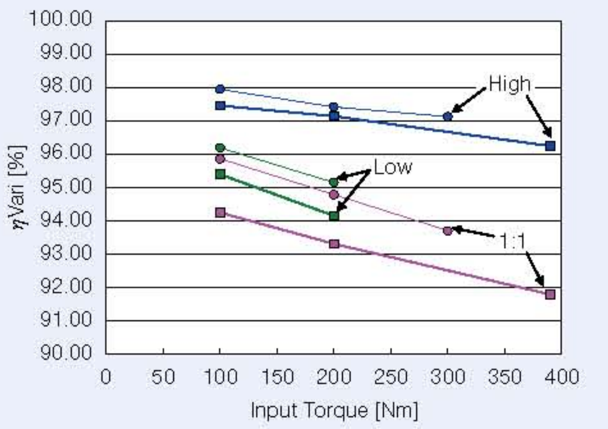

Fig. 6–1 Measured results

Table 6–3 Improvement of variator efficiency (simulation data and experiment data)

	Nin (rpm)	Tin (Nm)	Improvement of variator efficiency (%)	
			Simulation	Experiment
High	1 000	100	+ 0.37 %	+ 0.49 %
1:1	1 000	100	+ 1.12 %	+ 1.60 %
Low	1 000	100	+ 0.84 %	+ 0.80 %

7. Conclusion

A new method focusing on the relationship between the temperature of the contact point on the traction surface and the limiting traction coefficient was proposed for designing high-efficiency variator specifications. Measurements demonstrated that efficiency of the variator designed by the new method improved by 0.49 % under a high-speed ratio, by 1.6 % under a 1:1 speed ratio, and by 0.84 % under a low-speed ratio compared with a conventional variator. The variator achieved an efficiency of approximately 98 % under a high-speed ratio.

References

1) T. Miyaji, Y. Tamoto, H. Koga and H. Hata: Advanced Traction CVT Fluid for Innovating Transmission Technology, Proc. of CVT-HYBRID 2007 Yokohama, JSAE, pp. 73–78 (2007).
2) H. Nishii, S. Noji, T. Inoue: Improvements of half Toroidal CVT, Proc. of CVT-HYBRID 2007 Yokohama, JSAE, pp. 165–170 (2007).
3) Kobayashi et al.: Higher Efficiency of Half-Toroidal CVT, Society of Automotive Engineers of Japan, Preprinted Paper for Academic Lecture Presentation, No. 74–13, pp. 25–28 (2013).
4) Ueda et al.: Longer Life Technology of Rolling Bearings with Improving Anti-Indentation of Rolling Element, Tribology Conference 2008 Spring, Proceedings, (2008), pp. 143–144.

Deep Groove Ball Bearings with a Retainer Plate for Transmissions

In recent years, enhanced transmission efficiency, smaller size, and more lightweight features are increasingly being sought in transmissions as automobiles become more and more fuel-efficient. NSK has developed an integrated deep groove ball bearing with a retainer plate (Photo 1) which allows the whole transmission length to be shortened by the thickness of the plate; in conventional products, the two are separate. The following introduces the developed product's structure and features.

Photo 1 Newly developed deep groove ball bearing with retainer plate

1. Configuration, Structure, Specifications

This product consists of a bearing with a step groove on the outer ring for the snap ring (Figure 1 (a)), a retainer plate with claws along its inner circumference (Figure 1 (b)), and a specially shaped snap ring with protrusions along its circumference (Figure 1 (c)). When the claws of the retainer plate hook over the protrusions on the snap ring inserted into the groove on the outer ring of the bearing, the retainer plate is joined to the outer ring of the bearing to become an unseparable structure (Figure 2).

2. Features

(1) Compact and lightweight transmission

As the whole length of the transmission can be shortened by the thickness of the retainer plate (about 4 mm), the transmission can be made smaller and more lightweight (Figure 3).

(2) Enhanced transmission assembly performance

The retainer plate and outer ring of the bearing are an inseparable structure. It is designed to rotate smoothly as the outer ring of the bearing, thereby facilitating phase adjustments during bolt tightening and allowing for ease of assembly to the transmission (Figure 3).

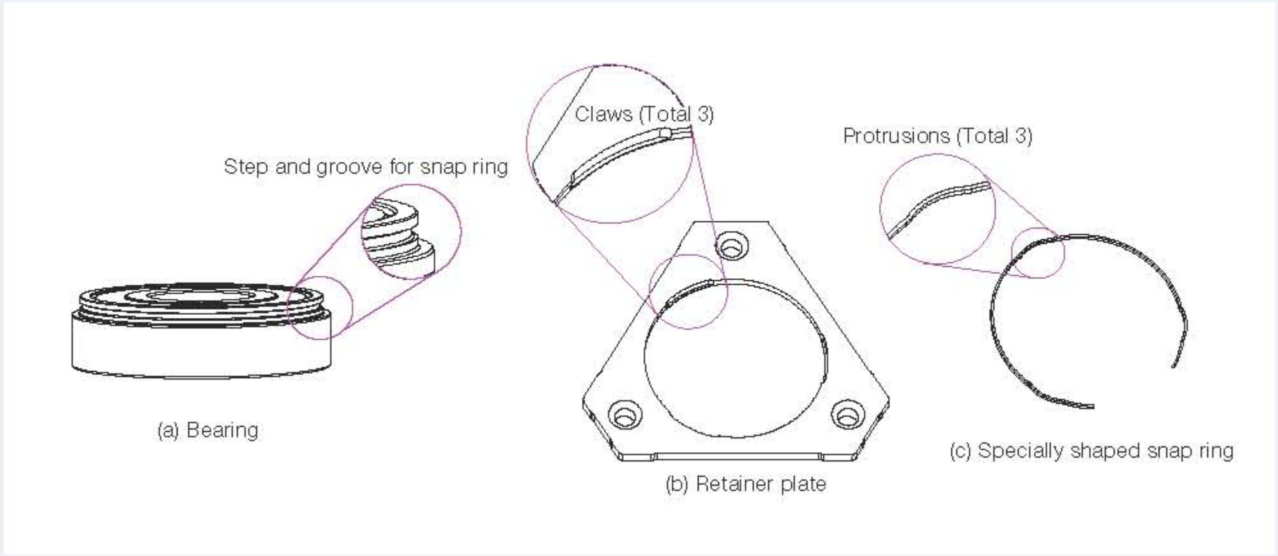

Fig. 1 Bearing with step and groove for snap ring

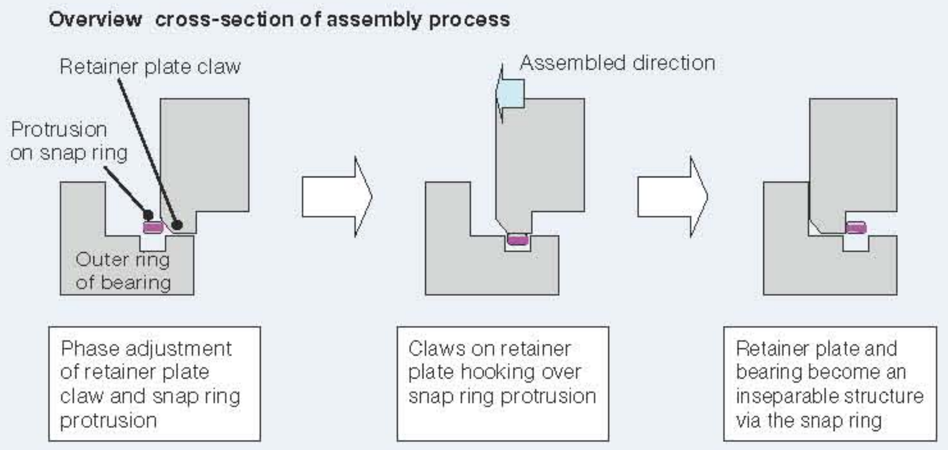

Fig. 2 Assembly process of the retainer plate and bearing

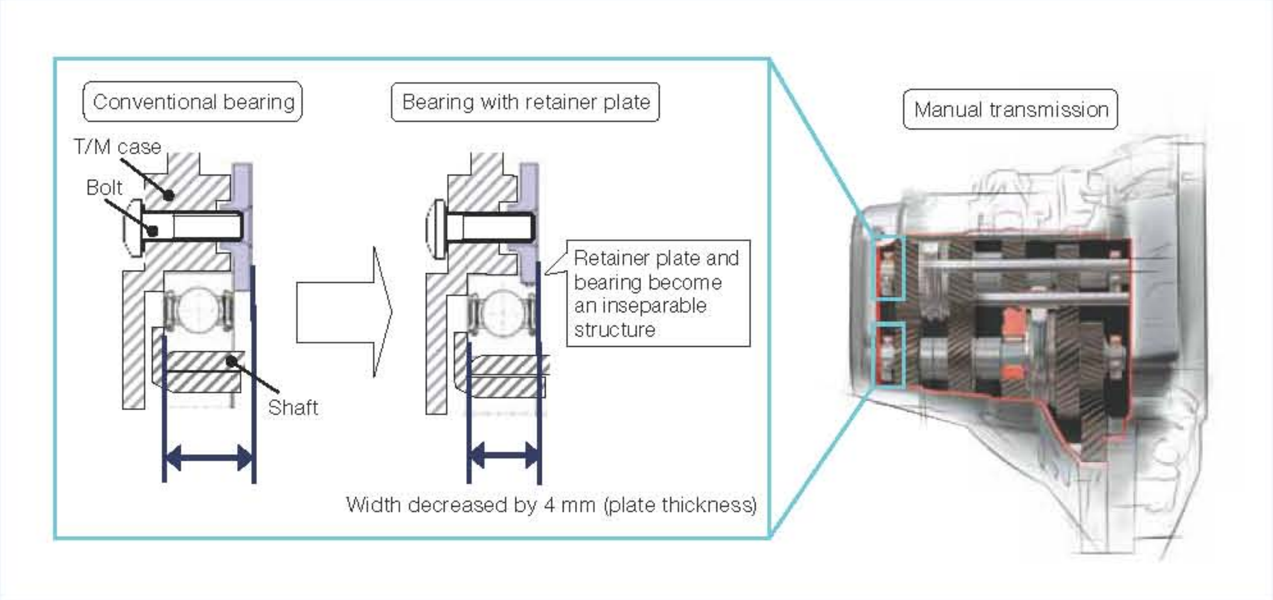

Fig. 3 Features of the newly developed deep groove ball bearing with retainer plate

3. Purpose

Main applications include bearings for automobile transmissions, particularly manual transmissions and dual clutch transmissions (DCTs).

4. Summary

NSK's deep groove ball bearings with a retainer plate contribute to the production of compact and lightweight transmissions. NSK will supply this product from our global production sites, as bearings for manual transmissions and DCTs are in high demand, particularly in Europe and China.

Hub Unit Bearing with High-Performance Sealing and a Nonmagnetic Metallic Cap

The hub unit bearing is located at the center of the automobile wheel. Since it is a necessary component for supporting the automobile body, it must have very strong reliability. In recent years, the improvement of car fuel efficiency has become an urgent task in order to reduce CO_2 emissions to address environmental concerns, cope with rising gasoline prices, and save resources. Subsequently, there is a strong demand for the development of a low friction bearing.

Photo 1 Hub unit bearing with high-performance sealing and a nonmagnetic metallic cap

To ensure reliability of the bearing, contamination in the bearing is prevented by inserting seals on its inboard and outboard sides. However, this leads to increased friction caused by the seals. An alternative method is to insert a metallic cap on the inboard side of the bearing. Since both materials are metal, however, ensuring sufficient sealing performance may be an issue, depending on the environment.

In response, NSK has developed a new hub unit bearing (Photo 1, Figure 1) consisting of a nonmagnetic metallic cap attached to vulcanized rubber to allow for high sealing performance, thereby ensuring both reliability and low friction.

1. Features

(1) Improved reliability in harsh environments

The nonmagnetic metallic cap attached to the vulcanized rubber fitting allows for sealing performance seven times greater than that of conventional metallic caps (Figure 2). This prevents the intrusion of muddy water, snow, sand, and other foreign matter into the bearing.

(2) Compact due to the use of a high-power magnetic encoder

Inserting a nonmagnetic metallic cap between the wheel speed sensor and magnetic encoder increases the air gap (Figure 1) and requires increased magnetic force from the encoder, which leads to. Conventional bearings are typically large because their size is dependent on larger magnetic encorders, which are required to provide sufficient magnetic force. With this new product, the need for a large bearing is eliminated due to the use of a smaller magnetic encoder that has a 20 % higher magnetic force than conventional products (Figure 3).

(3) Reduced friction

Instead of using a seal, the nonmagnetic metallic cap is directly attached to the inboard side of the bearing to ensure zero friction, and a low-friction seal is used on the outbord side.

Successfully achieving low friction and improved sealing performance of the hub bearing reduces the vehicle's overall driving resistance (Figure 4).

2. Summary

Ensuring reliability of both high sealing performance and low friction, NSK's new hub unit bearing with high-performance sealing and a nonmagnetic metallic cap contributes to the reduction of market defects and improved fuel efficiency. We hope to continue our development efforts to expand the use of this bearing in more vehicles, and to improve fuel efficiency while maintaining high reliability.

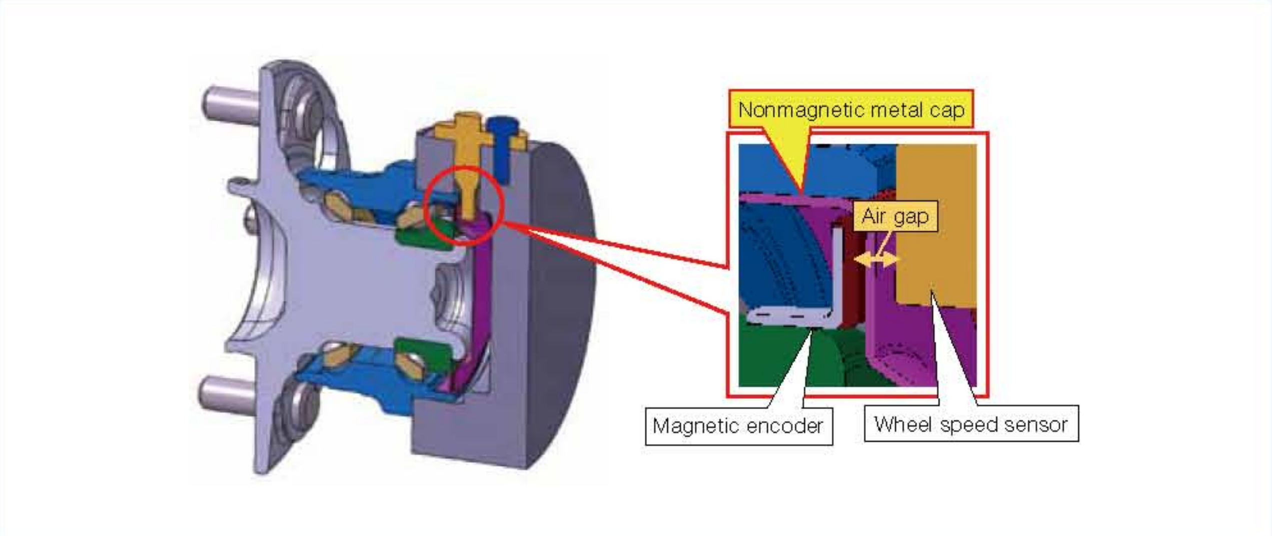

Fig. 1 Structure of nonmagnetic metallic cap

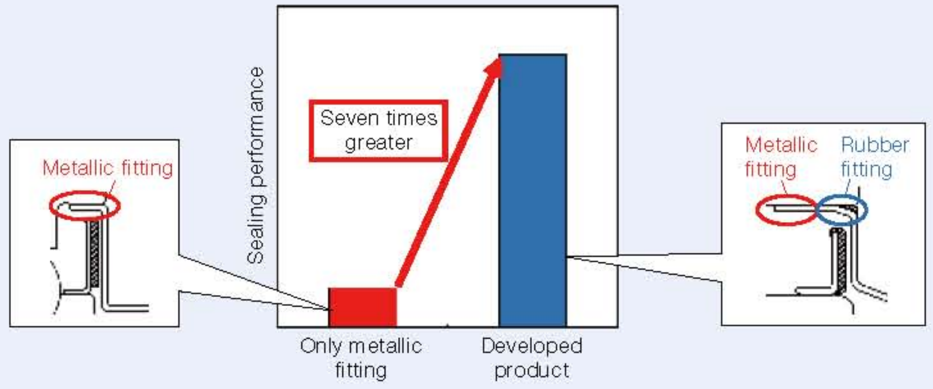

Fig. 2 Sealing performance of hub unit bearings (test results of an air leak test)

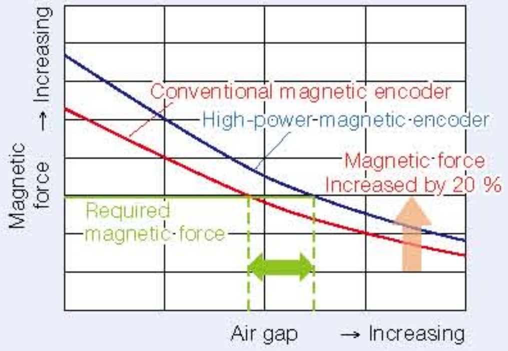

Fig. 3 Use of a high-power magnetic encoder

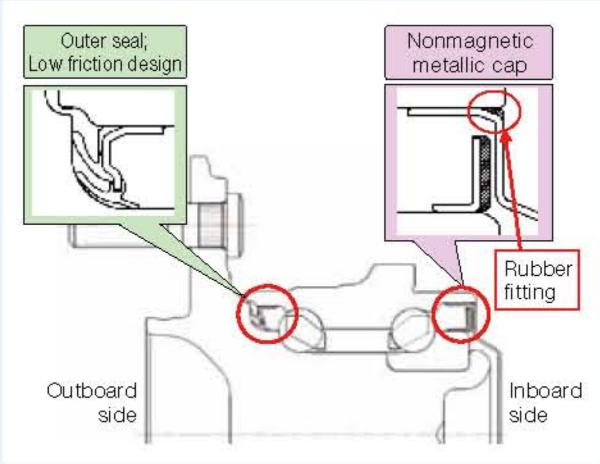

Fig. 4 Cross-sectional view of a hub unit bearing with high-performance sealing and a nonmagnetic metallic cap

Low-Friction Torque Tappet Roller Bearings for Automotive Engines

In recent years, the need for better fuel efficiency in automobiles has increased chiefly because of the growing environmental awareness of consumers. To realize improved fuel efficiency, improvements have been sought in a variety of engine-related technologies. Some advancements include creating compact and lightweight engines by miniaturizing technology, reducing torque loss by the use of low-viscosity engine oil, and adopting new technologies including variable valve timing mechanisms.

Photo 1 Newly developed low-friction torque tappet roller bearing

Reducing the size of bearings used in engines is particularly important as small bearings allow for compact and lightweight engines and may also help to reduce torque loss.

The following introduces low-friction torque tappet roller bearings for automotive engines (Photo 1) developed by NSK. This product has compact and lightweight features due to its long lifespan and contributes to improved automobile fuel efficiency due to reduced torque loss achieved by its compact size.

1. Features

The tappet roller bearing smoothly absorbs the load from the rotary movements of the camshaft of the engine. It is built into the rocker arm, which pushes down the suction and exhaust valves according to the rotary movements of the camshaft. As one locker arm is built into one valve, 16 bearings are used for a 4-cylindered engine (1 cylinder with 4 valves) (Figure 1).

The axis at the weakest part in this bearing has been treated by carbonitriding and induction hardening. While ensuring the tightening performance required by tappet roller bearings, a rolling fatigue life over twice that of same-sized conventional products has been achieved (Figure 2).

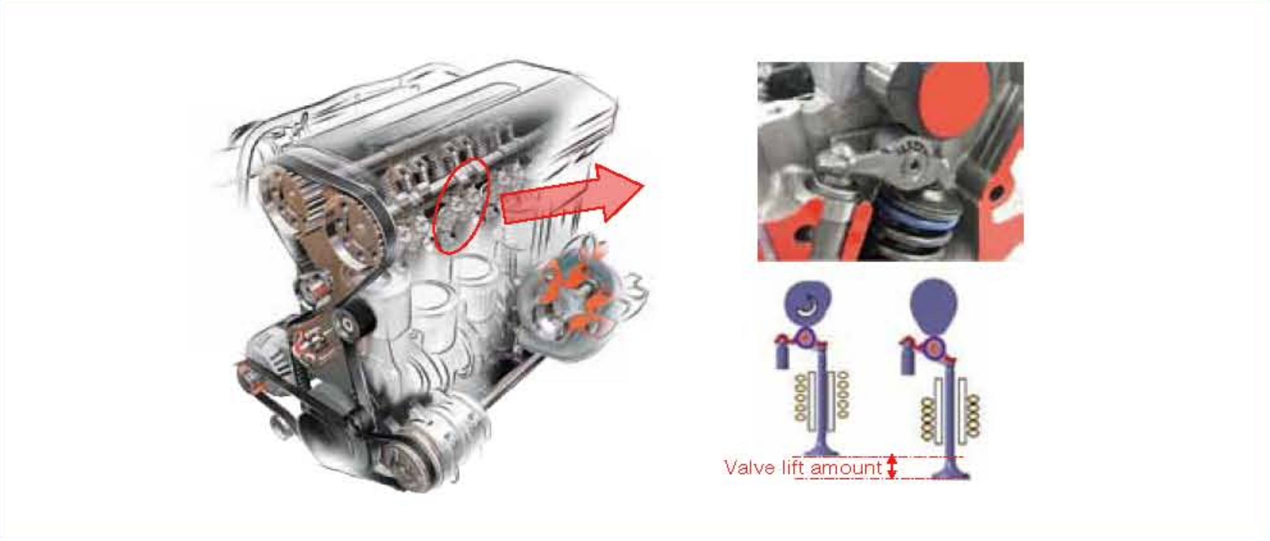

Fig. 1 Cutaway view of engine structure

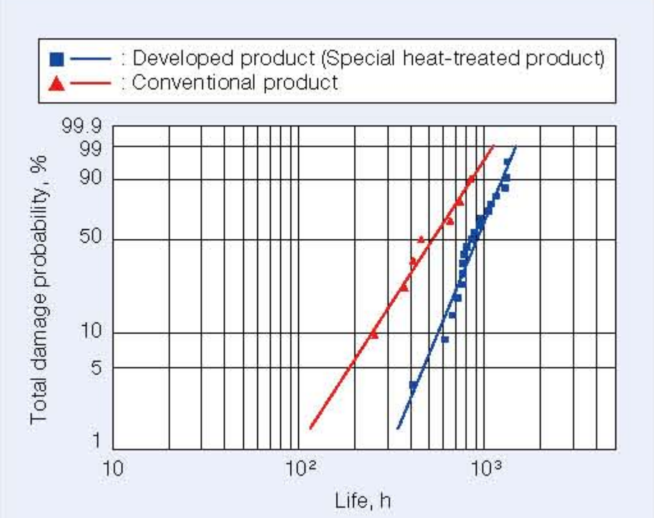

Fig. 2 Comparison of rolling fatigue life between the newly developed product (with special heat treatment) and conventional product

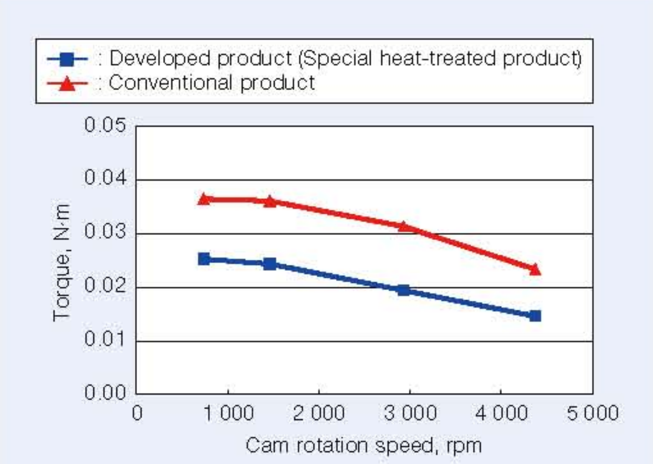

Fig. 4 Comparison of frictional torque between the newly developed product (with special heat treatment) and conventional product

The extended life of the bearing enables its weight and size to be reduced by about 20 % compared with conventional bearings with the same rolling fatigue life (Figure 3).

While the variable valve timing mechanism requires more parts to be used, which leads to a large system structure, this bearing contributes to downsizing the whole system because it is small itself.

The compactness and light weight of the developed product reduce frictional torque of the bearing alone by 30 to 40 % compared to conventional products (Figure 4). Moreover, smooth rotation of the tappet roller also helps reduce friction between camshafts (torque loss). As a result, these features contribute to the improvement of fuel efficiency.

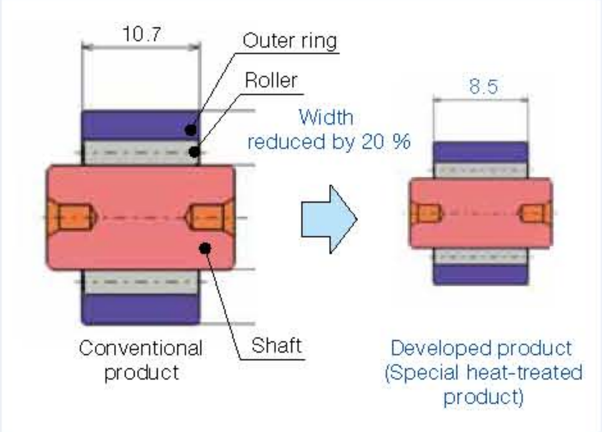

Fig. 3 The developed bearing achieves the same life at a smaller size

2. Applications

- These bearings can be used in variable valve system locker arms such as engine locker arms, timing mechanisms, and so forth.
- They can also be used in roller followers that use a bearing's outer diameter face as a guide face, such as fuel injection pumps.

3. Summary

Low-friction torque tappet roller bearings can further contribute to the realization of fuel-efficient, high performance engines. NSK will continue its efforts to develop new products to meet market needs and improve product performance.

Worldwide Sales Offices

P: Phone F: Fax ☆: Head Office

NSK LTD.-HEADQUARTERS, TOKYO, JAPAN

Nissei Bldg., 1-6-3 Ohsaki, Shinagawa-ku, Tokyo 141-8560, Japan
INDUSTRIAL MACHINERY BUSINESS DIVISION-HEADQUARTERS
P: +81-3-3779-7227 F: +81-3-3779-7644
AUTOMOTIVE BUSINESS DIVISION-HEADQUARTERS
P: +81-3-3779-7189 F: +81-3-3779-7917

●Africa

South Africa:
NSK SOUTH AFRICA (PTY) LTD.
SANDTON 25 Galaxy Avenue, Linbro Business Park, Sandton 2146, South Africa
P: +27-11-458-3600 F: +27-11-458-3608

●Asia and Oceania

Australia:
NSK AUSTRALIA PTY. LTD.
MELBOURNE ☆ 100 Logis Boulevard, Dandenong South, Victoria, 3175, Australia
P: +61-3-9765-4400 F: +61-3-9764-8304
SYDNEY Suite A315, 20 Lexington Drive, Bella Vista, New South Wales, 2153, Australia
P: +61-2-8843-8100 F: +61-2-9893-8406
BRISBANE 1/69 Selhurst Street, Coopers Plains, Queensland 4108, Australia
P: +61-7-3347-2600 F: +61-7-3345-5376
PERTH Unit 1, 71 Tacoma Circuit, Canning Vale, Western Australia 6155, Australia
P: +61-8-9256-5000 F: +61-8-9256-1044

New Zealand:
NSK NEW ZEALAND LTD.
AUCKLAND 3 Te Apunga Place, Mt. Wellington, Auckland 1060, New Zealand
P: +64-9-276-4992 F: +64-9-276-4082

China:
NSK (SHANGHAI) TRADING CO., LTD.
JIANGSU No.8 NSK Rd., Huaqiao Economic Development Zone, Kunshan, Jiangsu, China (215332)
P: +86-512-5796-3000 F: +86-512-5796-3300

NSK (CHINA) INVESTMENT CO., LTD.
JIANGSU ☆ No.8 NSK Rd., Huaqiao Economic Development Zone, Kunshan, Jiangsu, China (215332)
P: +86-512-5796-3000 F: +86-512-5796-3300
BEIJING Room 2116, Beijing Fortune Bldg., 5 Dong San Huan Bei Lu, Chao Yang District, Beijing, China (100004)
P: +86-10-6590-8161 F: +86-10-6590-8166
TIAN JIN Room 06, 09F The Exchange Tower 2, No. 189 NanJing Road, Heping District, Tianjin, China (300050)
P: +86-22-8319-5030 F: +86-22-8319-5033
CHANGCHUN Room 2311, Building A, Zhongyin Building, 727 Xi'an Road, Changchun, Jilin, China (130061)
P: +86-431-8898-8682 F: +86-431-8898-8670
SHENYANG Room 1101, China Resources Building, No. 286 Qingnian Street, Heping District, Shenyang Liaoning, China (110004)
P: +86-24-2334-2868 F: +86-24-2334-2058
DALIAN Room 1805 Xiwang Tower, No.136 Zhongshan Road, Zhongshan District, Dalian, Liaoning, China (116001)
P: +86-411-8800-8168 F: +86-411-8800-8160
NANJING Room A1 22F, Golden Eagle International Plaza, No.89 Hanzhong Road, Nanjing, Jiangsu, China (210029)
P: +86-25-8472-6671 F: +86-25-8472-6687
FUZHOU Room 1801-1811, B1#1A Class Office Building, Wanda Plaza, No.8 Aojiang Road, Fuzhou, China (350009)
P: +86-591-8380-1030 F: +86-591-8380-1225
WUHAN Room 1110, New World International Trade Tower I, No.568 Jianshe Road, Wuhan, Hubei, China (430000)
P: +86-27-8556-9630 F: +86-27-8556-9615
QINGDAO Room 802, Farglory International Plaza, No.26 Xianggang Zhong Road, Shinan District, Qingdao, Shandong, China (266071)
P: +86-532-5568-3877 F: +86-532-5568-3876
GUANGZHOU Room 2302, TaiKoo Hui Tower 1, No.385 Tianhe Road, Tianhe District, Guangzhou, China (510620)
P: +86-20-3817-8800 F: +86-20-3786-4501
CHANGSHA Room 1048, 10/F, Zhongtian Plaza, No.766 WuyiRoad, Changsha, Hunan, China (410005)
P: +86-731-8571-3100 F: +86-731-8571-3255
LUOYANG Room 1108, Fengda Hotel, 6 XiYuan Road, LuoYang HeNan, China (471003)
P: +86-379-6069-6188 F: +86-379-6069-6180
XI'AN Room 1007, B Changan Metropolis Center88 Nanguanzheng Steet, Xi'an, Shanxi, China (710068)
P: +86-29-8765-1896 F: +86-29-8765-1895
CHONGQING Room 2306, Unit B, No.137, Keyuan 2nd Road, Jiulongpo District, Chonqing, China (400039)
P: +86-23-6806-5310 F: +86-23-6806-5292
CHENGDU Room1117, Lippo Tower, No.62 North Kehua Road, Chengdu, Sichuan, China (610041)
P: +86-28-8528-3680 F: +86-28-8528-3690

NSK CHINA SALES CO., LTD.
JIANGSU No.8 NSK Rd., Huaqiao Economic Development Zone, Kunshan, Jiangsu, China (215332)
P: +86-512-5796-3000 F: +86-512-5796-3300

NSK HONG KONG LTD.
HONG KONG ☆ Suite 705, 7th Floor, South Tower, World Finance Centre, Harbour City, T.S.T, Kowloon, Hong Kong, China
P: +852-2739-9933 F: +852-2739-9323
SHENZHEN Room 624-626, 6/F, Kerry Center, Renminnan Road, Shenzhen, Guangdong, China
P: +86-755-25904886 F: +86-755-25904883

Taiwan:
TAIWAN NSK PRECISION CO., LTD.
TAIPEI ☆ 11F., No.87, Song Jiang Rd., Jhongshan District, Taipei City 104, Taiwan
P: +886-2-2509-3305 F: +886-2-2509-1393
TAICHUNG 3F. -2, No. 540, Sec. 3, Taiwan Blvd., Xitun Dist., Taichung City 407, Taiwan
P: +886-4-2708-3393 F: +886-4-2708-3395
TAINAN 5F. No.8, Daye 1st Rd., Southern Taiwan Science Park, Tainan City 741, Taiwan
P: +886-6-505-5861 F: +886-6-505-5061

TAIWAN NSK TECHNOLOGY CO., LTD.
TAIPEI ☆ 11F., No.87, Song Jiang Rd., Jhongshan District, Taipei City 104, Taiwan
P: +886-2-2509-3305 F: +886-2-2509-1393
TAICHUNG 10F-3, No.925, Sec.4, Taiwan Blvd., Xitun Dist., Taichung City 407, Taiwan
P: +886-4-2358-2945 F: +886-4-2358-7682
TAINAN 5F. No.8, Daye 1st Rd., Southern Taiwan Science Park, Tainan City 741, Taiwan
P: +886-6-505-5861 F: +886-6-505-5061

India:
NSK INDIA SALES CO.PVT.LTD.
CHENNAI ☆ 6th Floor, Bannari Amman Towers, No.29 Dr. Radhakrishnan Salai, Mylapore, Chennai-600 004 Tamil Nadu, India
P: +91-44-2847-9600 F: +91-44-2847-9601
GURGAON Unit No-202, 2nd Floor, Block-A, Iris Tech Park, Sector-48, Sohna Road, Gurgaon-122018, Haryana, India
P: +91-124-4104-530 F: +91-124-4104-532
MUMBAI 321, 'A' Wing, Ahura Centre, 82, Mahakali Caves Road, Andheri (East), Mumbai -400 093, India
P: +91-22-2838-7787 F: +91-22-2838-5191

Indonesia:
PT. NSK INDONESIA
JAKARTA Summitmas II, 6th Floor, Jl. Jend Sudirman Kav. 61-62, Jakarta 12190, Indonesia
P: +62-21-252-3458 F: +62-21-252-3223

Korea:
NSK KOREA CO., LTD.
SEOUL Posco Center (West Wing) 9F, 440, Teheran-ro, Gangnam-gu, Seoul, 135-777, Korea
P: +82-2-3287-0300 F: +82-2-3287-0345

Malaysia:
NSK BEARINGS (MALAYSIA) SDN. BHD.
SHAH ALAM ☆ No. 2, Jalan Pemaju, U1/15, Seksyen U1, Hicom Glenmarie Industrial Park, 40150 Shah Alam, Selangor, Malaysia
P: +60-3-7803-8859 F: +60-3-7806-5982
PRAI No.24, Jalan kikik, Taman Inderawasih, 13600 Prai, Penang, Malaysia
P: +60-4-3902275 F: +60-4-3991830
JOHOR BAHRU 88 Jalan Ros Merah 2/17, Taman Johor Jaya, 81100 Johor Bahru, Johor, Malaysia
P: +60-7-3546290 F: +60-7-3546291
IPOH Gr. Floor, 89 Jalan Bendahara, 31650 Ipoh, Perak, Malaysia
P: +60-5-2555000 F: +60-5-2553373

Philippines:
NSK REPRESENTATIVE OFFICE
MANILA 8th Floor The Salcedo Towers 169 H.V. dela Costa St., Salcedo Village Makati City, Philippines 1227
P: +63-2-893-9543 F: +63-2-893-9173

Singapore:
NSK INTERNATIONAL (SINGAPORE) PTE LTD.
SINGAPORE 238A, Thomson Road, #24-01/05, Novena Square Tower A, Singapore 307684
P: +65-6496-8000 F: +65-6250-5845

NSK SINGAPORE (PRIVATE) LTD.
SINGAPORE 238A, Thomson Road, #24-01/05, Novena Square Tower A, Singapore 307684
P: +65-6496-8000 F: +65-6250-5845

Thailand:
NSK BEARINGS (THAILAND) CO.,LTD.
BANGKOK 26 Soi Onnuch 55/1 Pravet Subdistrict, Pravet District, Bangkok 10250, Thailand
P: +66-2320-2555 F: +66-2320-2826

Vietnam:
NSK VIETNAM CO., LTD.
HANOI Techno Center, Room 204-205, Thang Long Industrial Park, Dong Anh District, Hanoi, Vietnam
P: +84-4-3955-0159 F: +84-4-3955-0158

NSK REPRESENTATIVE OFFICE
HO CHI MINH CITY Suite 307, Metropolitan Building, 235 Dong Khoi Street, District 1,HCMC, Vietnam
P: +84-8-3822-7907 F: +84-8-3822-7910

Worldwide Sales Offices

P: Phone F: Fax ☆: Head Office

●Europe

United Kingdom:
NSK EUROPE LTD. (EUROPEAN HEADQUARTERS)
MAIDENHEAD Belmont Place, Belmont Road, Maidenhead, Berkshire SL6 6TB, U.K.
P: +44-1628-509-800 F: +44-1628-509-808

NSK UK LTD.
NEWARK Northern Road, Newark, Nottinghamshire NG24 2JF, U.K.
P: +44-1636-605-123 F: +44-1636-605-000

France:
NSK FRANCE S.A.S.
PARIS Quartier de l'Europe, 2 Rue Georges Guynemer, 78283 Guyancourt, France
P: +33-1-30-57-39-39 F: +33-1-30-57-00-01

Germany:
NSK DEUTSCHLAND GMBH
DUSSELDORF ☆ Harkortstrasse 15, D-40880 Ratingen, Germany
P: +49-2102-4810 F: +49-2102-4812-290
STUTTGART Liebknechtstrasse 33, D-70565 Stuttgart-Vaihingen, Germany
P: +49-711-79082-0 F: +49-711-79082-289
WOLFSBURG Tischlerstrasse 3, D-38440 Wolfsburg, Germany
P: +49-5361-27647-10 F: +49-5361-27647-70

Italy:
NSK ITALIA S.P.A.
MILANO Via Garibaldi 215, Garbagnate Milanese (Milano) 20024, Italy
P: +39-299-5191 F: +39-299-025778

Netherlands:
NSK EUROPEAN DISTRIBUTION CENTRE B.V.
TILBURG De Kroonstraat 38, 5048 AP Tilburg, Netherlands
P: +31-13-4647647 F: +31-13-4647648

Poland:
NSK REPRESENTATIVE OFFICE
WARSAW Ul. Migdalowa 4/73, 02-796, Warsaw, Poland
P: +48-22-645-1525 F: +48-22-645-1529

Russia:
NSK POLSKA SP. Z O.O.
SAINT-PETERSBURG Office I 703, Bldg 29, 18th Line of Vasilievskiy Ostrov, Saint-Petersburg, Russia, 199178
P: +7-812-332-5071 F: +7-812-332-5072

Spain:
NSK SPAIN S.A.
BARCELONA C/Tarragona, 161 Cuerpo Bajo, 2a Planta, 08014, Barcelona, Spain
P: +34-93-289-2763 F: +34-93-433-5776

Turkey:
NSK RULMANLARI ORTA DOGU TIC. LTD. STI.
ISTANBUL 19 Mayis Mah. Ataturk Cad., Ulya Engin Is Merkezi No: 68 Kat. 6, P.K. : 34734, Kozyatagi-Istanbul, Turkey
P: +90-216-477-7111 F: +90-216-477-7174

United Arab Emirates:
NSK BEARINGS GULF TRADING CO.
DUBAI JAFZA View 19, Floor 24 Office LB192402/3, PO Box 262163, DownTown Jebel Ali, Dubai, UAE
P: +971-4-804-8207 F: +971-4-884-7227

●North and South America

United States of America:
NSK AMERICAS, INC. (AMERICAN HEADQUARTERS)
ANN ARBOR 4200 Goss Road, Ann Arbor, Michigan 48105, U.S.A.
P: +1-734-913-7500 F: +1-734-913-7511

NSK CORPORATION
ANN ARBOR 4200 Goss Road, Ann Arbor, Michigan 48105, U.S.A.
P: +1-734-913-7500 F: +1-734-913-7511

NSK PRECISION AMERICA, INC.
FRANKLIN ☆ 3450 Bearing Drive, Franklin, Indiana 46131, U.S.A.
P: +1-317-738-5000 F: +1-317-738-5050
SAN JOSE 780 Montague Expressway, Suite 505, San Jose, California, 95131, U.S.A.
P: +1-408-944-9400 F: +1-408-944-9405

NSK LATIN AMERICA, INC.
MIAMI 3470 NW 82nd Avenue Suite 625, Miami FL 33122, U.S.A.
P: +1-305-477-0605 F: +1-305-477-0377

Canada:
NSK CANADA INC.
TORONTO ☆ 5585 McAdam Road, Mississauga, Ontario, Canada L4Z 1N4
P: +1-905-890-0740 F: +1-800-800-2788
MONTREAL 2150-32E Avenue Lachine, Quebec, Canada H8T 3H7
P: +1-514-633-1220 F: +1-800-800-2788
VANCOUVER 3353 Wayburne Drive, Burnaby, British Columbia, Canada V5G 4L4
P: +1-877-994-6675 F: +1-800-800-2788

Argentina:
NSK ARGENTINA SRL
BUENOS AIRES Garcia del Rio 2477 Piso 7 Oficina "A" (1429) Buenos Aires-Argentina
P: +54-11-4704-5100 F: +54-11-4704-0033

Brazil:
NSK BRASIL LTDA.
SAO PAULO ☆ Rua 13 de Maio, 1633-14th Andar-Bela Vista-CEP 01327-905 São Paulo, SP, Brazil
P: +55-11-3269-4786 F: +55-11-3269-4720
BELO HORIZONTE Rua Ceara 1431-4th andar-sala 405-Funcionarios Belo Horizonte-MG, Brazil 30150-311
P: +55-31-3274-2591 F: +55-31-3273-4408
JOINVILLE Rua Blumenau, 178-sala 910-Centro Joinville-SC, Brazil 89204-250
P: +55-47-3422-5445 F: +55-47-3422-2817
PORTO ALEGRE Av. Cristovão Colombo, 1694-sala 202-Floresta Porto Alegre-RS, Brazil 90560 001
P: +55-51-3222-1324 F: +55-51-3222-2599
RECIFE Av. Conselheiro Aguiar, 2738-6th andar-conj. 604-Boa Viagem Recife-PE, Brazil 51020-020
P: +55-81-3326-3781 F: +55-81-3326-5047

Peru:
NSK PERU S.A.C.
LIMA Av. Caminos del Inca 670, Ofic : # 402, Santiago del Surco, Lima, Perú
P: +51-1-652-3372 F: +51-1-638-0555

Mexico:
NSK RODAMIENTOS MEXICANA, S.A. DE C.V.
MEXICO CITY ☆ Av. Presidente Juarez No.2007 Lote 5, Col. San Jeronimo Tepetlacalco, Tlalnepantla, Estado de Mexico, Mexico, C.P.54090
P: +52-55-3682-2900 F: +52-55-3682-2937
MONTERREY Av. Ricardo Margain 575, IOS Torre C, Suite 516, Parque Corporativo Santa Engracia, San Pedro Garza Garcia, N.L. Mexico, C.P.66267
P: +52-81-8000-7300 F: +52-81-8000-7095

<As of December 2015>
For the latest information, please refer to the NSK website.
www.nsk.com

Motion & Control

No. 26 April 2016

Published by NSK Ltd.

NSK used environmentally friendly printing methods for this publication.

CAT. No. ETJ-0026 2016 C-4 Printed in Japan